UNIVERSITÄT ZU LÜBECK
INSTITUT FÜR MEDIZINTECHNIK

From the Institute of Medical Engineering
of the University of Lübeck

Director: Prof. Dr. rer. nat. Thorsten M. Buzug

Development of a Three-Dimensional Magnetic Particle Spectrometer for Magnetic Particle Imaging

Dissertation
for Fulfillment of
Requirements
for the Doctoral Degree
of the University of Lübeck

from the Department of Computer Sciences and Engineering

Submitted by
Xin Chen
from Yancheng, Jiangsu, China

Lübeck, 2023

First referee: Prof. Dr. rer. nat. Thorsten M. Buzug

Second referee: Prof. Dr. -Ing. Alfred Mertins

Date of oral examination: April 11th, 2024

Approved for printing: Lübeck, April 26th, 2024

ACKNOWLEDGEMENTS

From the bottom of my heart, I would like to express my deepest appreciation to my supervisor, Prof. Dr. Thorsten M. Buzug, for his patience and support. Thanks should also go to my doctoral committee, who generously offered knowledge and expertise. Additionally, my work was within the scope of the project “SAMBA PATI”. It would not have been possible without the financial support from the Federal Ministry of Education and Research of Germany.

I am grateful to Prof. Dr. Matthias Gräser and André Behrends, who guided me since my master’s internship. I would like to extend my sincere thanks to Dr. Anselm von Gladiß, Ankit Malhotra, and Jan Stelzner for all the professional and personal support. Really enjoyed the time I spent with all the lovely colleagues at the Institute of Medical Engineering. Special thanks to laboratory technician Dirk Steinhagen, who helped me realize many of my crazy ideas.

I cannot forget to thank my family for their unconditional support and consideration. I would like to express my gratitude to Yen. Without her companion, it would not be easy for me to undertake this journey. Last but not least, thanks to all my friends for their encouragement.

ABSTRACT

In 2005, Bernhard Gleich and Jürgen Weizenecker introduced a novel medical imaging technology called magnetic particle imaging (MPI). MPI takes advantage of the non-linear characteristic of the superparamagnetic iron oxide nanoparticles (SPIONs) to map their distribution in the field of view. It is a promising image modality of high sensitivity and high resolution without involving any ionizing radiation. In MPI, the magnetic particle spectrometer (MPS) is utilized to analyze the spectra of the SPIONs, which allows the evaluation of their performance and estimation of their characteristics. Another usage of the MPS is to record the hybrid system matrix (SM), which is used in image reconstruction. By emulating the magnetic field generated by an MPI scanner, the MPS can significantly save the recording time and include the realistic characteristics of the SPIONs. Since the generated magnetic field is in a three-dimensional (3D) spatial space, a 3D MPS is indispensable for recording the 3D hybrid SM. Different one-dimensional and two-dimensional MPSs have been introduced before, and a 3D MPS prototype was developed in 2018 to show the initial results. In this work, a newly designed 3D MPS is presented in detail, including the transmit chain, the receive chain, and the control unit. It features additionally a temperature control unit, which can maintain and adjust the temperature of the SPION samples during measurement. Lastly, the measurement results of the SPIONs and the SMs verify the functionality of this 3D MPS.

KURZFASSUNG

Im Jahr 2005, präsentierten Bernhard Gleich und Jürgen Weizenecker erstmals eine neuartige medizinische Bildgebungstechnologie namens Magnet-Partikel-Bildgebung (engl. magnetic particle imaging (MPI)). MPI nutzt die nichtlinearen Eigenschaften von superparamagnetischen Eisenoxid-Nanopartikeln (engl. superparamagnetic iron oxide nanoparticles (SPIONs)), um ihre Verteilung im Betrachtungsfeld abzubilden. Es ist eine vielversprechende Bildgebungsmodalität mit hoher Empfindlichkeit und hoher Auflösung, ohne dass ionisierende Strahlung verwendet wird. Für MPI wird ein Magnet-Partikel-Spektrometer (engl. magnetic particle spectrometer (MPS)) verwendet, um die Spektren der SPIONs zu analysieren, damit ihre Leistung beurteilt und ihre Eigenschaften abgeschätzt werden können. Eine weitere Anwendung des MPS ist die Aufnahme der hybriden Systemmatrix (engl. system matrix (SM)), die für die Bildrekonstruktion verwendet wird. Durch die Emulation des von einem MPI-Scanner erzeugten Magnetfelds, kann ein MPS die Aufnahmezeit erheblich verkürzen und die realistischen Eigenschaften der SPIONs einbeziehen. Da sich das erzeugte Magnetfeld im dreidimensionalen (3D) Raum befindet, ist ein 3D-MPS für die Aufnahme des 3D-Hybrid-SM unverzichtbar. Verschiedene eindimensionale und zweidimensionale MPS wurden zuvor eingeführt. Ein 3D-MPS-Prototyp wurde 2018 entwickelt, um die ersten Ergebnisse zu zeigen. In dieser Arbeit wird ein neu gestaltetes 3D-MPS detailliert vorgestellt, einschließlich der Sendekette, der Empfangskette und der Steuereinheit. Es verfügt auch über eine Temperaturkontrolleinheit, die die Temperatur der SPION-Proben während der Messung halten und anpassen kann. Schließlich belegen die Messergebnisse der SPIONs und der SMs die Funktionalität dieses 3D-MPS.

CONTENTS

LIST OF FIGURES

LIST OF TABLES

LIST OF ABBREVIATIONS

2D two-dimensional.
3D three-dimensional.

AC alternating current.
ADC analog to digital converter.

BNC bayonet Neill–Concelman.
BPF band-pass filter.
BSF band-stop filter.

CAD computer-aided design.

DAC digital to analog converter.
DAQ data acquisition.
DB data bus.
DC direct current.

FFL field-free line.

FFP field-free point.
FoV field of view.

I/O input/output.

LED light emitting diode.
LNA low-noise amplifier.
LVTTL low voltage transistor–transistor logic.

MDR mini delta ribbon.
MNP magnetic nanoparticle.
MOSFET metal-oxide-semiconductor field-effect transistor.
MPI magnetic particle imaging.
MPS magnetic particle spectrometer.
MRI magnetic resonance imaging.
MSPS mega sample per second.

PC personal computer.
PCB printed circuit board.
PCI peripheral component interconnect.
PET positron emission tomography.
PID proportional–integral–derivative.
POM polyoxymethylene.

RMS root means square.

SCPI standard commands for programmable instruments.
SM system matrix.

SMA subminiature version A.

SNR signal-to-noise ratio.

SPECT single photon emission computed tomography.

SPION superparamagnetic iron oxide nanoparticle.

TEC thermoelectric cooler.

USB universal serial bus.

CHAPTER 1

INTRODUCTION

Medical technology has rapidly developed over the last decades. Different imaging modalities are widely used in diagnostic and therapeutic procedures. However, the desire for a better imaging method has always motivated scientists and engineers to develop advanced techniques. A new tracer-based, functional, and tomographic imaging modality – magnetic particle imaging (MPI) – was conceived by Bernhard Gleich in 2001 at the Philips Research Laboratory in Hamburg, Germany [1]. Together with Jürgen Weizenecker, Bernhard Gleich developed the first prototype of an MPI scanner and published a pivotal paper in 2005 to prove the concept and show the potential of MPI [2].

MPI utilizes the magnetic nanoparticle (MNP) tracers, which are free of ionizing radiation. It benefits the safety of patients and medical staff when compared to other medical imaging methods, e.g., positron emission tomography (PET) and single photon emission computed tomography (SPECT). Commonly used MNP in MPI is the superparamagnetic iron oxide nanoparticle (SPION), which is also a contrast agent for magnetic resonance imaging (MRI) [3], e.g., Resovist (Bayer Schering Pharma, Berlin, Germany). However, in MPI, the SPIONs are the only source of imaging signals rather than contrast agents used in MRI, namely the surrounding tissues or organs would not be imaged due to their diamagnetic properties [4]. Compared with protons in MRI, the SPIONs have much higher magnetization and faster relaxation time [5]. Thus, MPI promises an outstanding temporal resolution and a higher signal-to-noise ratio (SNR) [6]. In 2009, the first *in vivo* three-dimensional (3D) real-time images of a beating mouse heart were presented [7], it showed that MPI is capable of imaging with a high temporal resolution of 46 frames per second and a high spatial resolution of up to about 1 mm. Two commercial 3D MPI scanners for preclinical applications were successfully developed by Bruker Biospin MRI (Ettlingen, Germany) in 2014 and Magnetic Insight (California, United States) in 2017, respectively. MPI shows great potential for applications, including but not limited to cardiovascular, neuroimaging, tumor imaging, magnetic hyperthermia, and cellular tracking [4]. However, significant upscaling of the system for human use still undergoes development before being utilized clinically [8, 9]. MPI is based on the non-linear magnetic properties of the SPIONs. When applying an external magnetic field, the magnetic moments of the SPIONs will align. With the increase of the field strength, the resultant magnetization increases steeply and reaches saturation at a particular field strength. If an oscillating magnetic field is applied, the SPIONs exhibit a time-varying magnetization, which can induce a voltage signal in the receive coils. For spatial encoding, a static magnetic field gradient, called selection field, is superimposed to establish a field-free point (FFP) or a field-free line (FFL) depending on the encoding scheme. Only the SPIONs at the FFP or FFL in the field of view (FoV) will respond to the oscillating field, and all the other nanoparticles are saturated. By steering the FFP/FFL through the FoV, an image can be formed [2].

An magnetic particle spectrometer (MPS) is a device used in MPI, which is a zero-dimensional MPI scanner. It measures the MNPs without space encoding, namely the selection field can be excluded. Due to the same principle as the MPI, MPS is primarily developed to analyze the spectra of the MNPs so that their performance in MPI can be assessed [10–12]. MPS also shows the ability to estimate the particle parameters, such as the core diameter [13], as well as the environmental conditions including the temperature [14], bound state [15] and viscosity [16]. Recent research extends the applications of MPS to biological and biomedical assays [17–21]. Another usage of the MPS is to record the so-called hybrid system matrix (SM), which is used for image reconstruction. In order to record an SM, the MPS emulates the magnetic field inside an MPI scanner. Instead of a selection field, a static offset field is generated in the MPS [22]. The MPS can significantly reduce the time for recording the SM and, at the same time, keep the realistic response of the MNPs. Since the generated magnetic field is in 3D spatial space, a multidimensional MPS is indispensable for recording the SM used for multidimensional imaging. Few two-dimensional (2D) MPSs were introduced in [23, 24]. Later, in 2018 a 3D MPS prototype was built, and the initial results were shown in [25]. Based on previous experiences, a new 3D MPS has been developed. A temperature control unit was implemented to maintain and adjust the temperature of the MNPs since the influence of the temperature could not be neglected [14].

In this thesis, the contents are arranged into the following chapters:

Chapter 2 describes the basic knowledge of the MNP and its superparamagnetic characteristics. The fundamental principles of MPI are briefly introduced to show how it utilizes the SPIONs. Furthermore, the unique features of the MPS are introduced. The system diagram and the assembled view of the developed 3D MPS are included in this chapter.

Chapter 3 introduces the transmit chain, which generates the drive fields and the offset fields to excite the MNPs. The main hardware is the 3D transmit coil setup. In order to optimize the coil setup, different coil geometries are studied and simulated, and various coil setups are compared with each other for powerloss and field homogeneity. According to the optimized sizes, coil molds are designed to fabricate the coils. For generating the drive fields, a power amplifier is built, which amplifies the excitation signals sent from the personal computer (PC). The construction of the impedance matching network is described in detail, which matches the impedance of the transmit coils to a specific impedance so that sufficient power can be delivered to generate the magnetic field with the required amplitude. To purify the excitation signals, a band-pass filter (BPF) is designed and simulated. The construction of the BPF utilizes self-built tunable inductors. For generating the offset fields, the direct current (DC) sources are used, and the H-bridges are employed to change the directions of the DC.

Chapter 4 contains the descriptions of the receive chain, which receives the response of the excited MNPs. The design and construction of the receive coils are described in detail, as well as the coil formers. To attenuate the directly coupled excitation signals that are usually several orders of magnitude higher than the received particle signals, the band-stop filter (BSF) is designed and simulated. Differential BSFs are built to match the inputs of the low-noise amplifier (LNA), which can amplify the received signals for post-processing in the PC.

Chapter 5 describes the control unit. Various data acquisition (DAQ) cards are introduced according to their functionalities. A diagram shows the connection between the DAQ cards and other hardware in the MPS. To monitor the currents flowing in the transmit coils, the feedback components utilizing the Rogowski coils are designed and built. Since the MNPs are subject to changes in temperature, a temperature control unit featuring a water-circulating system is implemented to maintain and adjust the temperature of the nanoparticle samples during measurement. One opto-isolator circuity is used to safely control the H-bridges and isolate them from the DAQ cards. Another opto-isolator circuity is designed to prevent earth loops that could cause errors while controlling the DC sources.

Chapter 6 shows the measurement results. Calibration coils are used to calibrate the MPS system before quantitative measuring. Different nanoparticle samples are measured and compared. Various temperature measurements show the impact of the temperature on the MNPs and thus the necessity of temperature control. The SM measurements verify the functionality of this 3D MPS to record hybrid SMs.

Chapter 7 summarise this thesis with discussions and future improvements.

CHAPTER 2

FUNDAMENTAL PRINCIPLES

2.1 Magnetic Nanoparticle

2.1.1 Superparamagnetic Nanoparticle

MNPs are particles of size in the nanometer range, whose magnetic property is due to their iron oxide core material. An ideal MNP is illustrated in Fig. 2.1. The magnetic core is surrounded by a non-magnetic coating, which ensures the stability of the particle solution against aggregation and agglomeration. The diameter of the core is d_c, while the diameter of the whole particle, termed the hydrodynamic diameter, is d_h.

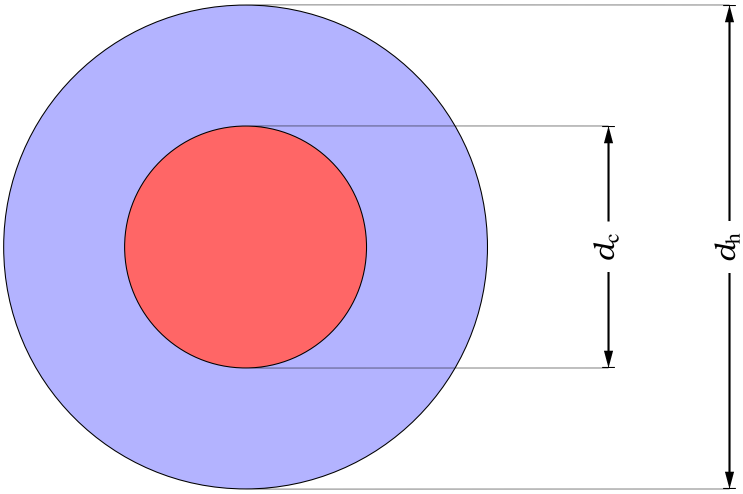

Figure 2.1: Illustration of an MNP. The magnetic core of diameter d_c is marked in red color, and the non-magnetic coating is marked in blue color. The total size of the particle is described by the hydrodynamic diameter d_h.

When the MNPs are sufficiently small, they compose a single magnetic domain and gain superparamagnetic characteristics. It means that the magnetic moments of the MNPs can randomly flip directions due to the thermal motion. Therefore, in an ensemble of MNPs, the net magnetic moment becomes zero. When an external magnetic field is applied, the MNPs are magnetized, and their magnetic moments are aligned with the direction of the field. The MNPs behave like paramagnets but with a much higher magnetic susceptibility of the ferromagnetic or ferrimagnetic material. Thus, such magnetism is named superparamagnetism. The iron oxide MNP is named superparamagnetic iron oxide nanoparticles (SPION).

In MPI, the most commonly used core materials are iron oxide maghemite (γ-Fe_2O_3) and magnetite (Fe_3O_4), the core size is about 5–30 nm diameter and the hydrodynamic diameter of the MNP is about 40–100 nm (see Table 1 in [6]). Resovist is one of the candidates for an MPI tracer since it is a clinically approved contrast agent for MRI. It can, therefore, be safely used inside the human body. Due to the good performance in MPI, Resovist has been widely used as a “gold standard” tracer. However, it is not optimized for MPI application [26] and has been discontinued by the manufacturer since 2009. A tailored MNP tracer for MPI could significantly improve the performance [27].

2.1.2 Static Magnetization

The static behavior of the SPIONs can be approximately described by the Langevin function [28]. In the presence of an external magnetic field H, the net magnetization of an ensemble of SPIONs is described as

$$M = mc\left(coth(\xi) - \frac{1}{\xi}\right), \tag{2.1}$$

where

$$\xi = \frac{m\mu_0 H}{k_B T} \tag{2.2}$$

is the ratio of the magnetic energy and the thermal energy. c denotes the particle concentration, k_B is the Boltzmann constant, T is the temperature, and μ_0 is the permeability of the vacuum. Eq. 2.1 shows the linear relation between the magnetization and the concentration of the particles. A typical magnetization curve of the SPIONs is shown in Fig. 2.2(a). For mono-disperse spherical particles, the magnetic moment m is given as

$$m = V_c M_S = \frac{1}{6}\pi {d_c}^3 M_S, \tag{2.3}$$

where V_c is the core volume of the particle, d_c is the particle core diameter (see Fig. 2.1), M_S is the saturation magnetization of the core material (about 480–520 kA/m for magnetite (Fe_3O_4), 290–390 kA/m for maghemite (γ-Fe_2O_3) [29]). In reality, the core diameter of the SPION is not mono-dispersed but rather a size distribution, which could impact the imaging performance [30, 31]. In principle, a larger particle core leads to a higher magnetic moment and a steeper magnetization curve, which can improve the image sensitivity and the spatial resolution [6]. However, if the core size exceeds a critical size, the SPION may lose its superparamagnetic characteristics. Moreover, as noticed from Eq. 2.1, the temperature change influences the behavior of the SPIONs, e.g., an increasing temperature leads to a reduced slope of the magnetization curve [32]. The static property of the MNPs is critical for spatial encoding and generation of MPI images [4].

2.1.3 Dynamic Property

The particle magnetization discussed before is a static property, i.e., the SPIONs are instantly aligned with the external field. In the presence of a time-varying external field, the dynamic property must be considered. There are two main mechanisms for describing the change of particle magnetization. One is called Néel relaxation, which describes the internal rotation of the particle magnetization. The other is called Brownian relaxation, which describes the mechanical rotation of the particle.

Due to the magnetic anisotropy, the magnetic moment usually has two stable orientations antiparallel to each other. The time constant in associating with the probability for the magnetization to flip between the two orientations is called the Néel relaxation time, which is given as

$$\tau_{\mathrm{N}} = \tau_0 \, exp\left(\frac{KV_{\mathrm{c}}}{k_{\mathrm{B}}T}\right) , \tag{2.4}$$

where K is the magnetic anisotropy constant, and V_{c} is the particle core volume [33]. τ_0 is a characteristic of the material, typically in the range $0.1\text{–}1\,\mathrm{ns}$. The Brownian relaxation time constant is given as

$$\tau_{\mathrm{B}} = \frac{3\eta V_{\mathrm{h}}}{k_{\mathrm{B}}T} , \tag{2.5}$$

where η is the viscosity of the particle medium, V_{h} is the hydrodynamic volume of the particle (see Fig. 2.1) [34]. In an MNP suspension, both the

Brownian and Néel relaxation mechanisms may play a role. Which one dominates depends on the size of the MNP, and the external magnetic field strength and frequency [35, 36]. The effective relaxation time is written as

$$\tau_{\mathrm{eff}} = \frac{\tau_{\mathrm{N}}\tau_{\mathrm{B}}}{\tau_{\mathrm{N}} + \tau_{\mathrm{B}}}\,. \tag{2.6}$$

The particle relaxation time is a critical parameter for spatial resolution [6]. Notice that in Eq. 2.4 and Eq. 2.5, the temperature influences both relaxation times. A higher temperature leads to a reduced relaxation time, i.e., it is easier to align the MNPs with the external magnetic field. The dynamic property of the MNPs is the basis for MPI signal generation and acquisition [4].

2.2 Magnetic Particle Imaging

2.2.1 Signal Generation

MPI is a trace-based imaging modality, and it takes advantage of the non-linear magnetization behavior of the SPIONs. The typical magnetization curve of the SPIONs is shown in Fig. 2.2(a). At lower magnetic field strength, the magnetization of the SPIONs increases almost linearly with the applied field. However, the magnetization quickly reaches a saturation level at higher field strength. If an oscillating magnetic field, termed excitation field, of frequency f_0 is applied (see Fig. 2.2(d)), the SPIONs will be excited and exhibit a time-varying magnetization (see Fig. 2.2(b)). When the excitation field has a sufficiently high amplitude, due to the non-linear behavior of the SPIONs, the exhibited magnetization reaches saturation. The time-varying magnetization induces then a voltage signal (see Fig. 2.2(c)) in the receive coils, which in the frequency domain contains not only the fundamental frequency f_0 but also its harmonics (see Fig. 2.2(e)). However, the excitation field will also induce a signal in the receive coil, which in amplitude is several orders higher than the particle signals [37]. Therefore, higher harmonics are the key feature distinguishing the particle signal from those induced by the excitation field.

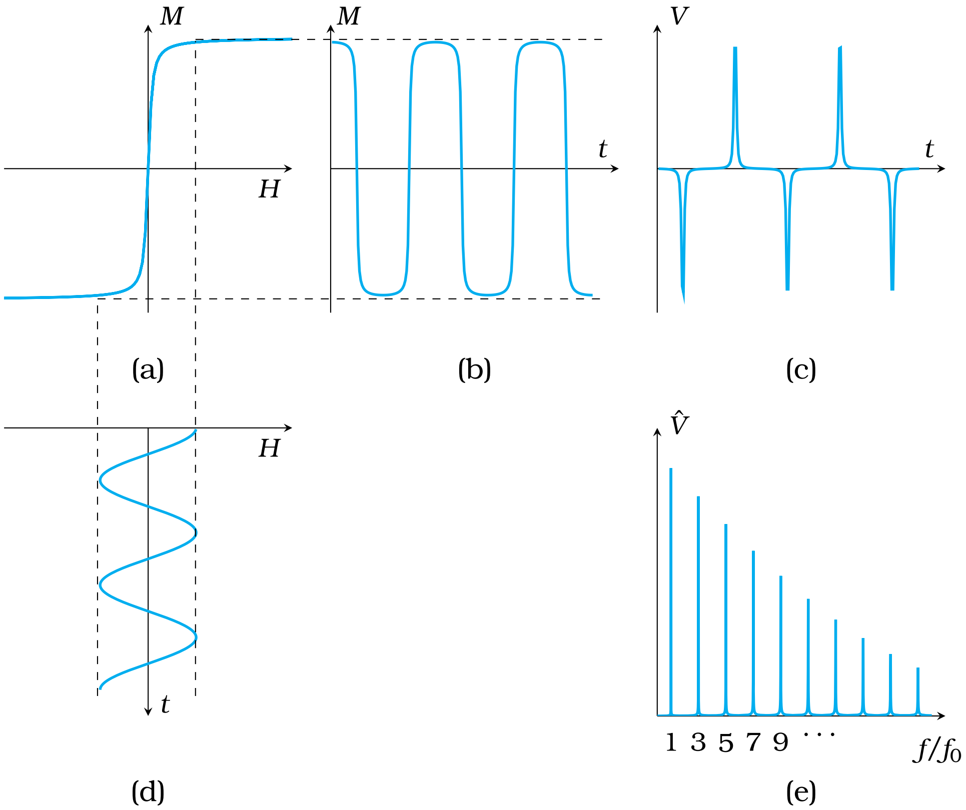

Figure 2.2: Response of SPIONs to an oscillating excitation field. An oscillating excitation field of frequency f_0 (d) is applied to the SPIONs. Due to the non-linear magnetization behavior of the SPIONs (a), the exhibited time-varying magnetization (b) reaches a saturation level. Thus, the induced voltage signal (c) contains the fundamental frequency f_0 as well as the higher harmonics (e).

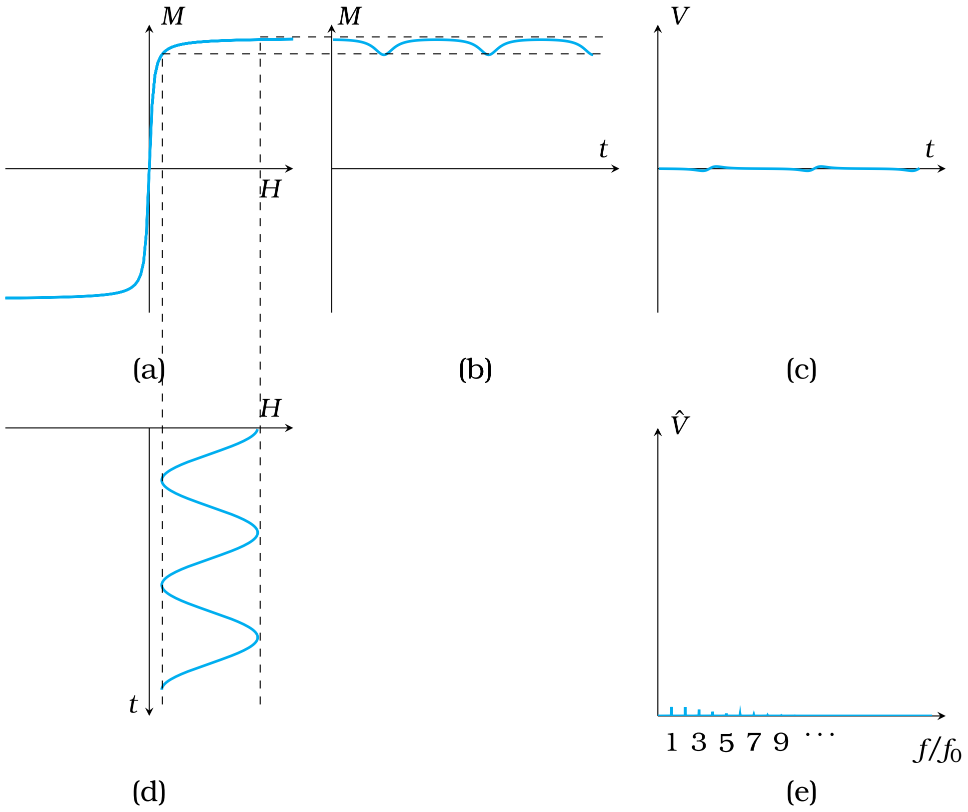

Figure 2.3: Response of SPIONs to an oscillating excitation field superimposed with a static field. An oscillating excitation field of frequency f_0 superimposed with a static field (d) is applied to the SPIONs. Due to the non-linear magnetization behavior of the SPIONs (a), the exhibited time-varying magnetization (b) is in saturation. It induces almost no signals in the time domain (c) or the frequency domain (e).

2.2.2 Spatial Encoding

Upon the application of the excitation field, the SPIONs are excited, and their response can be detected. However, it is impossible to localize the SPIONs and determine their spatial distribution. A spatial encoding method is introduced to solve this problem. As seen in Fig. 2.3(d), a static magnetic field is superimposed with the oscillating excitation field. The exhibited magnetization of the SPIONs saturates (see Fig. 2.3(b)) and induces almost no signals in the time domain (see Fig. 2.3(c)) or frequency domain (see Fig. 2.3(e)). Thus, in MPI a static magnetic field gradient, termed the selection field, is applied in the FoV. The selection field creates a point with zero field strength, termed the field-free point (FFP), while the magnitude of the field increases linearly in all directions away from the FFP [2]. Therefore, when superimposing the selection field with the excitation field, only the SPIONs at or in the close vicinity of the FFP can induce a strong signal (see Fig. 2.2). SPIONs away from the FFP are saturated and contribute nearly nothing to the signal (see Fig. 2.3). This relation between the induced signals and the FFP positions ensures the so-called spatial encoding. An alternative encoding method using the FFL promises an increase in the system sensitivity [38–40]. However, it is beyond the scope of this thesis.

To form an image, the FFP is moved over the entire FoV. The excitation field is applied at each position, and the received signal is recorded. The movement of the FFP can be performed by mechanically moving the object or the coil assembly inside the scanner. However, mechanical movement leads to slow image acquisition. The SNR is also limited due to the low excitation field amplitude, while a high field would shift the FFP [2]. An advanced method of moving the FFP uses the homogeneous magnetic field, termed the drive field. By superimposing the drive field, the selection field at any given point in the FoV can be canceled, namely the FFP can be moved to any point. The effective local field at position $\mathbf{r}$ is expressed as

$$\mathbf{H}(\mathbf{r}, t) = \mathbf{H}_{\mathrm{S}}(\mathbf{r}) + \mathbf{H}_{\mathrm{D}}(t)\,, \tag{2.7}$$

where $\mathbf{H}_{\mathrm{S}}$ denotes the selection field, and $\mathbf{H}_{\mathrm{D}}$ denotes the drive field. The use of the drive field significantly shortens the acquisition time. The amplitude of the drive field must be large enough to cancel the selection field at the border of the FoV [2]. In a multidimensional scanner, with a certain drive field waveform, the FFP can be moved continuously along a trajectory to cover the FoV. Different trajectories, such as Cartesian, radial, and spiral trajectories, have been analyzed [41]. However, the most commonly used one is the Lissajous trajectory (see Fig. 2.4) [42, 43]. A typical drive field has an amplitude of about $10\text{–}20\,\mathrm{mT}/\mu_0$, and a frequency of $25\,\mathrm{kHz}$. To perform a 2D Lissajous trajectory, [42, 43] suggested drive field frequencies of

- $2.5\,\mathrm{MHz}/99 = 25.25\,\mathrm{kHz}$,
- $2.5\,\mathrm{MHz}/98 = 25.51\,\mathrm{kHz}$,

which led to a repetition time of $3.88\,\mathrm{ms}$. For 3D Lissajous trajectory, [7] used the drive field frequencies of

- $2.5\,\mathrm{MHz}/102 = 24.51\,\mathrm{kHz}$,
- $2.5\,\mathrm{MHz}/96 = 26.04\,\mathrm{kHz}$,
- $2.5\,\mathrm{MHz}/99 = 25.25\,\mathrm{kHz}$,

which had a repetition time of $21.54\,\mathrm{ms}$. The same frequencies are also used in the preclinical MPI scanner from Bruker Biospin MRI (Ettlingen, Germany).

2.2.3 Reconstruction

The excited SPIONs exhibit a time-varying magnetization, which can induce a voltage signal in the receive coil. It is given as [44]

$$u(t) = -\mu_0 \frac{\partial}{\partial t} \int_\Omega \mathbf{M}(\mathbf{r}, t)\mathbf{p}_{\mathrm{rec}}(\mathbf{r})\, \mathrm{d}^3 r\,, \tag{2.8}$$

where Ω is the volume of the FoV. According to the law of reciprocity, the receive coil sensitivity $\mathbf{p}_{\mathrm{rec}}$ equals the magnetic field $\mathbf{H}_{\mathrm{rec}}$ generated by the coil per unit current I_0, which is

$$\mathbf{p}_{\mathrm{rec}}(\mathbf{r}) = \frac{\mathbf{H}_{\mathrm{rec}}(\mathbf{r})}{I_0}\,. \tag{2.9}$$

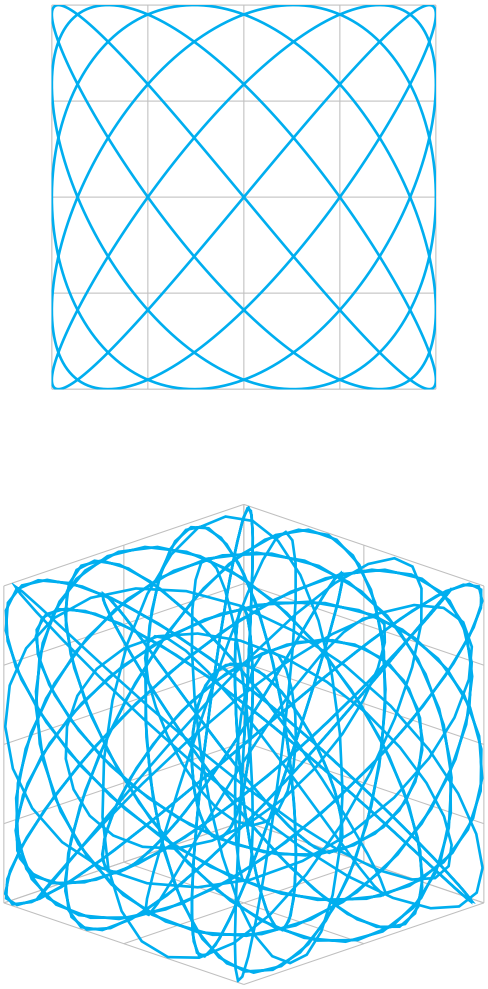

Figure 2.4: Illustration of the Lissajous trajectory. On the top is a 2D Lissajous trajectory, and on the bottom is a 3D one. The grey lines indicate the FoV grid. The drive field moves the FFP through the path indicated by the colored line, which is called the Lissajous trajectory.

Referring to Eq. (2.1), the particle magnetization $\mathbf{M}(\mathbf{r}, t)$ determined by the local field $\mathbf{H}(\mathbf{r}, t)$ can be rewritten as

$$\mathbf{M}(\mathbf{r}, t) = \overline{\mathbf{m}}(\mathbf{r}, t)c(\mathbf{r}) , \tag{2.10}$$

where $\overline{\mathbf{m}}(\mathbf{r}, t)$ is the mean magnetic moment of the particles, and $c(\mathbf{r})$ is the particle concentration. For numerical processing, Eq. (2.8) needs to be discretized [41]. If the time t is sampled at position t_k , $k = 0, \cdots, K - 1$, and the FoV is discretized at position $\mathbf{r}_n$, $n = 0, \cdots, N - 1$, with voxel size ΔV, by substituting Eq. (2.10) into Eq. (2.8) one gets

$$\begin{aligned} u(t_k) &\approx \sum_{n=0}^{N-1} -\mu_0 \Delta V \frac{\partial}{\partial t} \overline{\mathbf{m}}(\mathbf{r}_n, t_k)\mathbf{p}_{\text{rec}}(\mathbf{r}_n)c(\mathbf{r}_n) \\ &= \sum_{n=0}^{N-1} G(t_k, \mathbf{r}_n)c(\mathbf{r}_n) , \end{aligned} \tag{2.11}$$

where

$$G(t_k, \mathbf{r}_n) = -\mu_0 \Delta V \frac{\partial}{\partial t} \overline{\mathbf{m}}(\mathbf{r}_n, t_k)\mathbf{p}_{\text{rec}}(\mathbf{r}_n) . \tag{2.12}$$

The Eq. (2.11) can be written in the matrix vector form as

$$\mathbf{u} = \mathbf{G}\mathbf{c} , \tag{2.13}$$

where $\mathbf{u}$ is the vector of measured voltage, $\mathbf{c}$ is the vector of particle concentration, and $\mathbf{G}$ is the so-called system matrix (SM). In the frequency domain, Eq. (2.13) can be written as

$$\hat{\mathbf{u}} = \hat{\mathbf{G}}\mathbf{c} . \tag{2.14}$$

To reconstruct the spatial distribution $\mathbf{c}$ of the SPIONs, Eq. (2.14) needs to be inverted. Commonly, the matrix inversion problem is solved by the regularized least squares

$$\left\|\hat{\mathbf{G}}\mathbf{c} - \hat{\mathbf{u}}\right\|_2^2 + \lambda \left\|\mathbf{c}\right\|_2^2 \xrightarrow{c} \min , \tag{2.15}$$

where λ is the regularization parameter. Besides this SM-based reconstruction, there is a time-domain approach known as x-space reconstruction [45, 46]. However, the latter is not included in the scope of this thesis.

2.2.4 System Matrix

The SM is used in image reconstruction, which maps the relationship between the measured signals and the particle concentration. It contains information about the particle characteristics, instrument geometry, and the applied field properties [47]. Various methods have been proposed to acquire the SM. The first published MPI images were reconstructed using a measurement-based SM [2, 7, 43]. A robot moves a delta sample with known concentration and known volume through the FoV in the imaging scanner, and the measurement is performed at every discrete position. The measured SM inherently contains the characteristics of the scanner and the tracer. However, this means every change in the scanner or use of a new tracer requires a new SM. The main drawback is the long acquisition time. According to the calculation in [44], an SM of $64{\times}64{\times}64$ needs approximately three days to acquire. Additionally, since the delta sample size is usually chosen to be as small as possible, the SNR of the measurement is low. However, due to the good quality of the reconstructed imaging, it is still considered to be a gold standard.

An alternative way to determine the SM is known as the model-based approach [48, 49]. Instead of measuring, the SM is calculated by modeling the magnetic field and the sensitivity profile of the receive coils, the magnetization response of the SPIONs, and the transfer function of the receive chain of the imaging scanner. Images reconstructed by the model-based SM showed comparable results with those reconstructed by a measurement-based SM [48]. However, a more realistic particle model is needed to improve the imaging quality. An approximate calculation time for a model-based SM of size $64 \times 64 \times 64$ on a standard PC is about $30\,\mathrm{min}$ [44].

Another promising method to determine the SM is the hybrid approach [22]. It extends the model-based approach by measuring the characteristics of the SPIONs with an MPS. The magnetic field inside a scanner is emulated in the MPS. Hence, the SPIONs are measured without robot movement. Under the same condition, the acquisition time for an SM of size $64{\times}64{\times}64$ is about $94\,\mathrm{min}$ [44]. Furthermore, since the size of the delta sample can be chosen independently of the voxel size and a more dedicated receive coil is used, the SNR is much higher than that in the measurement-based approach. Compared with the model-based approach, the hybrid approach includes the realistic characteristics of the SPIONs, which are difficult to model [50]. However, a multidimensional MPS with offset fields is on-demand for fully emulating the imaging scanner.

2.3 Magnetic Particle Spectrometer

2.3.1 Magnetic Field

MPS can be used as a tool to examine the characteristics of the SPIONs for their performance in MPI [10, 11]. Compared to an MPI scanner, MPS does not include the selection field. Hence, the MNPs are measured inside the MPS without spatial encoding. The sample chamber is normally very small in size since it only needs to fit a sample vial. Due to the small sample chamber, the MPS easily provides a high SNR.

For MPS to be able to record the SM, a static offset field produced by the DC source is used instead of the selection field. Similar to Eq. (2.7), the magnetic field inside a MPS can be expressed as

$$\mathbf{H}(t) = \mathbf{H}_{\mathrm{O}}(t) + \mathbf{H}_{\mathrm{D}}(t)\,, \tag{2.16}$$

where $\mathbf{H}_{\mathrm{O}}$ denotes the static offset field, and $\mathbf{H}_{\mathrm{D}}$ denotes the drive field. Therefore, the magnetic field at arbitrary spatial positions in the FoV of a scanner can be emulated.

In this work, the developed 3D MPS can apply drive fields up to $20\,\mathrm{mT}/\mu_0$. To fulfill a Lissajous trajectory excitation (see Section 2.2.2), the field frequencies in three orthogonal directions are $24.51\,\mathrm{kHz}$, $26.04\,\mathrm{kHz}$, and $25.25\,\mathrm{kHz}$, respectively. The offset fields can reach $[-20, 20]\,\mathrm{mT}$ in all three dimensions.

2.3.2 Temperature Control

As mentioned in Section 2.1.2 and 2.1.3, the temperature will influence the behavior of the MNPs. If neglecting the particle dynamics, the increasing temperature causes a reduced slope of the magnetization curve and, therefore, a decrease of the higher harmonics [14, 32, 51]. If considering the particle dynamics, the increasing temperature leads to a shorter relaxation time and then an increase of the higher harmonics [52, 53]. Since the impact of the temperature is not negligible, during the measurement of the nanoparticle sample, the temperature of the MNPs should be controlled. In this work, the temperature of the sample chamber can be adjusted from 10 °C to 60 °C.

2.3.3 System Diagram

The system diagram of the MPS described in this thesis is shown in Fig. 2.5. Note that the signal chain of only one channel is fully shown in the diagram. The system is divided into three parts according to their functionalities:

Transmit Chain The transmit chain includes the components to generate the oscillating drive fields and the static offset fields. The excitation signals sent from the PC are amplified by the power amplifier and then purified by the BPF. The impedance matching network matches the impedance of the transmit coils to a specific impedance according to the power amplifier. The DC source applies direct current on the transmit coils to generate the offset fields. The H-bridge is used to switch the polarities of the DC.

Receive Chain The receive chain consists of the components for receiving the response of the MNPs. The receive coils detect the change of the particle magnetization as voltage signals. The BSF damps the received signals at the fundamental frequency and lets pass the harmonics. The LNA amplifies the received signals to match the input range of the data acquisition (DAQ) cards.

Control Unit The control unit includes the PC with DAQ cards for sending, receiving, and processing the signals. The feedback is to monitor the current flowing through the transmit coils. The temperature control unit maintains and adjusts the temperature of the nanoparticle samples. The opto-isolator circuitries are used to safely and precisely control the H-bridge and the DC source. Power supplies power different components in the MPS system.

Notice that in the system diagram, the transmit coils and the receive coils are duplicated to form a generation unit and a cancellation unit. This is according to a cancellation method proposed in [54, 55]. The BSF is commonly used to attenuate the directly coupled excitation signals. However, it also attenuates the particle signals at the fundamental frequency. The cancellation method damps the induced excitation signal by applying an inversed signal. To do so, the transmit coils and the receive coils are built identically twice. The receive coils are connected in series but with inverse polarity. During measurement, the particle samples are placed only in the generation unit. However, in practice, it is impossible to build identical coils. Therefore, in this work, the filter method and the cancellation method are combined, as suggested in [54, 55], to achieve a better attenuation of the excitation signals and largely preserve the particle signals at the fundamental frequency. Views of the assembled 3D MPS system are shown in Fig. 2.6. Different parts are designed and built separately and then mounted in a 19-inch rack. Due to the modular design approach, the system can be easily maintained, and it is possible to be customized and upgraded in the future.

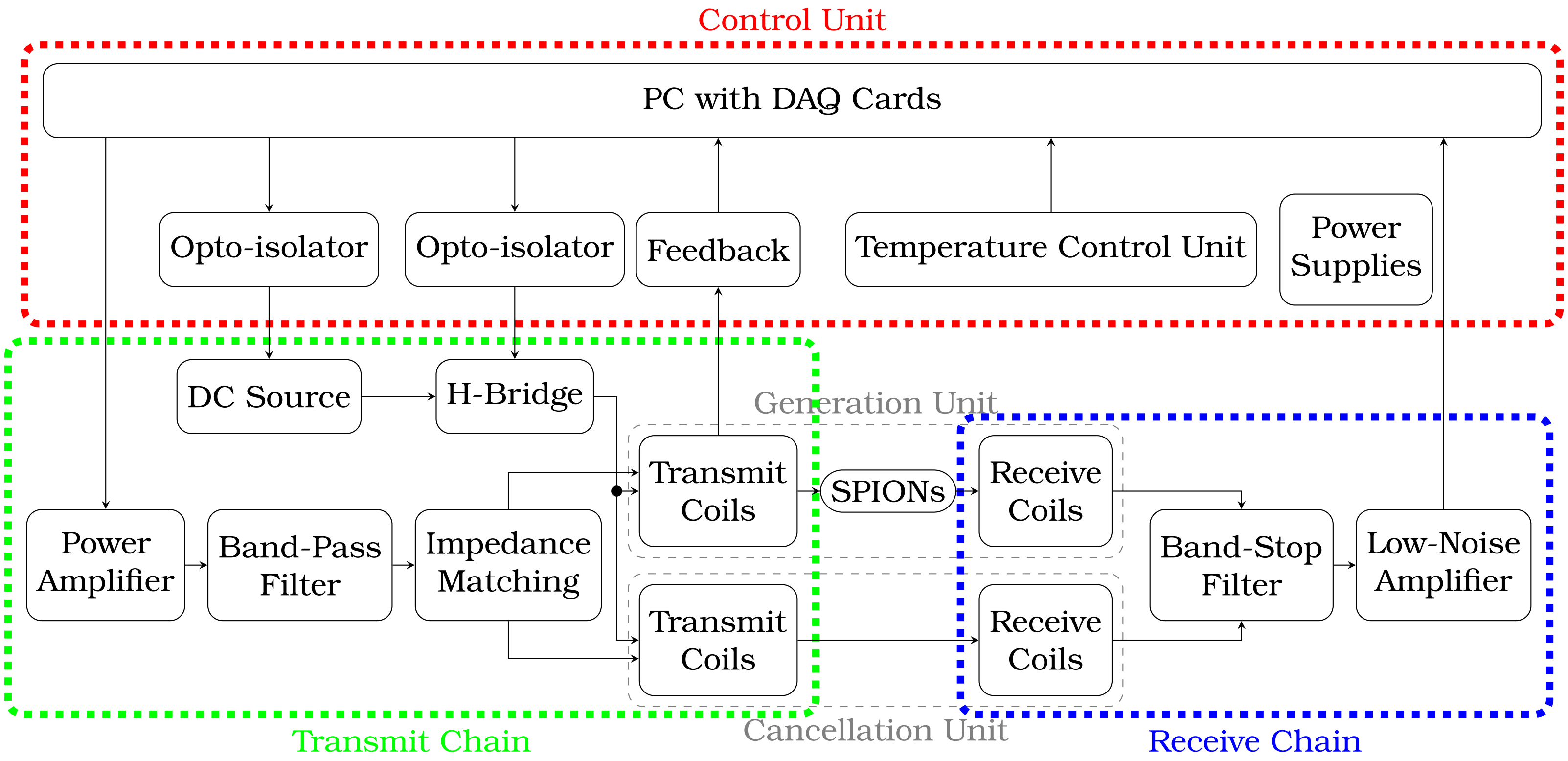

Figure 2.5: System diagram of the 3D MPS. It consists of three parts which are the transmit chain, the receive chain, and the control unit. The transmit coils and the receive coils form a generation unit and a cancellation unit. The nanoparticle samples are placed only in the generation unit for measuring. Note that the signal chain of only one channel is fully shown in the diagram.

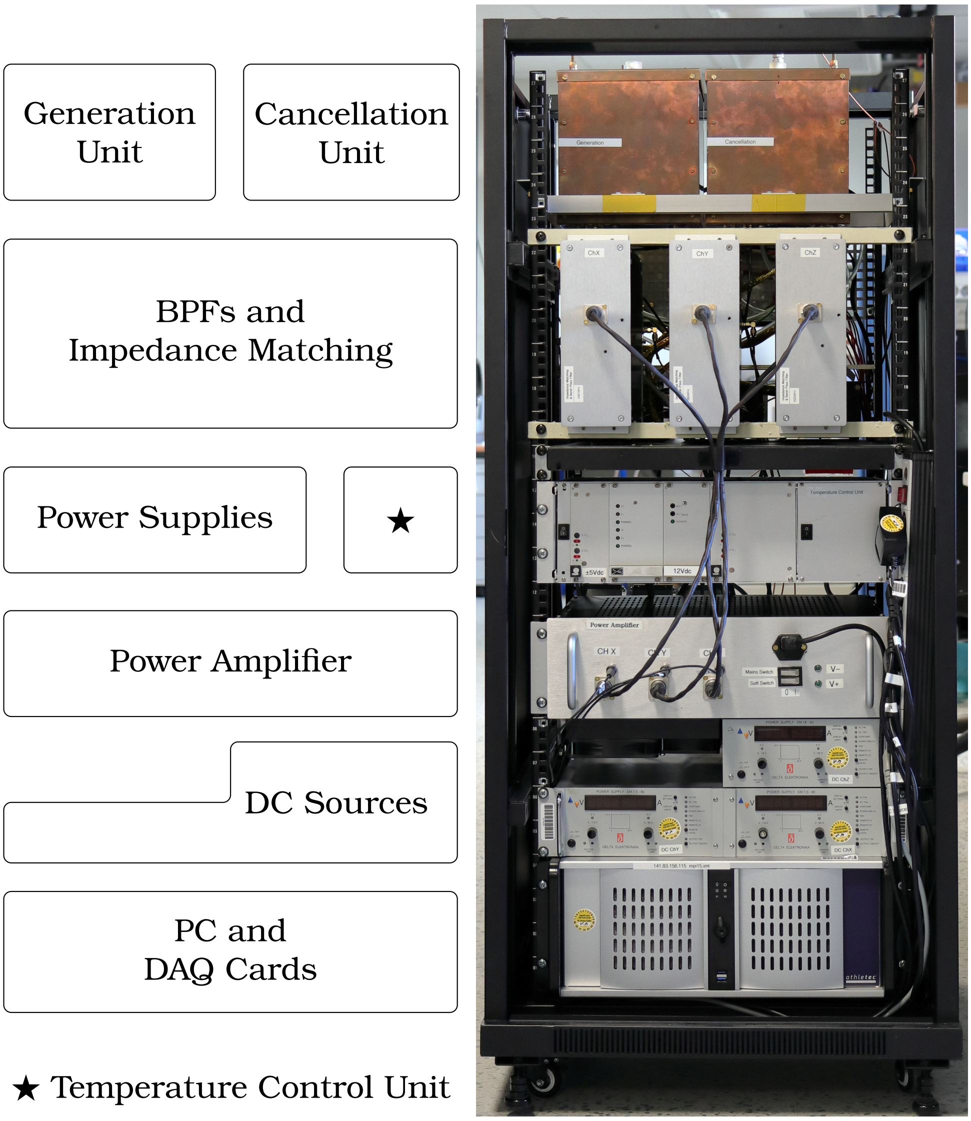

(a) Front view

Figure 2.6: Views of the 3D MPS system. (a) is the front view, (b) is the back view. Different components are indicated by the blocks. The entire system is mounted in a 19-inch rack. Due to the modular design approach, the system can be easily maintained, and it is possible to be customized and upgraded in the future.

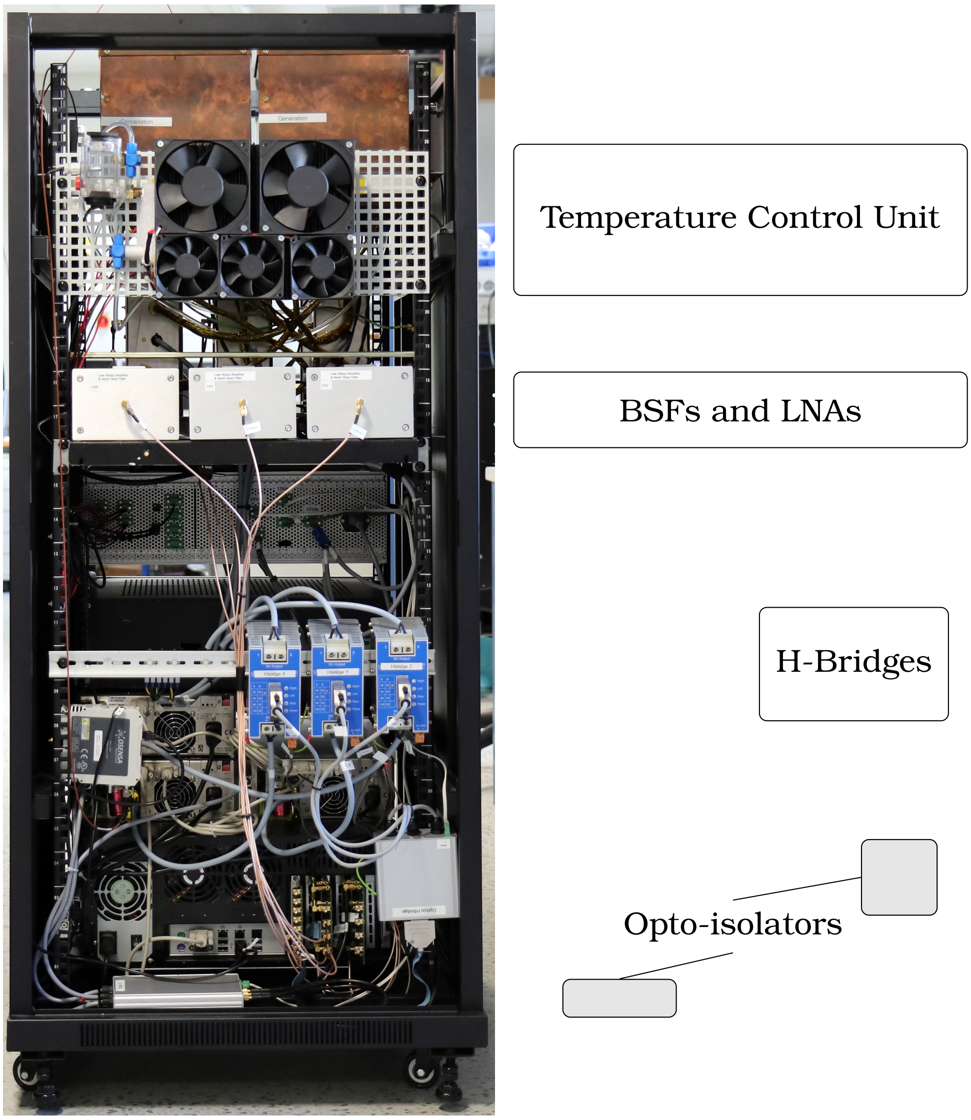

(b) (cont.) Back view

Figure 2.6 (cont.): Views of the 3D MPS system (continued). (a) is the front view, (b) is the back view. Different components are indicated by the blocks. The whole system is mounted in a 19-inch rack. Due to the modular design approach, the system can be easily maintained, and it is possible to be customized and upgraded in the future.

CHAPTER 3

TRANSMIT CHAIN

3.1 Transmit Coils

3.1.1 Design Considerations

The Transmit coil is the core hardware of the MPS. The sample chamber is small in MPS since it only needs to fit a sample vial. In this study, standard micro-centrifuge tubes with conical bottoms and a volume of $0.6\,\mathrm{mL}$ are used to contain the nanoparticle samples. The tube has a maximum outer diameter of about $7.7\,\mathrm{cm}$ and a length of $3\,\mathrm{cm}$. When filling with less than $50\,\mu\mathrm{L}$ nanoparticle sample, which is usually the case, the tip part of the tube is limited in a $5\,\mathrm{mm}^3$ region. The homogeneity of the drive field generated by the transmit coils is considered only in this area.

Whereas the powerloss of the coil plays a more critical role. The greater the powerloss, the harder it is to cool the coil and the larger the power amplifier required to supply it. Reducing the powerloss of the coil can provide significant benefits. Hence, the aim is to minimize the powerloss until an active air-cooling system can stabilize the temperature of the coils [56]. The powerloss of the coil is generally expressed as

$$P = I^2 R\,, \tag{3.1}$$

where I is the current flowing in the coil, and R denotes its resistance. As noticed from Eq. (3.1), in order to reduce the powerloss, it is more effective to reduce the current applied to the coil than to reduce the resistance of the coil. Hence, a coil with less powerloss tends to be bigger in size. However, a coil of bigger size brings more complexities to the fabrication and the supplementary hardware. Thus, a trade-off should be made in the design. Additionally, in this study, a multidimensional coil setup needs to be designed. The size of the coils in different channels will influence each other. Therefore, it is important to optimize the coil setup as a whole.

3.1.2 Coil Geometry

A 3D transmit coil setup in an MPS is illustrated in Fig. 3.1. In the x-axis direction, a single solenoid coil (named T_x-coil in the following) is used, in which the sample vial is placed in the center for measuring. In perpendicular y- and z-axis directions, two Helmholtz-like pairs of coils (named T_y- and T_z-coils in the following, respectively) are used to ensure the accessibility of the central bore.

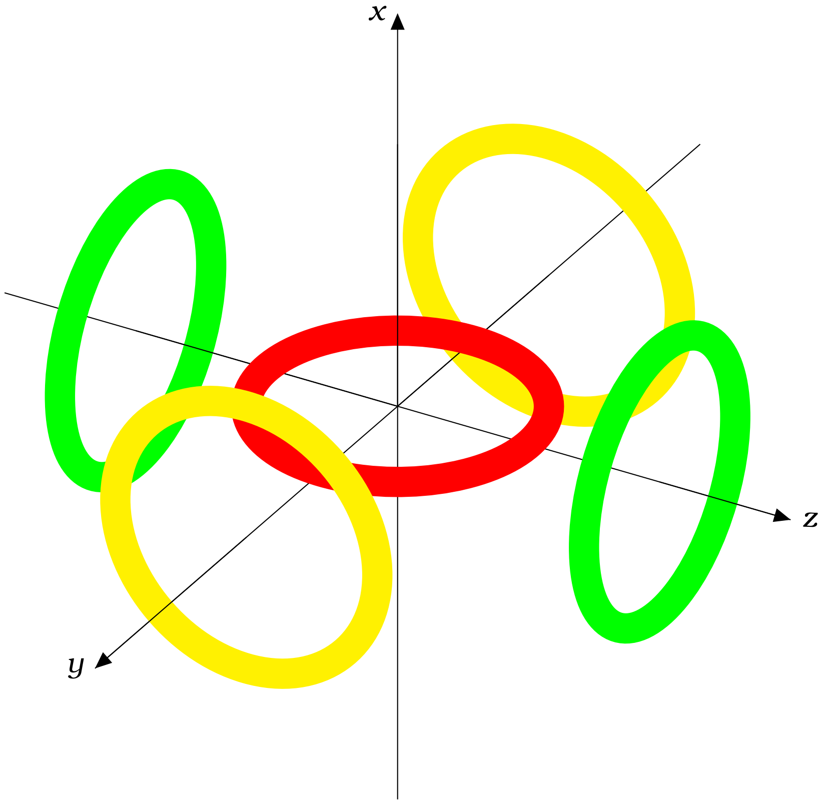

Figure 3.1: Illustration of a 3D transmit coil setup. The perpendicular x-, y-, and z-axis represent the directions of the magnetic fields generated by the transmit coils. In the x-axis direction, a single solenoid coil (T_x-coil) is used. In y- and z-axis directions, two Helmholtz-like pairs of coils (T_y- and T_z-coils) are used. Note that the circular shape is only for illustration.

In the previous study, published in [25], different coil setups were compared with their powerlosses, including circular, rectangular, curved circular, curved rectangular, and quasi-rectangular types. The simulation was performed using an internally developed software ScannerConf (Institute of Medical Engineering, University of Lübeck, Germany). As shown in Fig. 3.2, from (a) to (f), the crossed flat rectangular setup has the lowest powerloss. The distance between the coils in each coil pair can be further reduced to

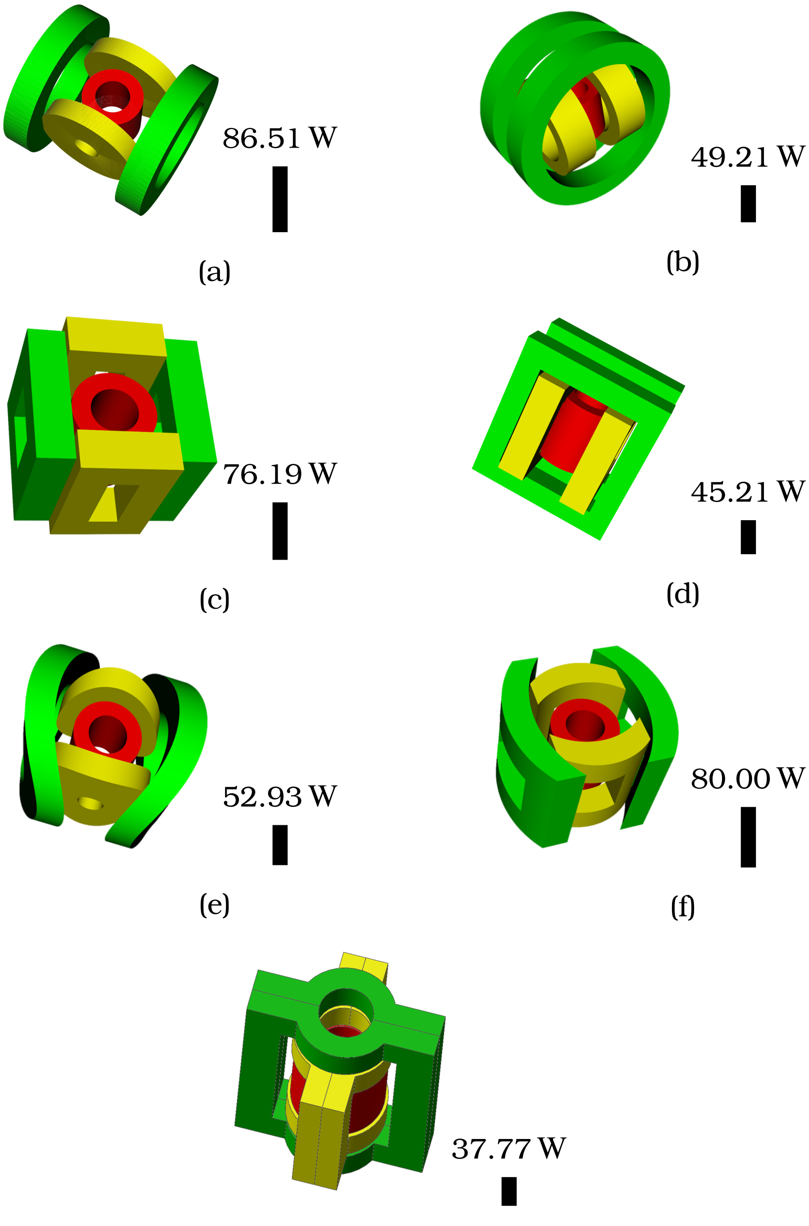

(a) (b) (c) (d) (e) (f) (g)

Figure 3.2: Powerloss comparison of different coil setups: (a) flat circular; (b) crossed flat circular; (c) flat rectangular; (d) crossed flat rectangular; (e) curved circular; (f) curved rectangular; (g) quasi-rectangular. The magnetic field generated by the transmit coils is $20\,\mathrm{mT}/\mu_0$ in the center. From (a) to (f), the powerloss results are simulated. In (g), the powerloss result is approximately calculated according to (d). [25]

achieve a lower powerloss. As the central bore of the coil setup should be accessible for placing the sample vials, the quasi-rectangular coil setup was proposed (see Fig. 3.2(g)). Due to the limitation of the software, it was not possible to simulate an irregular shape of a coil. The powerloss of the quasi-rectangular coils setup was approximately calculated according to the crossed flat rectangular coil setup (see Fig. 3.2(d)). Moreover, the size modification was done by manually changing the parameters in the simulation software. Although many efforts had been put into optimization, the powerloss result of each coil setup could not be proved to be the lowest. Hence, the results shown in Fig. 3.2 are only for relative comparison. Due to the abovementioned limitation, a numerical approach was implemented to improve the optimization process.

As illustrated in Fig. 3.3, the Biot-Savart law states the magnetic field produced by an electric current:

$$\mathrm{d}\mathbf{B} = \frac{\mu_0}{4\pi} \cdot \frac{I\mathrm{d}\boldsymbol{\ell} \times \mathbf{r}}{|\mathbf{r}|^3}, \tag{3.2}$$

where $\mathrm{d}\boldsymbol{\ell}$ is the wire element along the path in the direction of the current I, $\mathbf{r}$ is the displacement vector from the wire element $\mathrm{d}\boldsymbol{\ell}$ to the point P at

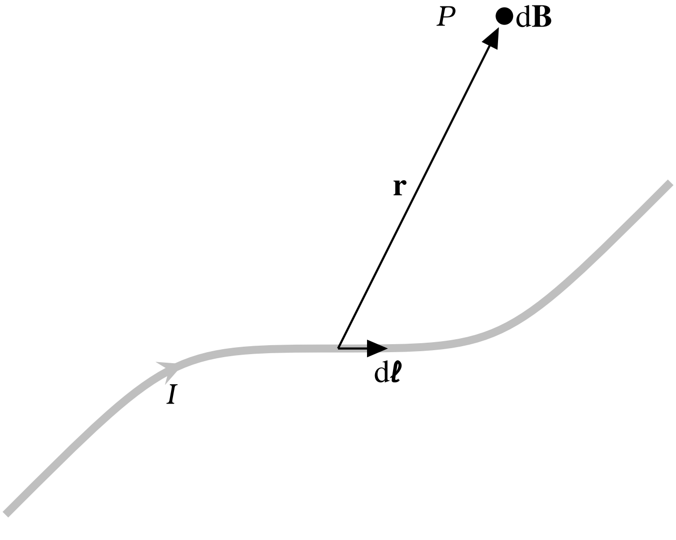

Figure 3.3: Illustration of the Biot–Savart law. A current I flows through a wire path, $\mathbf{r}$ is the displacement vector from the wire element $\mathrm{d}\boldsymbol{\ell}$ to the point P, where the magnetic field $\mathrm{d}\mathbf{B}$ is calculated.

which the magnetic field is calculated, $\mu_0 = 4\pi \times 10^{-7}\,\mathrm{H/m}$ is the vacuum permeability. The direction of the d**B** can be determined by applying the right-hand rule to the vector product $\mathrm{d}\boldsymbol{\ell} \times \mathbf{r}$. The Biot-Savart law can, in principle, be used for any configuration of current paths, where the generated magnetic field is evaluated by a line integral. In the following, different geometry of wire loops is studied. For simplicity, the wire is assumed to be infidelity thin, i.e., the cross-section of the wire is neglected.

Circular Loop

Fig. 3.4 shows a circular wire loop of radius R in the y-z plane. The x-component of the magnetic field generated at the point P on the x-axis is calculated as:

$$B_x = \frac{\mu_0 I}{4\pi} \cdot \frac{2\pi R}{R^2 + x^2} \cdot \cos\theta$$

$$= \frac{\mu_0 I}{2} \cdot \frac{R^2}{(R^2 + x^2)^{3/2}}\,, \tag{3.3}$$

where θ is the angle between the displacement vector **r** and the y-z plane, x is the coordinate of P on the x-axis, and I is the current flowing in the loop.

Rectangular Loop

For a rectangular wire loop carrying current I, as shown in Fig. 3.5, of side dimensions $2a$ by $2b$ and bisected by the y-axis and z-axis, the x-component of the magnetic field generated at the point P on the x-axis can be written as [57]:

$$B_x = \frac{\mu_0 I a b}{\pi l}\left(\frac{1}{l^2 - a^2} + \frac{1}{l^2 - b^2}\right), \tag{3.4}$$

where

$$l = \sqrt{a^2 + b^2 + x^2}$$

is the distance from the corners of the loop to P, and x is the coordinate of P on the x-axis.

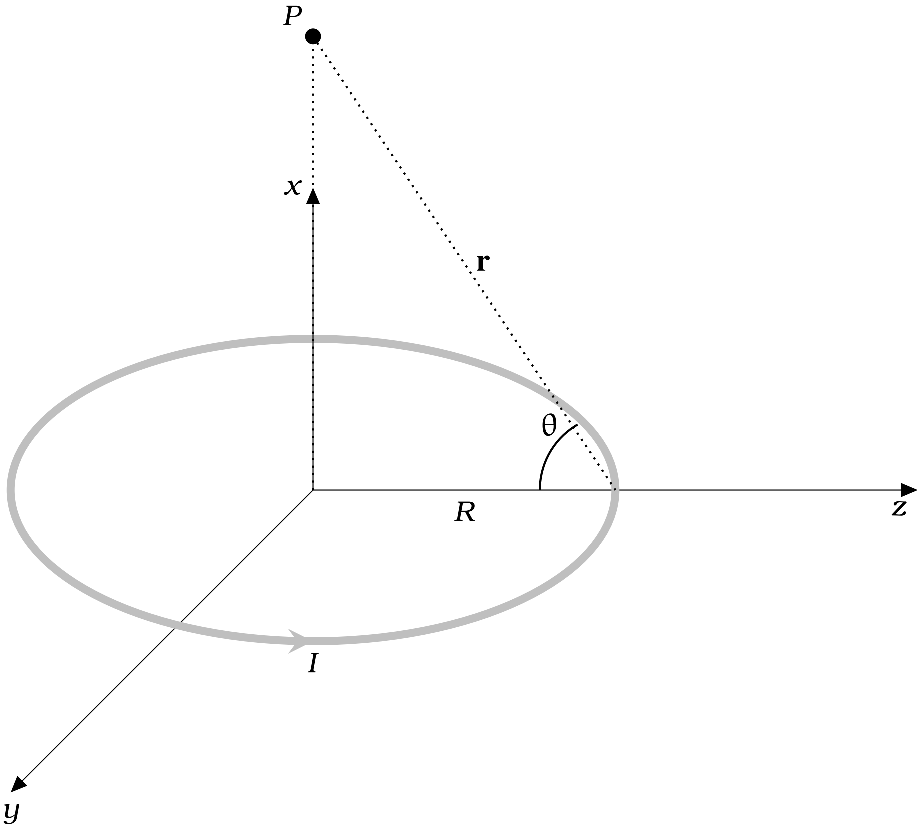

Figure 3.4: Geometry of a circular wire loop. I is the current flowing in the loop; R is the radius; θ is the angle between the displacement vector $\mathbf{r}$ and the plane of the circular loop; P is the point on the x-axis, where the magnetic field is evaluated.

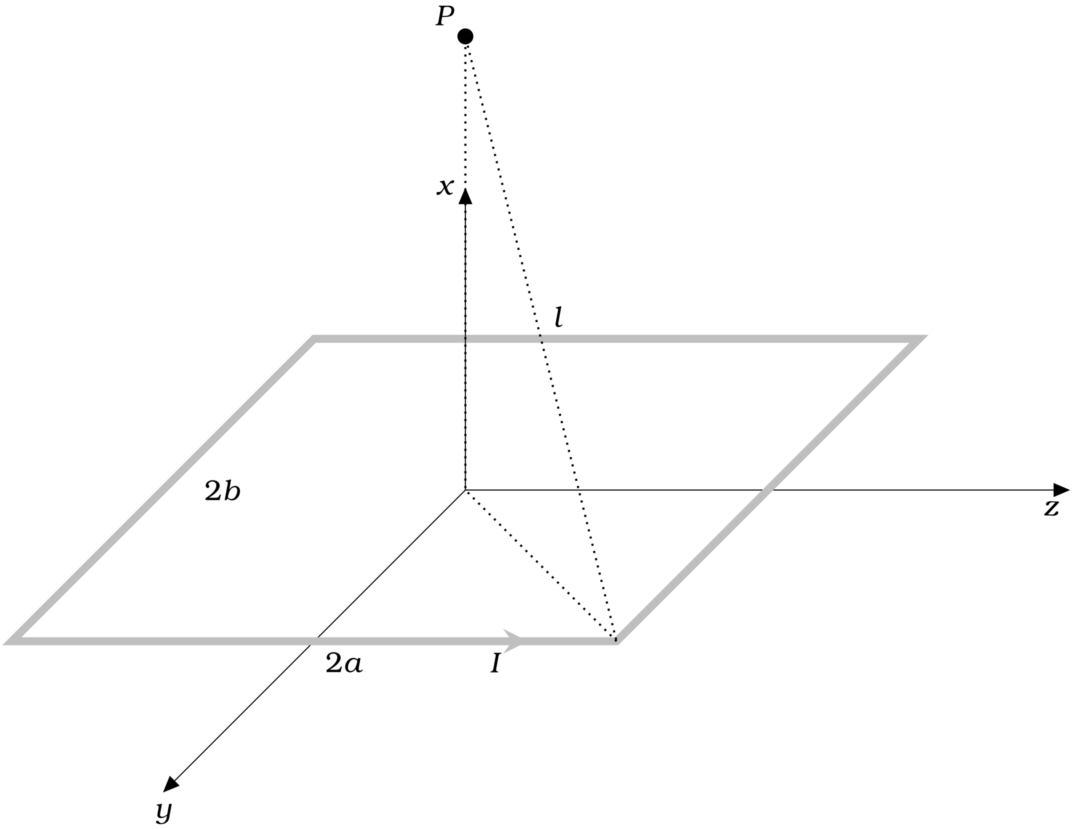

Figure 3.5: Geometry of a rectangular wire loop. I is the current flowing in the loop; $2a$ and $2b$ are the side dimensions; l is the distance from the corners of the loop to the point P, where the magnetic field is evaluated.

Quasi-rectangular Loop

A quasi-rectangular coil is shown in Fig. 3.2(g). In order to numerically evaluate the produced magnetic field, an arc wire path and a finite straight wire path need to be studied first. The detailed calculation is described in Appendix A. As seen in Fig. 3.6, a quasi-rectangular wire loop can be considered as a combination of a rectangular wire and two arc wires subtracting two straight line wires. Therefore, the produced magnetic field is evaluated as

$$\mathbf{B} = \mathbf{B}_{\text{rectangle}} + 2\mathbf{B}_{\text{arc}} - 2\mathbf{B}_{\text{line}} \, . \tag{3.5}$$

The rectangular wire in the x-z plane has its center at the origin O and the side dimensions $2a$ by $2b$. Each arc wire parallel with the x-y plane has a radius R and subtends an angle π. Each subtracted line wire of length $2R$ is parallel to the x-axis. From Eq. (3.4), Eq. (A.4) and Eq. (A.6), the y-component of the magnetic field at the point P on the y-axis is given as

$$B_{\text{rectangle}} = \frac{\mu_0 I a b}{\pi l}\left(\frac{1}{l^2 - a^2} + \frac{1}{l^2 - b^2}\right) , \tag{3.6}$$

$$B_{\text{arc}} = \frac{\mu_0 I R b}{4\pi} \int_0^{\pi} \frac{\sin\theta \, \mathrm{d}\theta}{(R^2 + y^2 + b^2 - 2Ry\sin\theta)^{3/2}} , \tag{3.7}$$

$$B_{\text{line}} = \frac{\mu_0 I}{2\pi k} \cdot \frac{R\cos\alpha}{\sqrt{R^2 + k^2}} = \frac{\mu_0 I}{2\pi k^2} \cdot \frac{Rb}{\sqrt{R^2 + k^2}} , \tag{3.8}$$

where

$$l = \sqrt{a^2 + b^2 + y^2}$$

is the distance from the corners of the rectangular loop to P,

$$k = \sqrt{b^2 + y^2}$$

is the distance from the midpoint Q of the line wire to P, y is the coordinate of P on the y-axis, θ is the subtended angle of the arc, and α is the angle between $\overline{PQ}$ and $\overline{QO}$. Note that the notations are changed in accordance with that in Fig. 3.6.

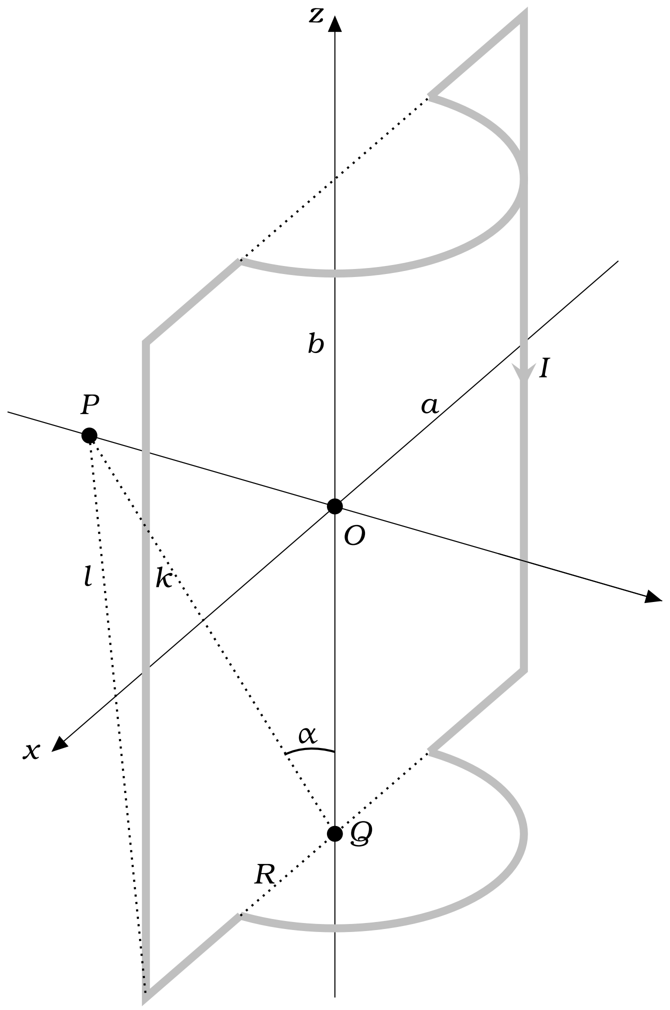

Figure 3.6: Geometry of a quasi-rectangular wire loop. It is a combination of a rectangular wire of side dimensions $2a$ by $2b$, and two arc wires each with a radius R and subtending an angle π, subtracting two straight line wires each of length $2R$. I is the current flowing in the wire; P is the point where the magnetic field is evaluated; l is the distance from the corners of the rectangular wire to P; k is the distance from the midpoint Q of the line wire to P; α is the angle between $\overline{PQ}$ and $\overline{QO}$.

Quasi-circular Loop

Fig. 3.7 shows a quasi-circular wire loop, which is a combination of a circular wire (partial) and two arc wires. The produced magnetic field is evaluated as

$$\mathbf{B} = \mathbf{B}_{\text{circle}} + 2\mathbf{B}_{\text{arc}} \,. \tag{3.9}$$

The partial circular wire of radius R' is in the x-z plane and centered at the origin O. Each arc wire in parallel with the x-y plane has a radius R and subtends an angle π. From Eq. (3.3) and Eq. (A.4), the y-component of the magnetic field at the point P on the y-axis is given as

$$B_{\text{circle}} = \frac{\mu_0 I}{2} \cdot \frac{R'^2}{(R'^2 + y^2)^{3/2}} \cdot \frac{\pi - \arcsin(R/R')}{\pi} \,, \tag{3.10}$$

$$B_{\text{arc}} = \frac{\mu_0 I R b}{4\pi} \int_0^{\pi} \frac{\sin\theta \, d\theta}{(R^2 + y^2 + b^2 - 2Ry\sin\theta)^{3/2}} \,, \tag{3.11}$$

where

$$b = \sqrt{R'^2 - R^2}$$

is the distance from the center of the arc wire to O, y is the coordinate of P on the y-axis, and θ is the subtended angle of the arc. Note that the notations are changed in accordance with that in Fig. 3.7.

Curved Rectangular Loop

As seen in Fig. 3.8, a curved rectangular wire loop is a combination of two straight wires and two arc wires. The produced magnetic field is written as

$$\mathbf{B} = 2\mathbf{B}_{\text{arc}} + 2\mathbf{B}_{\text{line}} \,. \tag{3.12}$$

The straight wires each of length $2b$ are parallel to the z-axis and bisected by the x-y plane. From Eq. (A.6), the y-component of the magnetic field at the point P on the y-axis is

$$B_{\text{line}} = \frac{\mu_0 I}{2\pi k} \cdot \frac{b\sin\alpha}{\sqrt{b^2 + k^2}} = \frac{\mu_0 I}{2\pi k^2} \cdot \frac{ab}{\sqrt{b^2 + k^2}} \,, \tag{3.13}$$

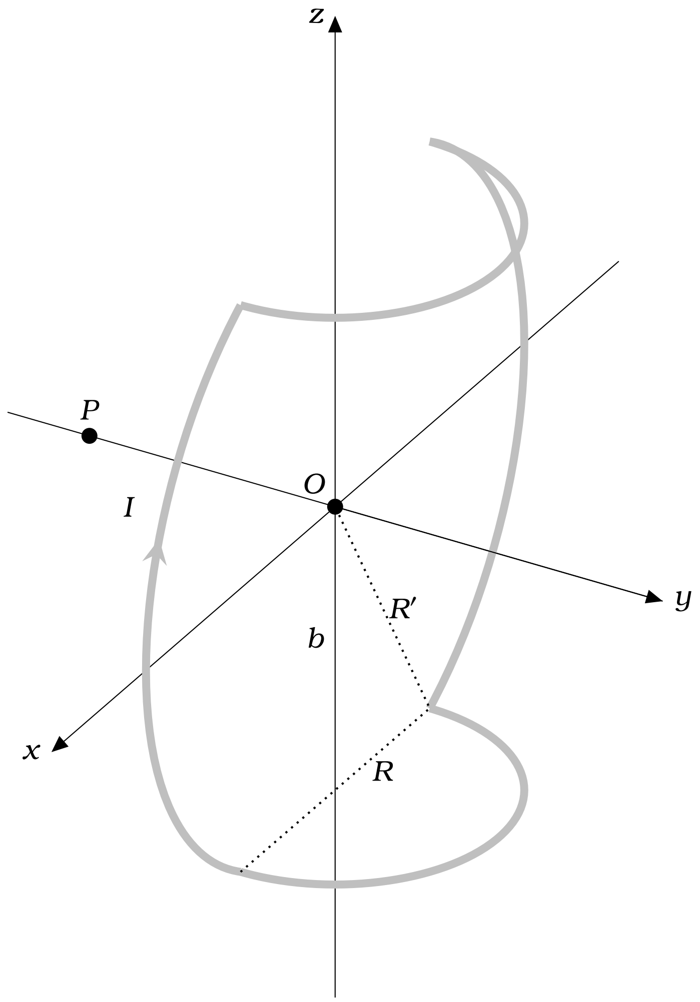

Figure 3.7: Geometry of a quasi-circular wire loop. It is a combination of a partial circular wire with a radius R', and two arc wires each with a radius R and subtending an angle π. I is the current flowing in the wire; P is the point where the magnetic field is evaluated.

where

$$k = \sqrt{(\sqrt{R^2 - a^2} - y)^2 + a^2}$$

is the distance from P to the midpoint Q of the line wire, a is the distance from Q to the y-axis, R is the radius of the arc wire, and α is the angle between $\overline{QP}$ and the y-axis. The arc wires, each with a radius R and subtending an angle 2φ, are parallel to the x-y plane. From Eq. (A.4), the y-component of the magnetic field produced by the arc is written as

$$B_{\mathrm{arc}} = \frac{\mu_0 I R b}{4\pi} \int_{-\varphi}^{\varphi} \frac{\cos\theta \, \mathrm{d}\theta}{(R^2 + y^2 + b^2 - 2Ry\cos\theta)^{3/2}}\,, \tag{3.14}$$

Note that the notations are changed in accordance with that in Fig. 3.8.

Curved Circular Loop

A curved circular loop is shown in Fig. 3.9. A circular coil of radius R' is wrapped on a cylinder of radius R. Its projection in the x-z plane is an ellipse of semi-major axis R and semi-minor axis a. Its projection in the x-y plane is an arc that has a radius R and subtends an angle 2φ. According to the parametric equation of the ellipse, the x-coordinate and the z-coordinate of a wire element $\boldsymbol{\ell}$ on the wire loop are given as

$$(x, z) = (a \sin t, R' \cos t)\,, \qquad \text{for} \quad 0 \le t \le 2\pi\,.$$

The length of the projected arc equals the diameter of the curved circular loop $2R'$. Hence, the subtended angle is calculated as $\varphi = R'/R$. Then, the y-coordinate of the wire element $\boldsymbol{\ell}$ is

$$y = \sqrt{R^2 - a^2 \sin^2 t} - \sqrt{R^2 - a^2}\,.$$

Therefore, an infinitely small increment of the wire element is

$$\mathrm{d}\boldsymbol{\ell} = \Big(a \cos t, -\frac{a^2 \sin t \cos t}{\sqrt{R^2 - a^2 \sin^2 t}}, -R' \sin t\Big)\,\mathrm{d}t\,. \tag{3.15}$$

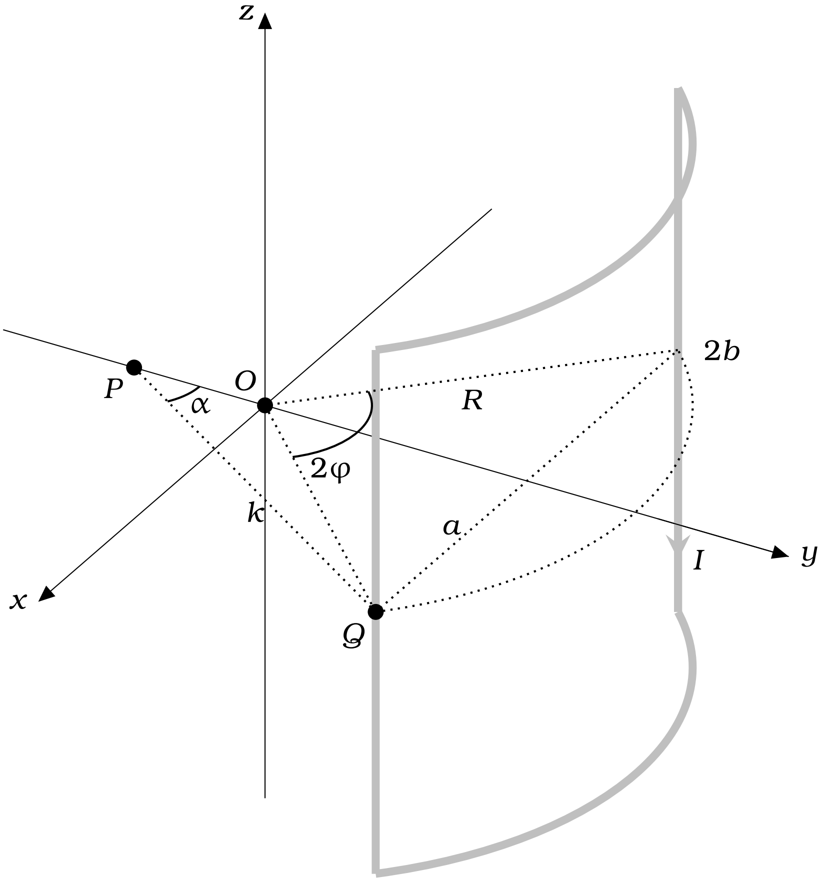

Figure 3.8: Geometry of a curved rectangular wire loop. It is a combination of two straight line wires and two arc wires. The straight wires each of length $2b$ are parallel to the z-axis and bisected by the x-y plane. The arc wires, each with a radius R and subtending an angle 2φ, are parallel to the x-y plane. I is the current flowing in the wire; P is the point where the magnetic field is evaluated; k is the distance from P to the midpoint Q of the line wire; α is the angle between $\overline{QP}$ and the y-axis; a is the distance from Q to the y-axis.

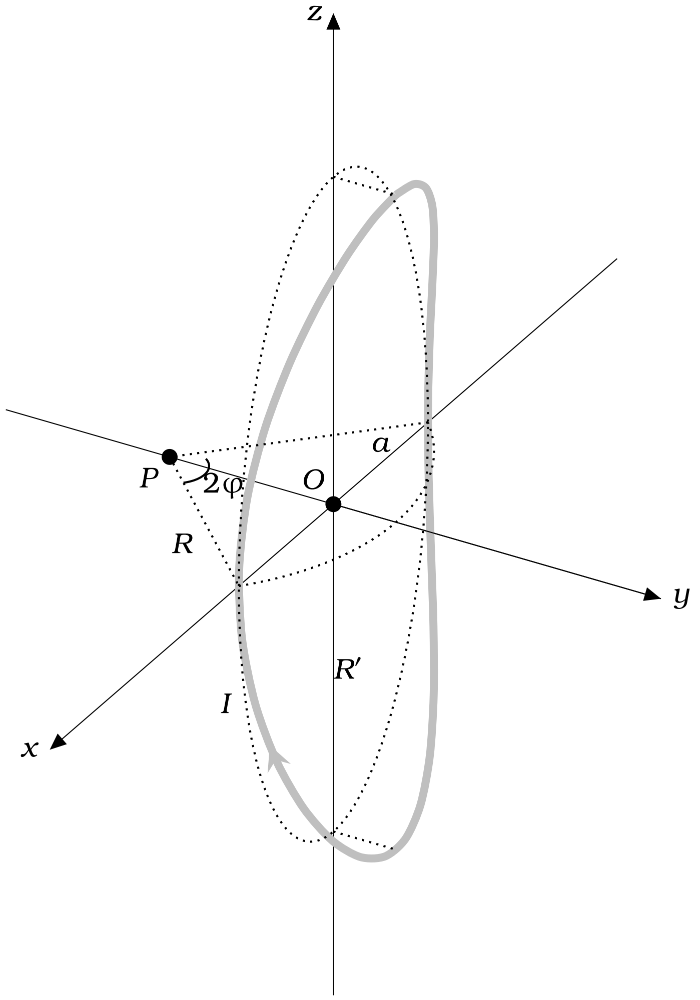

Figure 3.9: Geometry of a curved circular wire loop. A circular coil of radius R' is wrapped on a cylinder of radius R. Its projection in the x-z plane is an ellipse of semi-major axis R' and semi-minor axis a. Its projection in the x-y plane is an arc with a radius R and subtends an angle 2φ. I is the current flowing in the wire; P is the point where the magnetic field is evaluated.

The magnetic field is calculated at the point $P(0, y_\mathrm{p}, 0)$ on the y-axis. The displacement vector $\mathbf{r}$ from the wire element $\boldsymbol{\ell}$ to P is

$$\mathbf{r} = (-a \sin t, y_\mathrm{p} - \sqrt{R^2 - a^2 \sin^2 t} + \sqrt{R^2 - a^2}, -R' \cos t)\,. \tag{3.16}$$

Substituting Eq. (3.15) and Eq. (3.16) into Eq. (3.2), the contribution of the current I in the curved circular wire to the y-component of the magnetic field at P is written as

$$B_\mathrm{y} = \frac{\mu_0 I}{4\pi} \int_0^{2\pi} \frac{aR' \,\mathrm{d}t}{(x^2 + (y_\mathrm{p} - y)^2 + z^2)^{3/2}}\,, \tag{3.17}$$

where $a = R \sin(R'/R)$.

3.1.3 Coil Simulation

After numerically expressing the produced magnetic fields from wire loops of different geometries, they were implemented into the MATLAB (The MathWorks, Massachusetts, United States) codes. A coil was considered a combination of multiple wire loops of the same geometry without a span between them. Hence, the magnetic field produced by a coil could be simulated. For a defined magnetic field, the geometrical size of the coil was then optimized regarding the powerloss and field homogeneity.

In the simulation program, the magnetic field generated by each loop is calculated with the unit current. After adding up the magnetic field at the observation point, the magnetic field produced by the coil is known. The necessary current for producing a desired magnetic field is then calculated by proportion. The total wire length used in the coil is calculated by adding the wire length of each wire loop. Additionally, with a known wire resistance, the resistance of the coil can then be calculated. Thus, the powerloss of the coil for producing the desired magnetic field is calculated by the current and the coil resistance. Moreover, with a known current, the produced magnetic field along the axis of the simulated coil is calculated to examine the field homogeneity. In the program, the diameter of the wire is required. So, the size of the coil is increased by iteratively adding a wire loop. For different sizes of coils, the powerlosses and homogeneities are compared to find the optimum.

The central bore was pre-determined to have at least 13 mm radius, which was reserved for fitting the receive coils and the components of the temperature control unit. A Litz wire manufactured by Elektrisola (Reichshof-Eckenhagen, Germany) was used for building the coil, which has 1000 × 0.05 mm strands and 2 mm diameter. The Litz wire has a conduct cross-section of $1.9635\,\mathrm{mm}^2$ and $9.2\,\mathrm{m\Omega/m}$ resistance. According to experience, the wire could safely carry a current up to 16 A. The target magnetic field generated at the point of observation is $20\,\mathrm{mT}/\mu_0$. Note that in the simulation, only the DC resistance of the coils was taken into calculating the powerloss.

T$_x$-coil

See Fig. 3.1, the central T$_x$-coil is a single solenoid coil whose cross-section could be either circular or rectangular. If comparing the powerloss of a circular loop and a rectangular loop, one gets

$$\frac{P_{circle}}{P_{rectangle}} = \frac{I_{circle}^2 \cdot 2\pi R \cdot \rho}{I_{rectangle}^2 \cdot 2 \cdot (2a + 2b) \cdot \rho}, \tag{3.18}$$

where ρ is the wire resistance per unit length. Let the side dimensions $2a$ and $2b$ of the rectangular loop be equal, and let the diameter $2R$ of the circular loop equal the side dimension, one gets $a = R$. When produce the same magnetic field, by substituting Eq. (3.3) and Eq. (3.4) into Eq. (3.18), the powerloss ratio is written as

$$\begin{aligned}\frac{P_{circle}}{P_{rectangle}} &= \left(\frac{4\sqrt{R^2 + x^2}}{\pi\sqrt{2R^2 + x^2}}\right)^2 \cdot \frac{2\pi R}{8R} \\ &= \frac{4(R^2 + x^2)}{\pi(2R^2 + x^2)},\end{aligned} \tag{3.19}$$

where x is the coordinate of the observation points on the x-axis. Let $P_{circle} < P_{rectangle}$, from Eq. (3.19) one gets

$$\frac{x}{R} < \sqrt{\frac{2\pi - 4}{4 - \pi}} \approx 1.63\,. \tag{3.20}$$

Eq. (3.20) indicates that if x is less than $1.63R$, the circular loop has less powerloss than the rectangular loop. Since the observation point is located at the center of the T_x-coil and the length of the coil is limited, a circular solenoid is chosen in preference to a rectangular solenoid. Another advantage is that, when winding the coils, it is much easier to wind into a circle than into a rectangle.

Circular solenoid coils were simulated and compared. The result showed that a circular solenoid with 13 mm inner radius, 82 mm outer radius, and 48 mm length had the minimum powerloss of 5.96 W. The current flowing in the coil was 3.37 A, and the number of windings was 336. As mentioned in Section 3.1.1, coils in a bigger dimension can bring more complexities to the fabrication. Building a coil with 336 number of windings was impossible in our laboratory due to the manufacturing process, which will be addressed in Section 3.1.4. It was necessary to limit the number of windings into a resalable range, which in this study was 50. Another restriction was that the number of windings in the axial direction of the coils should be an even number, only then could the two wire terminals be reached from the outer layer of the coils.

Under all mentioned restrictions, the optimized T_x-coil had 13 mm inner radius, 23 mm outer radius, and 20 mm length. By applying 12.94 A current, it produced a $20\,\mathrm{mT}/\mu_0$ magnetic field at the center point. The powerloss was 8.71 W and the number of winding was 50. Note that in the design of a multiply dimensional coil setup, the size of the T_x-coil would influence the distance and the dimension of the T_y-coils and T_z-coils. Thus, the results given here are for determining the shape of the T_x-coil, which is a single circular solenoid.

T_y-coils

The T_y-coils were a pair of Helmholtz-like coils, so the sample chamber in the T_x-coil could be easily accessed. In the simulation, six different shapes of the coil were implemented, which were circular, curved circular, quasi-circular, rectangular, curved rectangular, and quasi-rectangular coil. As the T_x-coil had been determined to be a single circular solenoid with 13 mm inner diameter, only the length and the outer diameter of the coil were modified in the simulation program. The T_y-coils were set as close as possible to the center point, where the magnetic field was calculated. The inner dimensions of the T_y-coils were set as small as possible just to fit the T_x-coil inside. By increasing the outer diameter of the T_x-coil with a step of the wire diameter (2 mm), all possible sizes of the T_x-coil and the accordant T_y-coils were compared with their total powerlosses.

The results are shown in Fig. 3.10. The coil setups with regular circular and rectangular T_y-coils have clearly higher powerlosses. Their plots are discontinued because the simulation program cannot find solutions when the outer radius of the T_x-coil is bigger than 23 mm. The coil setups with quasi-shape of coils have less powerloss than those with the curved shape of coils. In Fig. 3.11, the simulated magnetic fields along the axis of different T_y-coils are plotted. For each coil setup, the dimensions of the coils and the currents flowing in them are chosen at the lowest total powerloss. Fig. 3.11 shows that the curved shape of coils produces the magnetic fields with the best homogeneity. The quasi-rectangular coils produce a magnetic field with slightly worse homogeneity. However, due to its advantage of less powerloss, the T_y-coils were determined to be quasi-rectangular.

The optimized coil setup, with the lowest total powerloss of 36.82 W, consisted of a circular T_x-coil with 13 mm inner radius, 21 mm outer radius, and 20 mm length, and a pair of quasi-rectangular T_y-coils with 42 mm by 20 mm inner side dimension, 74 mm by 52 mm outer side dimension, 12 mm length, and 13 mm arc radius. If one designs a 2D coil setup, the optimized size of the T_x-coil and T_y-coils stated above could be used to build the coils. However, in a 3D coil setup design, the results shown here are for relative comparison.

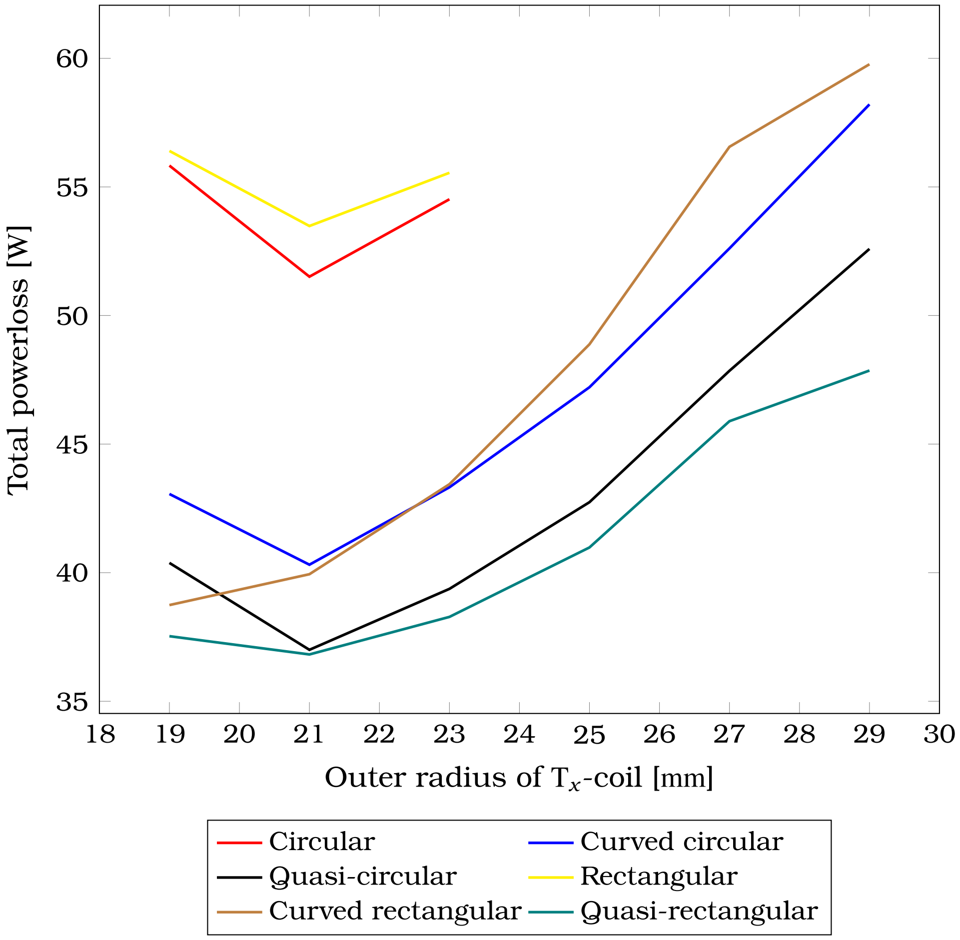

Figure 3.10: Powerloss comparison of 2D coil setups with different T_y-coils. The T_x-coil is a single circular solenoid with 13 mm inner radius. By increasing the outer diameter of the T_x-coil, the total powerloss is optimized for each shape of T_y-coils.

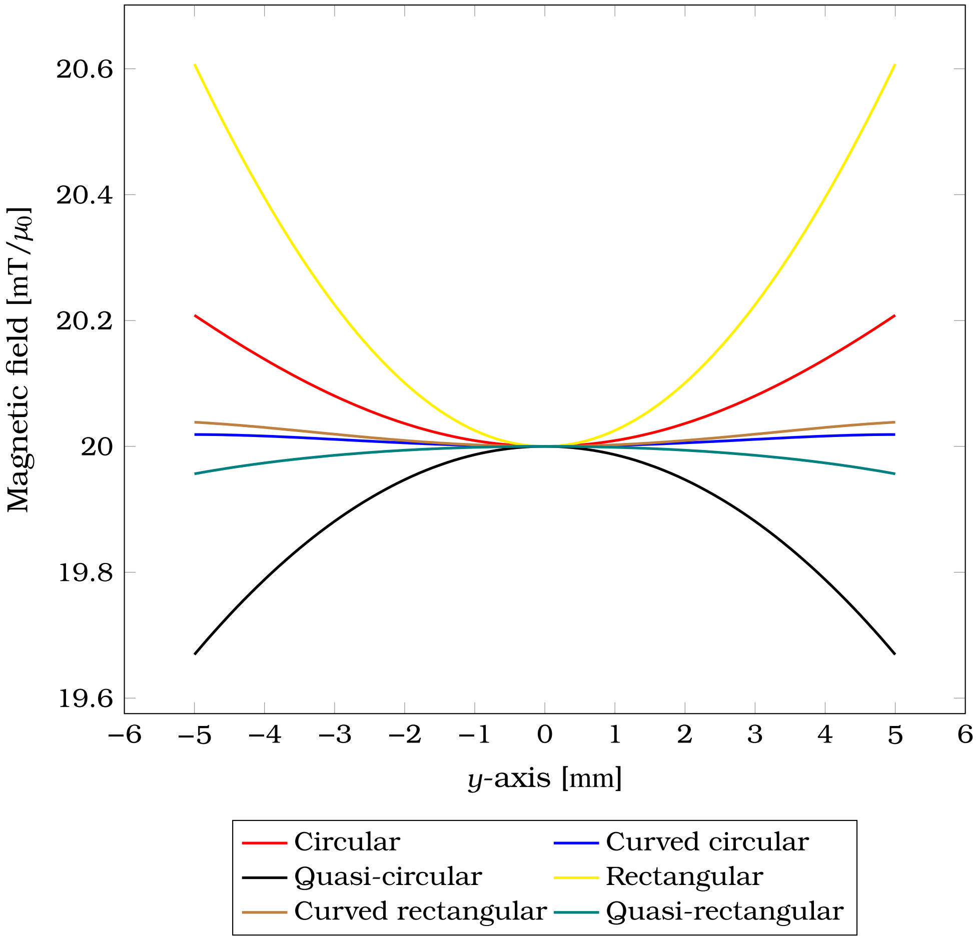

Figure 3.11: Magnetic field comparison of different T_y-coils in a 2D coil setup. The dimension of each pair of T_y-coils and the current flowing in them are chosen at the lowest total powerloss.

T_z-coils

Similar to the T_y-coils, the T_z-coils were as well a pair of Helmholtz-like coils. As noted from the simulation of the T_y-coils, the coil setups with the regular circular and rectangular coils had higher powerloss, and the homogeneity of the produced fields was also worse than other shapes of coils. Thus, in the simulation of the T_z-coils, only the curved shape and the quasi-shape of coils were compared. The T_x-coil and the T_y-coils had already been determined to be a single circular solenoid and a pair of quasi-rectangular coils, respectively. The T_y-coils and the T_z-coils were set as close as possible to the center point, and their inner dimensions were set as small as possible just to fit the inner coils. By increasing the outer diameter of the T_x-coil with a step of the wire diameter (2 mm), all possible sizes of the T_x-coil and the accordant T_y-coils and T_z-coils were compared with their powerlosses.

Fig. 3.12 shows that the coil setups with the rectangular shape of coils have a significantly lower powerloss. The simulated magnetic fields along the axis of different T_z-coils are plotted in Fig. 3.13. For each coil setup, the dimensions of the coils and the currents flowing in them are chosen at the lowest total powerloss. The curved shape of coils generates magnetic fields with better homogeneity than the quasi-shape of coils.

The optimized total powerloss for a coil setup with the quasi-rectangular T_z-coils was 82.82 W, and that was 82.52 W with the curved rectangular T_z-coils. Due to the advantages of less powerloss and better field homogeneity, the T_z-coils were determined to be curved rectangular.

The optimized coil setup consisted of a circular T_x-coil with 13 mm inner radius, 21 mm outer radius, and 20 mm length; a pair of quasi-rectangular T_y-coils with 42 mm by 20 mm inner side dimension, 74 mm by 52 mm outer side dimension, 12 mm length, and 13 mm arc radius; a pair of curved rectangular T_z-coils with 52 mm inner side length, 48.00 mm inner arc length, 76 mm outer side length, 72.00 mm outer arc length, 16 mm length, and 47.50 mm curvature radius. For the T_x-coil, the current was 15.56 A and the powerloss was 9.51 W; for the T_y-coils, the current was 11.92 A and the powerloss was 27.31 W; for the T_z-coils, the current was 14.44 A and the powerloss was

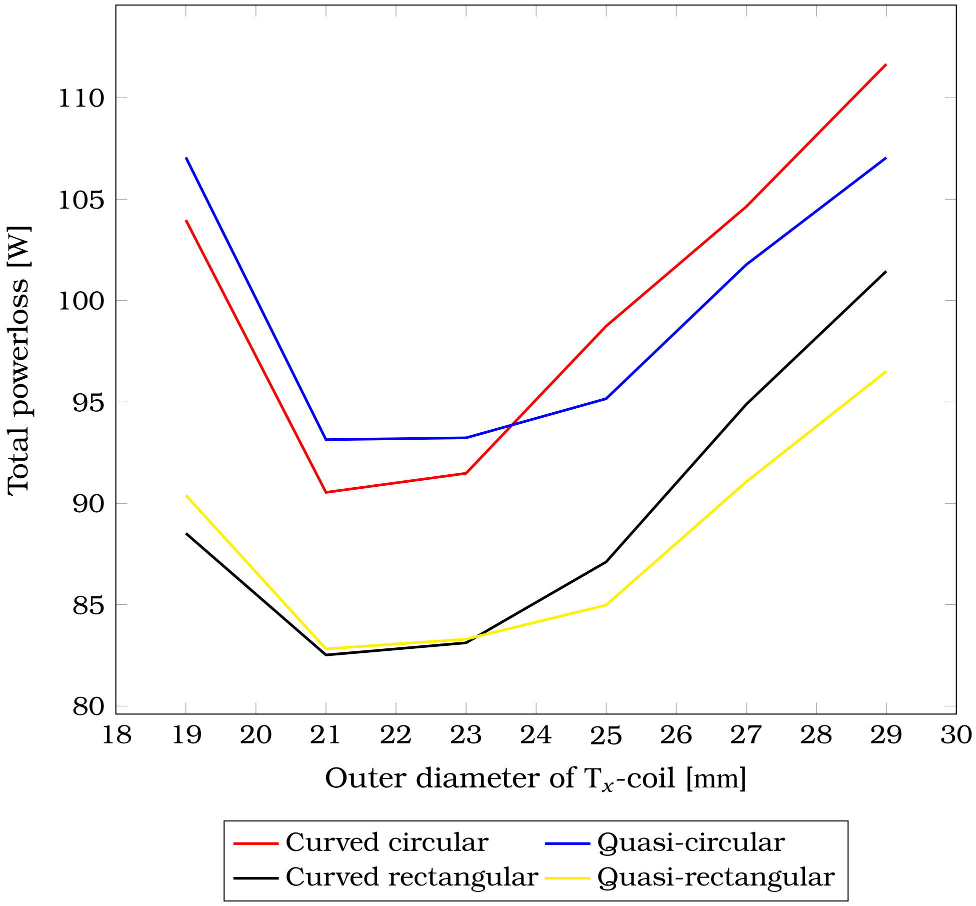

Figure 3.12: Powerloss comparison of 3D coil setups with different T_z-coils. The T_x-coil is a single circular solenoid with 13 mm inner radius, and the T_y-coils are a pair of quasi-rectangular coils. By increasing the outer diameter of the T_x-coil, the total powerloss is optimized for each shape of T_z-coils.

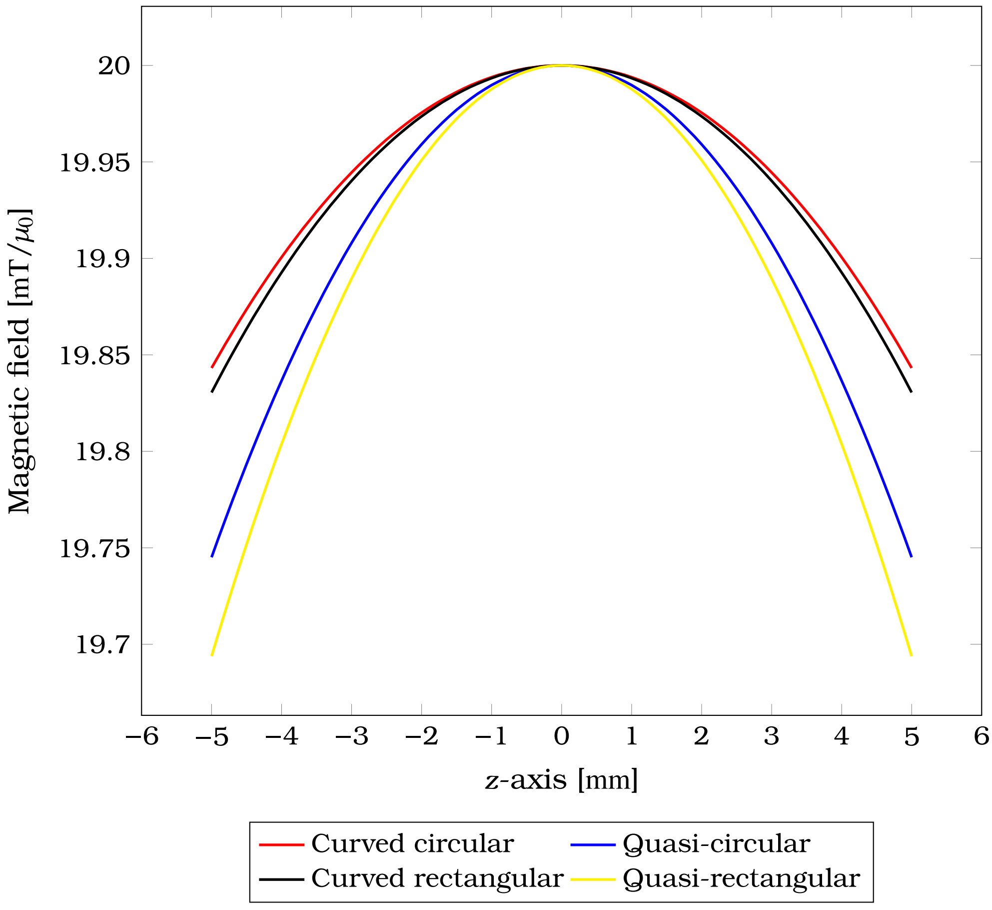

Figure 3.13: Magnetic field comparison of different T_z-coils in a 3D coil setup. The dimension of each pair of T_z-coils and the current flowing in them are chosen at the lowest total powerloss.

45.70 W. The total powerloss was 82.52 W. The mean deviation between the target magnetic field and the simulated fields were -0.1256 mT, -0.0033 mT, and -0.0143 mT in a $[-2.5, 2.5]$ mm range on the x-axis, y-axis, and z-axis, respectively.

Coil setup

During the simulation, the coils were placed as close as possible to each other, with no gap left in between. However, due to the size tolerance of the fabricated coils, the inner dimensions of the T_y-coils and T_z-coils were slightly increased. Earlier, due to a calculation error in the program, the optimized coil setup had a slight difference in dimension comparing to the aforementioned one. Unfortunately, the mistake was found after the coils were fabricated. Since the total powerloss and the homogeneity of the fields were in an acceptable range, and the manufacturing of the coils was time-consuming, the coils were not re-fabricated according to the optimized results.

The earlier optimized coil setup, including size tolerance, has a circular T_x-coil with 13 mm inner radius, 23 mm outer radius, and 16 mm length; a pair of quasi-rectangular T_y-coils with 51 mm by 17.5 mm inner side dimension, 83 mm by 49.5 mm outer side dimension, 12 mm length, and 13 mm arc radius; a pair of curved rectangular T_z-coils with 53 mm inner side length, 54.10 mm inner arc length, 85 mm outer side length, 86.10 mm outer arc length, 12 mm length, and 69.00 mm curvature radius. For the T_x-coil, the current was 15.41 A and the powerloss was 9.89 W; for the T_y-coils, the current was 12.55 A and the powerloss was 32.08 W; for the T_z-coils, the current was 15.14 A and the powerloss was 56.29 W. The total powerloss was 98.26 W. The mean deviation of the magnetic fields were -0.1465 mT, -0.0116 mT, and -0.0172 mT in a $[-2.5, 2.5]$ mm range on the x-axis, y-axis, and z-axis, respectively. A demonstration of the 3D models of the optimized coil setup is shown in Fig. 3.14.

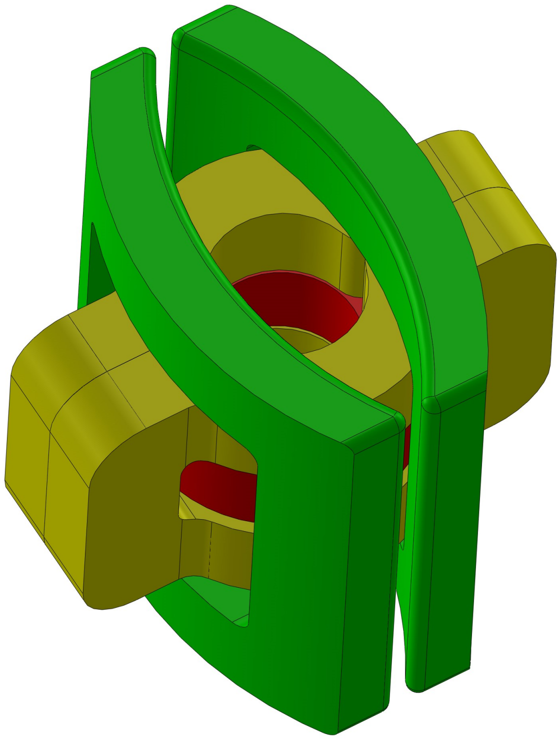

(a) Coil assembly

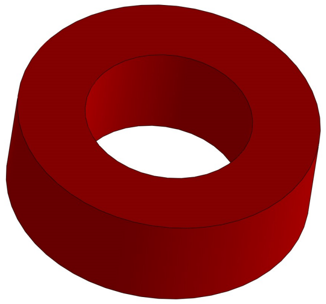

(b) T$_x$-coil

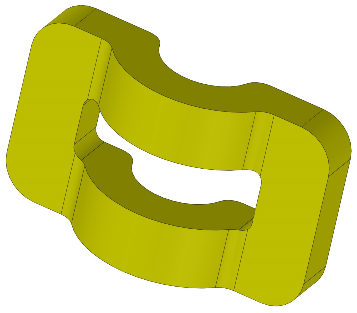

(c) T$_y$-coil

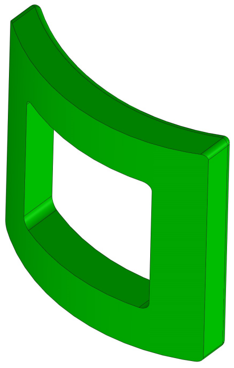

(d) T$_z$-coil

Figure 3.14: 3D models of the optimized coil setup. The coil assembly (a) consists of a single circular T$_z$-coils (b), a pair of quasi-rectangular T$_y$-coils (c), and a pair of curved rectangular T$_z$-coils (d). Note the scale is not in proportion.

3.1.4 Coil Fabrication

The fabrication was done manually in the laboratory. Coil molds were indispensable parts in which the coils were wound into different shapes. The computer-aided design (CAD) models of the coil mold for winding the T_y-coils are shown in Fig. 3.15. It consists of four parts: the frame part confines the outer dimension of the coil, the core part defines the inner dimension, and the base and the top parts are used to press the coils in between to form the shape of the coils. The coil molds for winding the T_x-coils and T_z-coils were similar to the ones for T_y-coils; only the shape of the molds was modified in accordance with the dimensions of the coils. The molds were designed in SOLIDWORKS (Dassault Systèmes, Massachusetts, United States), and they were produced in a local workshop. The material used to produce the coil molds was polyoxymethylene (POM), which was a common polymer characterized by its high stiffness and dimension stability.

Any ferromagnetic material should be excluded from the process of fabricating the coils, because the residual material particles may contaminate the particle signals. While winding the coils in the mold, a dual-component epoxy adhesive Epoxy Ultra Strong (UHU, Bühl, Germany) was used to bond the wires to keep the shape after the process. This adhesive has a cure time of 90 min at room temperature, i.e., to reach the final bonding strength. A coil with a large number of windings was challenging to build inside 90 min before the adhesive got hard. This is the reason that the numbers of winding were limited to 50 during the design of the coils. The number 50 was set based on the production speed of a proficient researcher. After finishing the winding of the coils, the top part of the mold was pressed into the frame part by a pressing machine. It formed the coils into the designed dimension. The mold was removed after approximately 12 h when the adhesive reached its final bonding strength. Theoretically, the epoxy adhesive could not bond to the POM. However, because of the rough surface of the coil, the mold was still difficult to remove. Hence, a household-used cling film Frischhaltefolie (Toppits, Minden, Germany), which is made of polyethylene, was placed between the mold and the coil to ensure easy removal of the mold after the adhesive was cured.

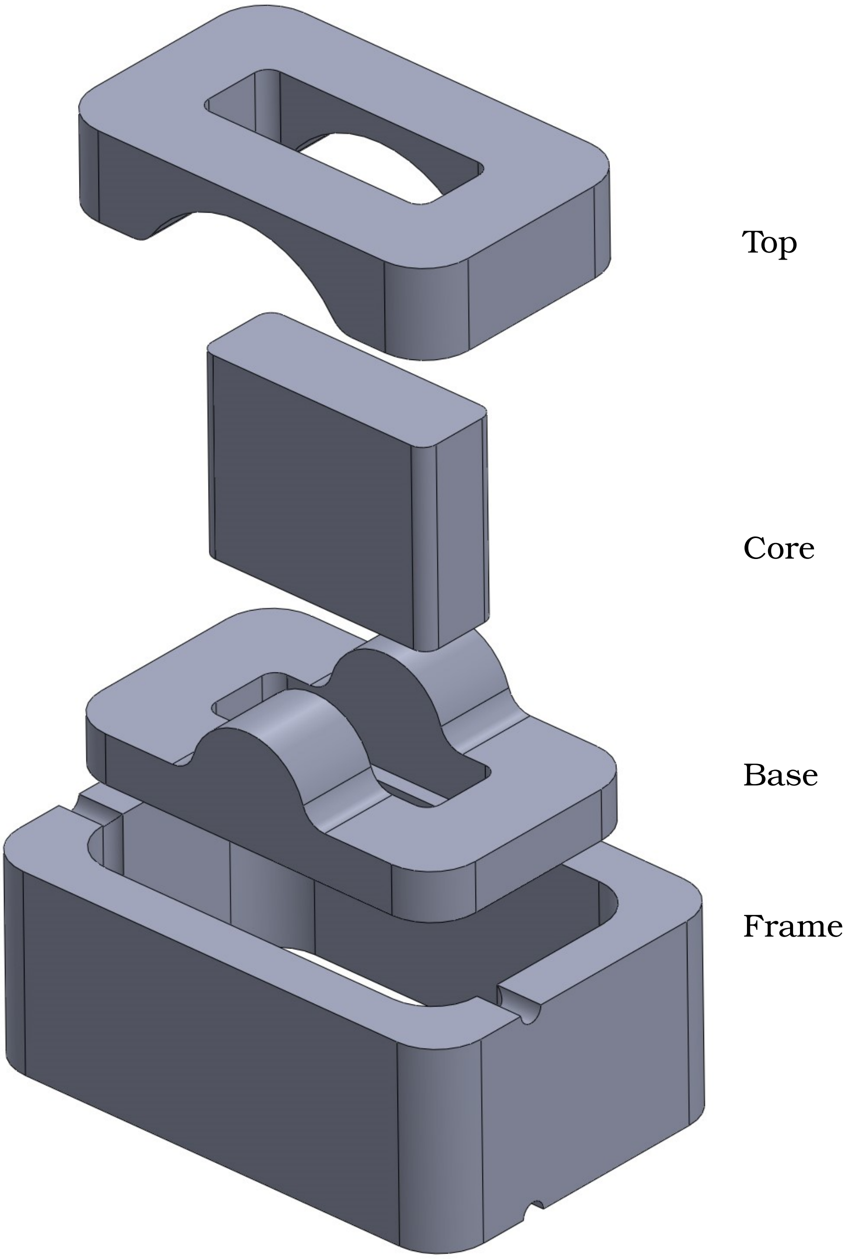

Figure 3.15: CAD models of the T_y-coil mold. The coil mold consists of four parts: the frame part confines the outer dimension of the coil, the core part defines the inner dimension, and the base and the top parts are used to press the coils in between to form the shape of the coils.

An assembly of the fabricated coils is shown in Fig. 3.16. After removing the mold, a visual inspection was conducted to examine the coils:

- no broken or overlapped wires;
- gap between the wires should not exceed 1 mm;
- the dimension tolerance of the coils should be less than 0.5 mm.

These criteria were followed during the inspection to maintain the quality of the coils. Due to the pressing process during the fabrication, some strands in the wire may be broken. However, it could not be easily seen with bare eyes. Therefore, the resistance and the inductance of the coils were measured to compare with each other. Any coils with abnormal values would be excluded. As mentioned in Section 2.3.3, two identical coil setups needed to be built. In reality, it is not possible to build exactly the same coils. Therefore, the same shape of coils was fabricated three or four times, from which two with closer electrical properties were selected.

Figure 3.16: Assembly of the fabricated transmit coils. A dual-component epoxy adhesive is used to bond the wires during the winding of the coils.

3.1.5 Coil Frame

In order to fix the positions of the transmit coil and improve the efficiency of the air cooling, a coil frame was designed. It sealed the coil setup inside and let the air only go through from the bottom to the top of the frame.

In Fig. 3.17, the CAD models of the coil frame are shown. The coil fixators are used to fix the relative positions of the transmit coils; the top and bottom frames enclose the coils and guide the air to flow through the surface of the coils; the top and bottom plates have mounting holes in them, which are used for assembly and attaching extra accessories; the frame base is for adjusting the vertical positions of the coils; the air guider part is an adapter to connect the active air cooling device (e.g., fans) to the coil frame. The parts of the frame were printed by Ultimaker 2 (Ultimaker, Utrecht, Netherlands) with the PLA (polylactic acid) material. The 3D printed frame is shown in Fig. 3.17(c). Because the coil fixators were directly attached to the coils, they were printed by Projet 3510 HD Plus (3D Systems, South Carolina, United States), due to the mechanical stability and the high-temperature tolerance of the material.

3.1.6 Results and Discussion

After fabrication, a DC current was applied separately on the coil or pair of coils to generate $20\,\mathrm{mT}/\mu_0$ magnetic field at the central point. The results were 15.5 A, 13.0 A and 15.5 A for T_x-coil, T_y-coils and T_z-coils, respectively. Additionally, with the measured resistance of the transmit coil, the powerloss of the fabricated coils was calculated. In Table 3.1, the powerloss of the simulated and fabricated coils are compared. Note that the simulated coils here include the leading cables. The T_y-coils and T_z-coils are consistent with the simulated results, while for T_x-coil the deviation is relatively big. However, the absolute deviation is in an acceptable range. Compared to the 32 % deviation from the earlier simulation method [25], the new approach is a comprehensive improvement. Note that the powerloss results from Fig. 3.2 cannot be compared with that in Table 3.1 because the bore size differs in both studies.

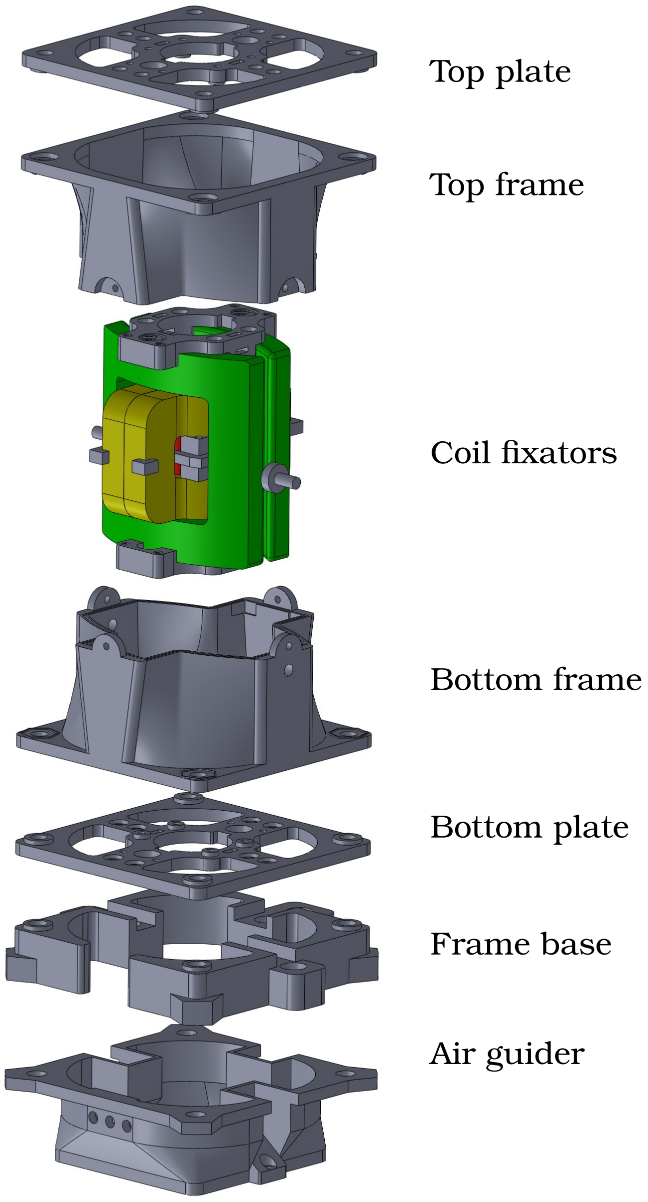

(a) CAD models (exploded view)

Figure 3.17: CAD models and the 3D printed coil frame. The coil frame includes coil fixators, top frame, bottom frame, top plate, bottom plate, frame base, and air guider. (a) is the exploded view of the CAD models; (b) is the assembly view of the CAD models; (c) is the 3D printed coil frame. Note the scale is not in proportion.

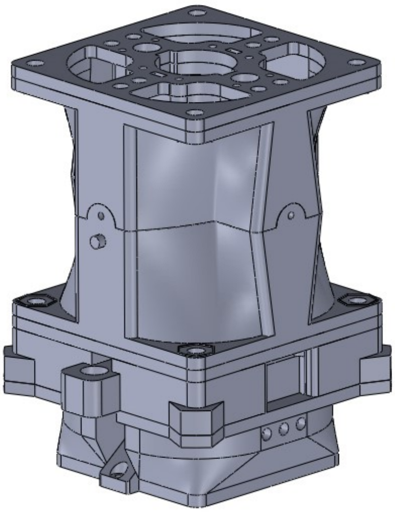

(b) (cont.) CAD models (assembly view)

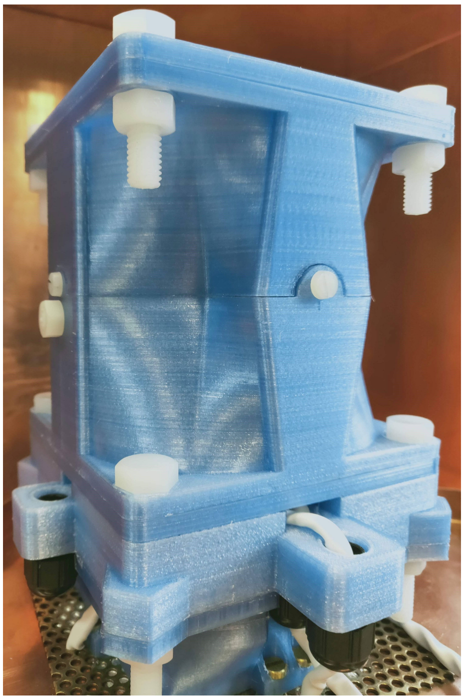

(c) (cont.) 3D printed frame

Figure 3.17 (cont.): CAD models and the 3D printed coil frame (continued).

Table 3.1: Transmit coil powerloss comparison

Coil(s)	Simulated [W]	Fabricated [W]	Deviation
T_x	12.64	14.07	11.3 %
T_y	36.72	37.87	3.1 %
T_z	62.20	66.11	6.3 %

In order to prevent the electromagnetic radiation of the transmit coils from interfering with external devices, as well as to reduce the coupling of external magnetic fields, boxes of dimension 20 cm × 20 cm × 22 cm made of 2 mm thick copper were used to shield the transmit coils. After the coils were assembled and placed into the shielding boxes, the parameters of the coils were measured. The results are shown in Table 3.2.

Table 3.2: Parameters of the transmit coils

Coil Unit	T_x		T_y		T_z	
	R [mΩ]	L [µH]	R [mΩ]	L [µH]	R [mΩ]	L [µH]
Generation	59.3	47.4	236.3	341.7	333.2	537.1
Cancellation	60.3	47.6	240.8	341.7	335.6	537.1

Noticed from Section 3.1.3, the optimized coil setup has a total powerloss of 82.52 W. Fig. 3.10 and Fig. 3.11 show that the coil setup with curved rectangular T_y-coils has a slightly higher powerloss than that with quasi-rectangular T_y-coils, and the fields have nearly the same homogeneity. If the T_y-coils in the optimized coil setup were changed from quasi-rectangular shape to curved rectangular shape, the minimum total powerloss would be 89.43 W, which is about 7 W higher. As mentioned in Section 3.1.1, active air cooling is used to cool the coils. As observed from Fig. 3.14(a) and Fig. 3.16, the curved rectangular coils have a much bigger surface area contacting the air than quasi-rectangular coils do, namely their heat dissipation rate will be higher under the same condition. Another advantage is that the curved rectangular coils are much easier to build than the quasi-rectangular coils. From these perspectives, curved rectangular T_y-coils could be taken into consideration in the future design.

3.2 Power Amplifier

The excitation signals sent from the PC cannot directly drive the transmit coils. A power amplifier is needed to amplify the power of the excitation signals so that the transmit coils can be driven to generate desired magnetic fields. In this study, the power amplifier was self-built with commercially available components.

Fig. 3.18 shows the top (a), front (b), and bottom (c) views of the power amplifier. A mains power controller, Power One R4 (Holton Precision Audio, Launceston, Australia), and a power supply unit, NXVPSU-One R1 (Holton Precision Audio, Launceston, Australia), are used. The former features a built-in inrush current limiter and low current switch on and off, and the latter rectifies the alternating current (AC) supplied from the transformer to DC to power the amplifier modules. The transformer is a 500 VA toroidal transformer, RS0500P1-2-045K (Talema Elektronik, Germering, Germany), with a single 230 V primary winding and dual 45 V secondary windings. Three class-AB amplifier modules, NXL200 R4 (Holton Precision Audio, Launceston, Australia), are used separately to supply each transmit channel. With 63 V rail voltage, each amplifier module can supply root means square (RMS) 150 W to 8 Ω load or 260 W to 4 Ω load, and the minimum required load impedance is 2 Ω. Refer to [58] for more specifications of the amplifier module. The heat sinks to dissipate the heat from the metal-oxide-semiconductor field-effect transistor (MOSFET) chips, and a temperature sensor is attached to monitor the temperature. Different heat sinks are installed, while the one outside of the chassis is cooled by fans. A DC power supply, MW 3H36GS (Minwa Electronics, Hong Kong, China), is used separately to power the fans. Two light emitting diode (LED) indicators indicate the rail voltage applied on the amplifier modules, which can be seen from the front panel. The input signal connectors are bayonet Neill–Concelman (BNC) connectors, and the output connectors are XLR connectors.

The amplifier modules used here are designed for audio amplification. The audio frequencies range from about 20 Hz to 20 kHz, which is a bit lower than the typical operating frequency (25 kHz) in the MPI application. However, it is not difficult to find a commercially available audio amplifier with a

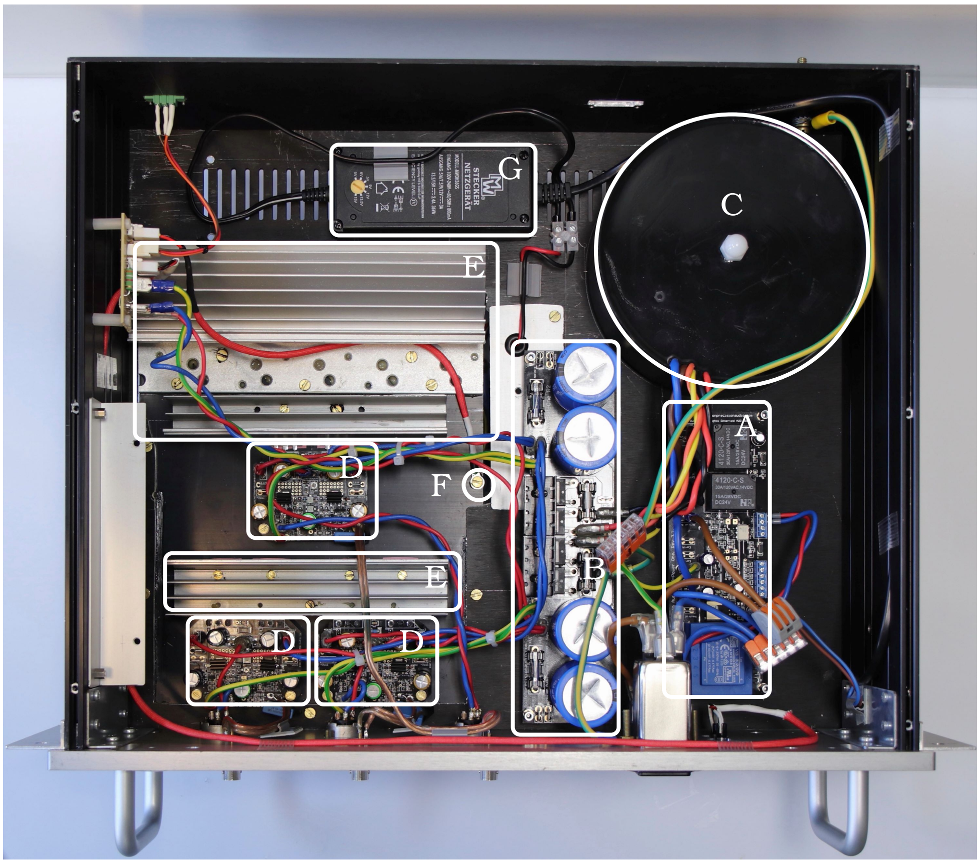

(a) Top view

Figure 3.18: Views of the power amplifier. Top view (a), front view (b), and bottom view (c) show the power amplifier from different directions. The solid frames indicate different components in the power amplifier: A: mains power controller; B: power supply unit; C: toroidal transformer; D: amplifier modules; E: heat sinks; F: temperature sensor; G: DC power supply; H: heat sink with fans; I: inputs and outputs; J: LED indicators; K: switches. Note the top panel of the chassis is disassembled for a better demonstration, and the scale is not in proportion.

(b) (cont.) Front view

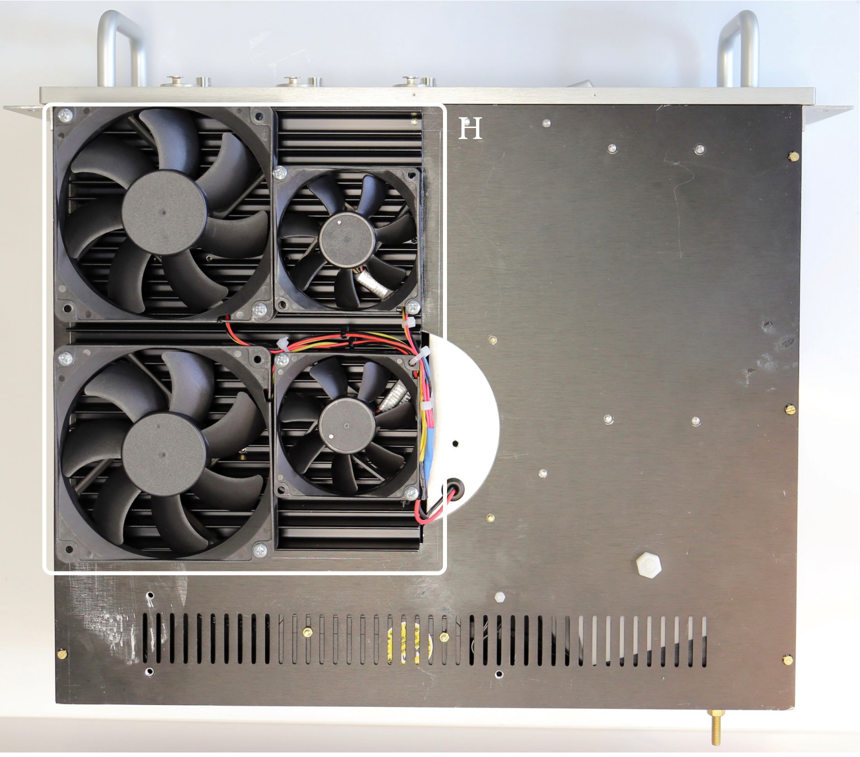

(c) (cont.) Bottom view

Figure 3.18 (cont.): Views of the power amplifier (continued).

bandwidth greater than 25 kHz. The amplifier modules used here have a frequency response from 3.5 Hz to 300 kHz. Since the transmit signal in each channel is at a single frequency, the purity of the signal is essential, i.e., the signal applied on the transmit coils should ideally have minimal distortion. A linear power amplifier should be used in favor of its better linearity over the switching amplifier. A class-AB amplifier is recommended among different linear amplifiers due to its better linearity than the class-B amplifier and higher efficiency than the class-A amplifier. Most of the commercially available audio amplifiers supply speakers with rated impedance between 4 Ω and 8 Ω. Therefore, depending on the desired power, the input impedance of each transmit channel should be matched to an impedance between 4 Ω and 8 Ω. Note that the lower the load impedance, the more power it can draw from the amplifier, but the heat dissipation will limit the performance of the amplifier. Instead of a self-built power amplifier, a suitable audio amplifier with a built-in linear power supply can also be acquired and used in the MPS system.

3.3 Impedance Matching

The term "impedance matching" in an electrical system with transmission lines means that the impedance at the end of the line is matched to the characteristic impedance of the transmission line to avoid reflection. In an MPS, the length of the cable is not long enough to be considered a transmission line. More often, "impedance matching" defines the process of matching the impedance of the load to the impedance of the source. According to the maximum power transfer theorem, it results in a maximum power transfer from the source to the load. However, in modern audio amplifiers, active components are used, and the effective output impedance may be very low (typically $< 0.1\,\Omega$). The active circuitry dynamically controls the power delivered to the load. Impedance matching of the load to the amplifier is no longer considered best practice. Therefore, the "impedance matching" used here is for its broad meaning of adjusting mismatched impedance. The impedance of the load is matched to a target impedance so that sufficient power can be delivered to the load from the amplifier.

3.3.1 Matching Network

A two-element matching network, L network, is a basic and widely used network architecture. A combination of a capacitor(s) and an inductor(s) can be chosen to match the impedance. Fig. 3.19 shows a basic schematic of an impedance matching network. Consider a real source impedance of R_0 and a real load impedance of R_L, and $R_0 > R_\mathrm{L}$. The impedance of R_L and the series component can be written as

$$Z = R_\mathrm{L} + jX_\mathrm{S} \,, \tag{3.21}$$

and its admittance is

$$Y = \frac{R_\mathrm{L}}{{R_\mathrm{L}}^2 + {X_\mathrm{S}}^2} - \frac{jX_\mathrm{S}}{{R_\mathrm{L}}^2 + {X_\mathrm{S}}^2} \,. \tag{3.22}$$

In order to match R_L to R_0, the impedance Z_in seen from the input of the impedance network should equal to R_0. Therefore, the imaginary part of Y should be canceled by the susceptance of the parallel component, and the real part should equal the source conductance, which gives

$$\Re\{Y\} = \frac{1}{R_0} \,, \tag{3.23}$$

$$\Im\{Y\} + \frac{1}{jX_\mathrm{P}} = 0 \,. \tag{3.24}$$

Substituting Eq.(3.22) into Eq. (3.23) and Eq. (3.24), one gets

$$|X_\mathrm{P}| = \frac{R_0}{Q_0} \,, \tag{3.25}$$

$$|X_\mathrm{S}| = Q_0 R_\mathrm{L} \,, \tag{3.26}$$

$$\text{where} \quad Q_0 = \sqrt{\frac{R_0}{R_\mathrm{L}} - 1} \tag{3.27}$$

is the quality factor of the impedance matching network. X_P and X_S are the reactance of the parallel and series components, respectively, of which one must be an inductor and the other must be a capacitor [59].

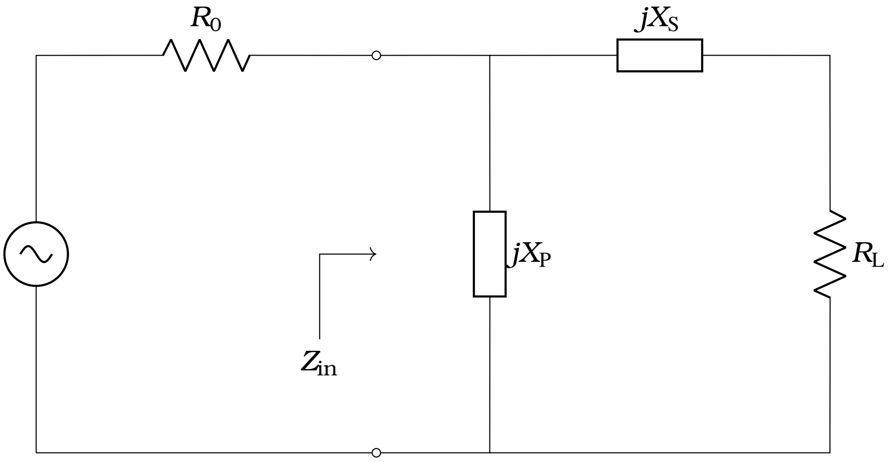

Figure 3.19: Basic schematic of an impedance matching network. R_0 is the source resistance, R_L is the load resistance. X_P and X_S are the reactance of the parallel and series components, respectively. Note that in this schematic $R_0 > R_L$.

In this study, R_0 was considered as a virtual target resistance to which the load impedance was matched. The parallel component was chosen as a capacitor to form a low-pass configuration, which gave the matching network additional features of attenuating the harmonics and noise of higher frequencies. The series component was supposed to be an inductor. However, due to the inductive component of the transmit coil, the serial component was actually a capacitor to compensate for the inductive reactance.

As mentioned in Section 2.3.3, a cancellation unit should be built identically to the generation unit. See Fig. 3.20, the transmit coils in both units are connected in the same circuit and are assumed to be equal. A capacitor C_b is used to form a resonance circuit with the transmit coil in the cancellation unit. The resonance frequency is written as [60]

$$\omega_0 = \omega_0' \sqrt{1 - \frac{1}{Q^2}}\,, \tag{3.28}$$

where

$$\omega_0' = \frac{1}{\sqrt{LC_b}}\,,$$

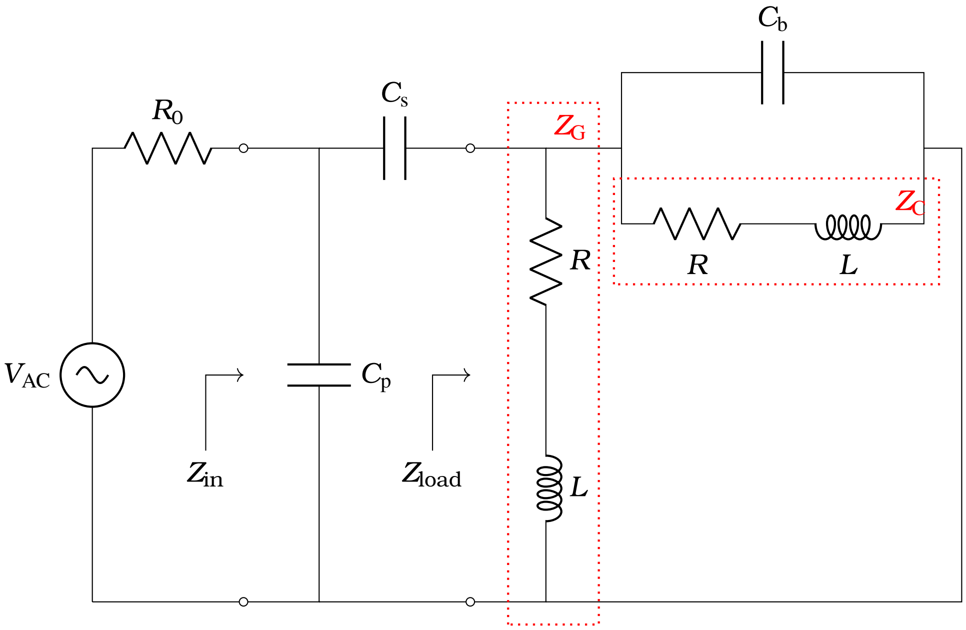

Figure 3.20: Schematic of the impedance matching network in the transmit chain. R_0 is considered as a virtual source resistance to which the load impedance is matched. C_s and C_p are the series and parallel capacitors, which form the matching network. C_b forms a resonant circuit with the transmit coil in the cancellation unit. Z_G and Z_C are the impedance of the transmit coils in the generation and cancellation units, respectively, which are assumed to be equal. Note that the schematic shows the impedance matching network in only one transmit channel.

$$Q = \frac{1}{R}\sqrt{\frac{L}{C_b}}\,.$$

When the quality factor $Q \gg 1$, the resonance frequency $\omega_0 \approx \omega_0'$, then

$$C_b = \frac{1}{{\omega_0}^2 L}\,. \tag{3.29}$$

The impedance of the resonance circuit is given as

$$Z_B = \frac{(R + j\omega_0 L)\dfrac{1}{j\omega_0 C_b}}{R + j\omega_0 L + \dfrac{1}{j\omega_0 C_b}} = \frac{{\omega_0}^2 L^2}{R} - j\omega_0 L\,, \tag{3.30}$$

Therefore, the load impedance is

$$Z_{\text{load}} = \frac{Z_B Z_G}{Z_B + Z_G}$$

$$= \frac{\left(\frac{\omega_0{}^2 L^2}{R} - j\omega_0 L\right)(R + j\omega_0 L)}{\frac{\omega_0{}^2 L^2}{R} - j\omega_0 L + R + j\omega_0 L}$$

$$= \frac{2R}{1 + \frac{R^2}{\omega_0{}^2 L^2}} + j\omega_0 L \frac{1 - \frac{R^2}{\omega_0{}^2 L^2}}{1 + \frac{R^2}{\omega_0{}^2 L^2}}$$

$$= \frac{2R}{1 + \frac{1}{Q^2}} + j\omega_0 L \frac{1 - \frac{1}{Q^2}}{1 + \frac{1}{Q^2}}\,, \tag{3.31}$$

when $Q \gg 1$,

$$Z_{\text{load}} \approx 2R + j\omega_0 L\,. \tag{3.32}$$

The load impedance approximately equals the impedance of one transmit coil but with its resistance doubled. Substituting the load resistance of Eq. (3.32) into Eq. (3.27) gives

$$Q_0 = \sqrt{\frac{R_0}{2R} - 1}\,. \tag{3.33}$$

Since the parallel component is a capacitor, from Eq. (3.25) one gets

$$X_P = -\frac{R_0}{Q_0}\,, \tag{3.34}$$

$$C_p = \frac{Q_0}{\omega_0 R_0}\,. \tag{3.35}$$

The negative sign means that the component is a capacitor. The series component is a capacitor that compensates for the inductive reactance of the load. Substituting Eq. (3.33) into Eq. (3.26) and subtracting the reactance of Eq. (3.32), one gets

$$X_S = 2RQ_0 - \omega_0 L \,, \tag{3.36}$$

$$C_s = \frac{1}{\omega_0(\omega_0 L - 2RQ_0)} \,. \tag{3.37}$$

3.3.2 Network Construction

Calculation

The target impedance, to which the matching network was matched, was chosen to be 4 Ω. The impedance of each channel was matched at specific frequencies, which were 24.51 kHz, 26.04 kHz, and 25.25 kHz, as mentioned in Section 2.3.1. With the values of the transmit coils in Table 3.2, the capacitors needed for constructing the impedance network were calculated from Eq. (3.29), Eq. (3.35), and Eq. (3.37). Note that the values of each coil or pair of coils were averaged for an approximate calculation. The calculated values of the capacitors are shown in Table 3.3. The transmit chains in x-, y-, and z- channel are denoted by T_x-, T_y-, and T_z-channel, respectively, according to the denotations of the transmit coils.

Table 3.3: Capacitor values in the matching network

Channel	Frequency [kHz]	C_s [μF]	C_p [μF]	C_b [μF]
T_x	24.51	0.979	9.247	0.888
T_y	26.04	0.112	4.151	0.109
T_z	25.25	0.075	3.517	0.074

As mentioned in Section 3.1.6, the currents applied in T_x-coil, T_y-coils, and T_z-coils to generate $20\,\mathrm{mT}/\mu_0$ magnetic field were 15.5 A, 13.0 A, and 15.5 A, respectively. Although these were DC values, they were used as magnitude values of the AC to calculate the corresponding voltages and currents on the capacitors in the matching network. The RMS values of the voltages and currents of the capacitors are shown in Table 3.4. Note that the resonance circuit was assumed to be ideal.

Table 3.4: RMS values of voltage and current applied on the capacitors in the matching network

Channel	C_s		C_p		C_b	
	U [V]	I [A]	U [V]	I [A]	U [V]	I [A]
T_x	72.7	11.0	7.6	10.8	80.2	11.0
T_y	502.0	9.2	12.7	8.6	514.0	9.2
T_z	917.7	11.0	17.9	10.0	934.0	11.0

Selection

The values in Table 3.3 and Table 3.4 were essential for selecting the proper capacitors. Since the commercially available capacitors could only have certain capacitance values, each required capacitor was actually a combination of multiple different capacitors. The capacitors were combined in series and/or in parallel so that the voltages and currents applied to them were divided into a safe operating range. The capacitors used in this study were polypropylene film capacitors (series A72, C4C, and C4G) from KEMET (Fort Lauderdale, United States), which have a low dissipation factor and could be used for high-frequency and high-power applications. An example is given in Fig. 3.21 to show a capacitor combination of C_b in T_z-channel. The required capacitance read from Table 3.3 is 0.074 µF, and the combination approaches with capacitance 0.073 µF. The voltage and current applied to each capacitor are calculated in accordance with the values from Table 3.4. Refer to the manuals [61–63], the 68 nF capacitor of rated AC voltage 750 V and ripple current 9 A, and 10 nF capacitor of rated AC voltage 750 V and ripple current 3 A from series C4C are selected. The combined capacitors should reach a capacitance close to, but smaller than, the required capacitance. The capacitor value could be adjusted late in the tuning step. The selection procedure should be carefully conducted for all required capacitors.

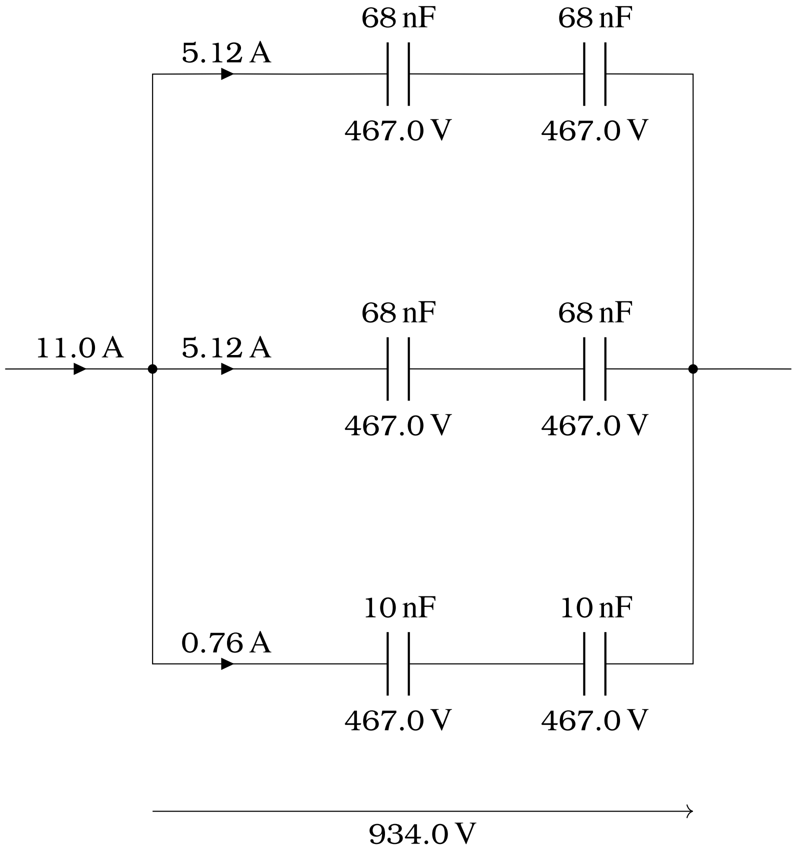

Figure 3.21: Schematic of the capacitor combination of C_b in T_z-channel. The required capacitance is 0.074 µF, the combination approaches with capacitance 0.073 µF. The capacitors are combined in series and in parallel to divide the voltages and currents applied to them.

Tuning

Due to the tolerance of the capacitors, their capacitance may vary from the nominal values. During the calculation of the capacitor values in Table 3.3, a few assumptions were made. Besides, the internal resistance of the capacitors was not taken into consideration. Therefore, tuning was indispensable for precise impedance matching. An impedance analyzer, E4990A (Keysight Technologies, California, United States), was used in the tuning procedure. Tuning was done by manually adding or removing capacitors of smaller values. Additionally, because the capacitors used here had 5 % tolerance, the capacitors were swapped with the same nominal values for finer tuning. Note that the impedance results were measured at the frequencies shown in Table 3.3. The tuning was done separately for each of the three transmit channels. The voltage and current applied to the added capacitors were calculated to select the proper ones.

Tuning C_b First, C_b was connected in parallel with the transmit coils in the cancellation channel. Then, the probes of the impedance analyzer were connected with the terminals of the transmit coils to measure the magnitude $|Z|$ and the phase angle θ of the impedance Z_B (see Fig. 3.20). Since C_b and the transmit coils together formed a resonance circuit, C_b was precisely tuned to let phase angle θ approach to 0°. The measured results of Z_B are shown in Table 3.5.

Table 3.5: Measured results of Z_B after tuning C_b

Channel	$\|Z\|$ [kΩ]	θ [deg]
T_x	0.85	−0.15
T_y	12.04	−0.20
T_z	19.65	−1.61

Tuning C_s Secondly, the resonance circuit was connected in parallel with the transmit coils in the generation unit and then together connected in series with C_s. The impedance analyzer was used to measure the conductance G and susceptance B at the input terminals of the circuit. C_s was tuned to let G approach the reciprocal of the target resistance (see Eq. (3.23)). Although the target impedance was chosen to be $4\,\Omega$, the power amplifier could actually safely deliver power to a load impedance above $2\,\Omega$. It was thus unnecessary to precisely tune C_s. So C_s was tuned so that G is close to 0.25. The measured results of the admittance at the input terminals of the circuit are shown in Table 3.6.

Table 3.6: Measured admittance after tuning C_s

Channel	G [Ω]	B [Ω]
T_x	0.22	1.32
T_y	0.23	0.62
T_z	0.24	0.53

Tuning C_p Lastly, C_p was connected to the circuit. The impedance analyzer was connected to measure the magnitude $|Z|$ and the phase angle θ of the impedance Z_in (see Fig. 3.20). According to Eq. (3.24), C_p was precisely tuned to let θ approach 0°. The measured results of Z_in are shown in Table 3.7.

Table 3.7: Measured results of Z_in after tuning C_p

Channel	$\lvert Z\rvert$ [Ω]	θ [deg]
T_x	4.24	0.89
T_y	4.40	0.02
T_z	4.21	1.59

Installation

The capacitors were soldered on the copper plates for a stable connection. The capacitors in each transmit channel are installed in separate chassis. Fig. 3.22 shows the installed capacitors in one of the chassis.

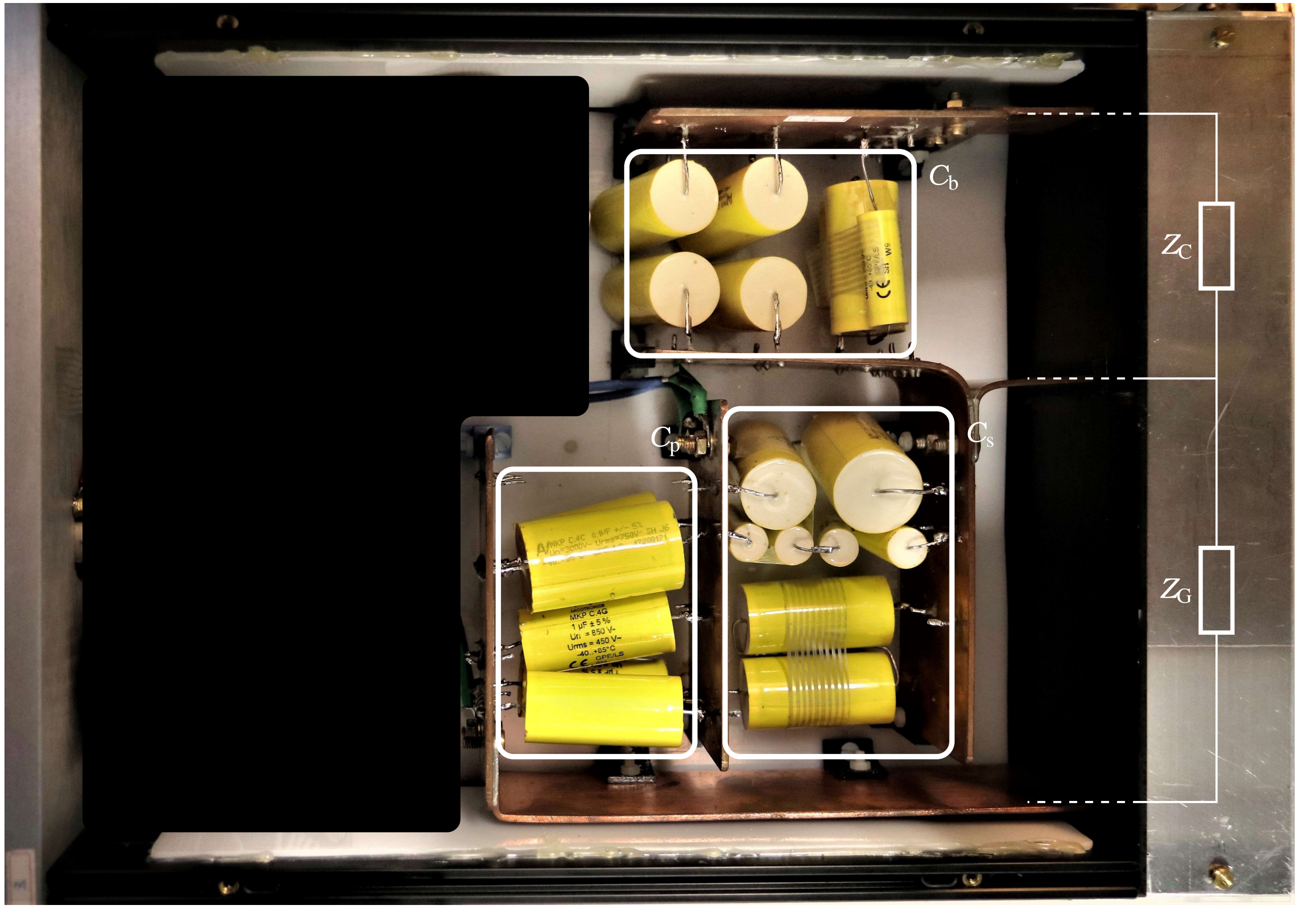
[redacted]

Figure 3.22: Installed capacitors of the impedance matching network. The installed capacitor combinations are indicated by the solid frames. The transmit coils in generation and cancellation units are illustrated by Z_G and Z_C, respectively. Note that the capacitors in each transmit channel are installed in separate chassis.

3.3.3 Discussion

During the tuning procedure, the capacitors had been soldered and desoldered multiple times to adjust the capacitance. It was time-consuming and inconvenient to do so. In addition, the capacitance of the capacitors may drift over time. In order to adjust the drifted capacitance, the chassis needs to be dismantled, and the tuning procedure needs to be conducted from the first step. For a more convenient and easier tuning process, variable capacitors could be used. However, most variable capacitors have very small capacitance values, typically in the range of pF. Combining the fixed capacitors and the variable capacitors may be a solution to overcome the limitation. For instance, refer to Fig. 3.21, a variable capacitor is connected in series with the 10 nF capacitors, which is plotted in Fig. 3.23. The fine-tuning of the capacitance is then done by adjusting the variable capacitors. Since the variable capacitors could be mounted on the chassis panel, adjusting the drifted capacitance will be efficiently conducted without dismantling the chassis. The installation of the variable capacitors could be a future improvement of the hardware.

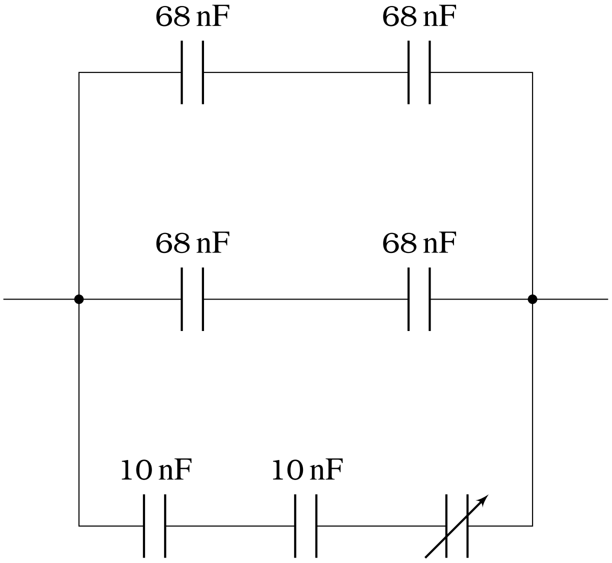

Figure 3.23: Schematic of the capacitor combination with a variable capacitor. The variable capacitor can be easily tuned to adjust the capacitance of the combined capacitors.

3.4 Band-Pass Filter

All amplifiers possess the impairment of linearity in the signals they amplify. Besides, a class-AB amplifier was used to improve the efficiency, which, on the other hand, degraded the linearity. Although the bias level was carefully adjusted, the crossover distortion could not be fully removed. The existence of distortion and, hence, non-linearity in the transmit signals is very displeasing since the harmonic of the receive signals are essential characteristics of the nanoparticles. Therefore, filtering should be employed to reduce the distortion of the amplified signals.

3.4.1 Design and Simulation

Third-order LC BPFs were used to reduce the harmonic distortion from the power amplifier. Fig. 3.24 shows the schematic of the BPF together with the impedance matching network and the transmit coils in the transmit chain.

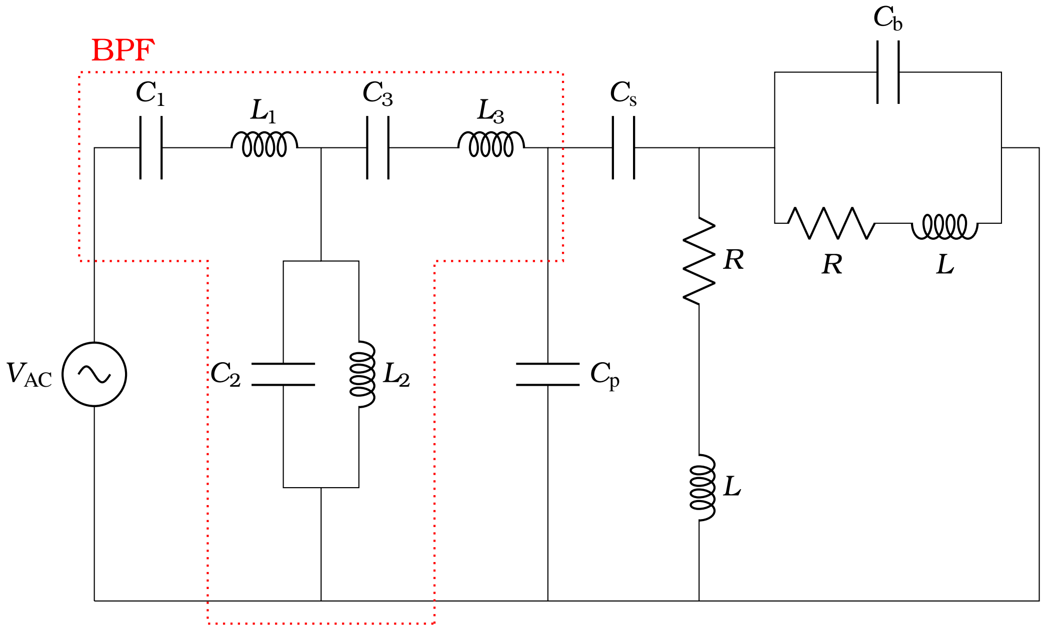

Figure 3.24: Schematic of the BPF in the transmit chain. It is a third-order LC filter. Note that the schematic shows the BPF in only one transmit channel.

At first, the filter was designed with the assumption of a resistive load by using the FilterSolutions (Ansys, Pennsylvania, United States). Afterward, with the transmit coil values (see Table 3.2) and the capacitor values in the impedance matching network (see Table 3.3), the circuits shown in Fig. 3.24 were simulated in the LTspice. Due to the more realistic load values, the indicators and capacitors in the BPF were adjusted to achieve a better attenuation at all drive field frequencies (24.51 kHz, 26.04 kHz, and 25.25 kHz). Later, in the operating software of the MPS, a decoupling function was implemented to reduce the coupling effects between the transmit coils in different channels. For instance, in T_x-channel, the transmit signals applied from the PC not only contain the 24.51 kHz signal but also contain the 26.04 kHz and 25.25 kHz signals with reversed phase to cancel out the coupled signal from T_y- and T_z-channels. The capacitor values were chosen according to the commercially available capacitors [61–63]. The adjusted values of the LC components in the BPFs are shown in Table 3.8. The simulated attenuation results of the BPFs at different harmonics are shown in Table 3.9. Note that the results are normalized to the ones at the fundamental frequencies in each channel.

Table 3.8: Values of the LC components in the BPFs

Channel	C_1 [µF]	L_1 [µH]	C_2 [µF]	L_2 [µH]	C_3 [µF]	L_3 [µH]
T_x	1.0	42.2	5.0	8.4	1.0	42.2
T_y	1.0	37.4	4.4	8.5	1.0	37.4
T_z	0.68	58.4	6.2	6.4	1.0	39.7

Table 3.9: Simulated attenuation results of the BPFs

Channel	2nd [dB]	3rd [dB]	4th [dB]
T_x	−46.8	−66.9	−78.6
T_y	−37.9	−58.3	−70.1
T_z	−40.8	−61.1	−72.8

3.4.2 Construction

The LC branches in the BPF needed to be precisely tuned to the resonant frequencies. Otherwise, the simulated attenuation would not be achieved. Although, it was possible to tune either the capacitors, the inductors, or even both. For simplicity, in this study, the capacitors were chosen from the commercially available capacitors, and the inductors were self-built tunable inductors. The selection of the capacitors was similar to that mentioned in Section 3.3.2, except that the selected capacitor(s) should have the required values as in Table 3.8. The self-built inductors were air core inductors so that the saturation and the production of harmonics could be prevented.

The tunable inductor is shown in Fig. 3.25, the wires are wound on the coil former (a) to form a toroidal shape of coil (b) with a rectangular cross-section. Half of the coil is fixed on the base, while the other half is movable. With the change of the angle between the two halves of the coil, the inductance can be fine-adjusted. The coil former and the base parts were printed with the PLA material by the Ultimaker 3 (Ultimaker, Utrecht, Netherlands). The inductance of the toroidal coil was approximately calculated according to the formulas in [64]. However, the cross-section of the toroid was not optimized to achieve the maximum inductance. The dimensions of the coil former were designed mainly with consideration of the space limitation inside the chassis. Due to the big difference of the inductance between L_1 (L_3) and L_2 (see Table 3.8), the dimensions of the coil former used for L_1 (L_3) and L_2 were different. The Litz wires used to wind the coils were also different because of the current limitation of the wires. The self-built inductors had a quality factor of about 30–35 at 25 kHz. The impedance analyzer, E4990A (Keysight Technologies, California, United States), was used during the tuning. The inductors were adjusted to let the phase value of the impedance of each resonant branch in the BPF approach to 0°. The installed BPF is shown in Fig 3.26.

3.4.3 Results

After connecting the BPF to the transmit chain, a waveform generator, DG1032Z (RIGOL Technologies, Beijing, China), was used to send excitation

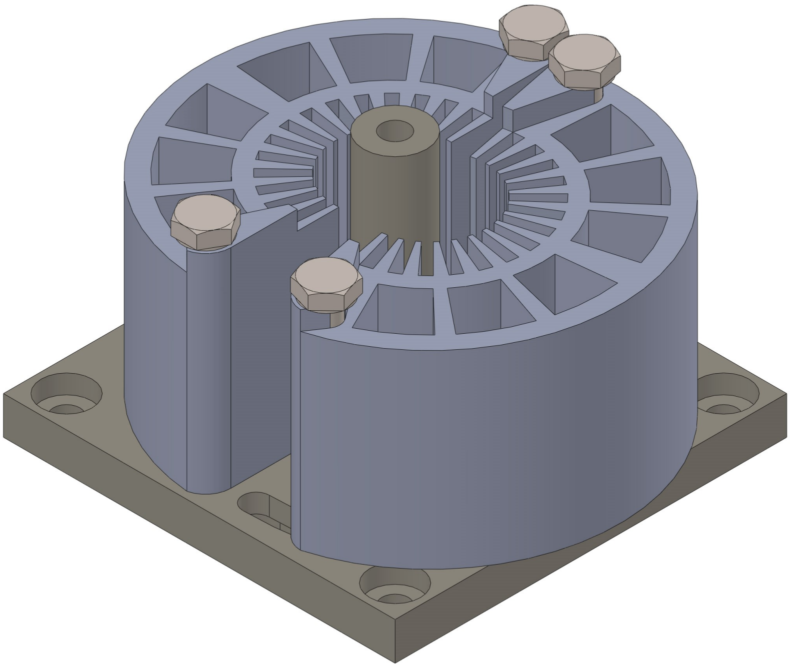

(a) CAD model of the coil former

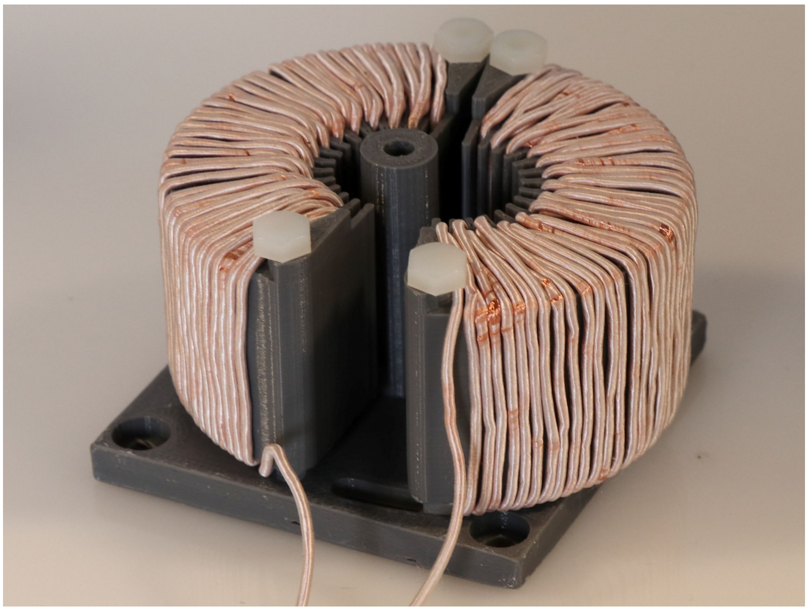

(b) Self-built tunable inductor

Figure 3.25: Tunable air core inductor in the BPF. The wires are wound on the coil former (a) to form a toroidal shape of coil (b) with a rectangular cross-section. The angle between the two halves of the coil can be changed to fine adjust the inductance.

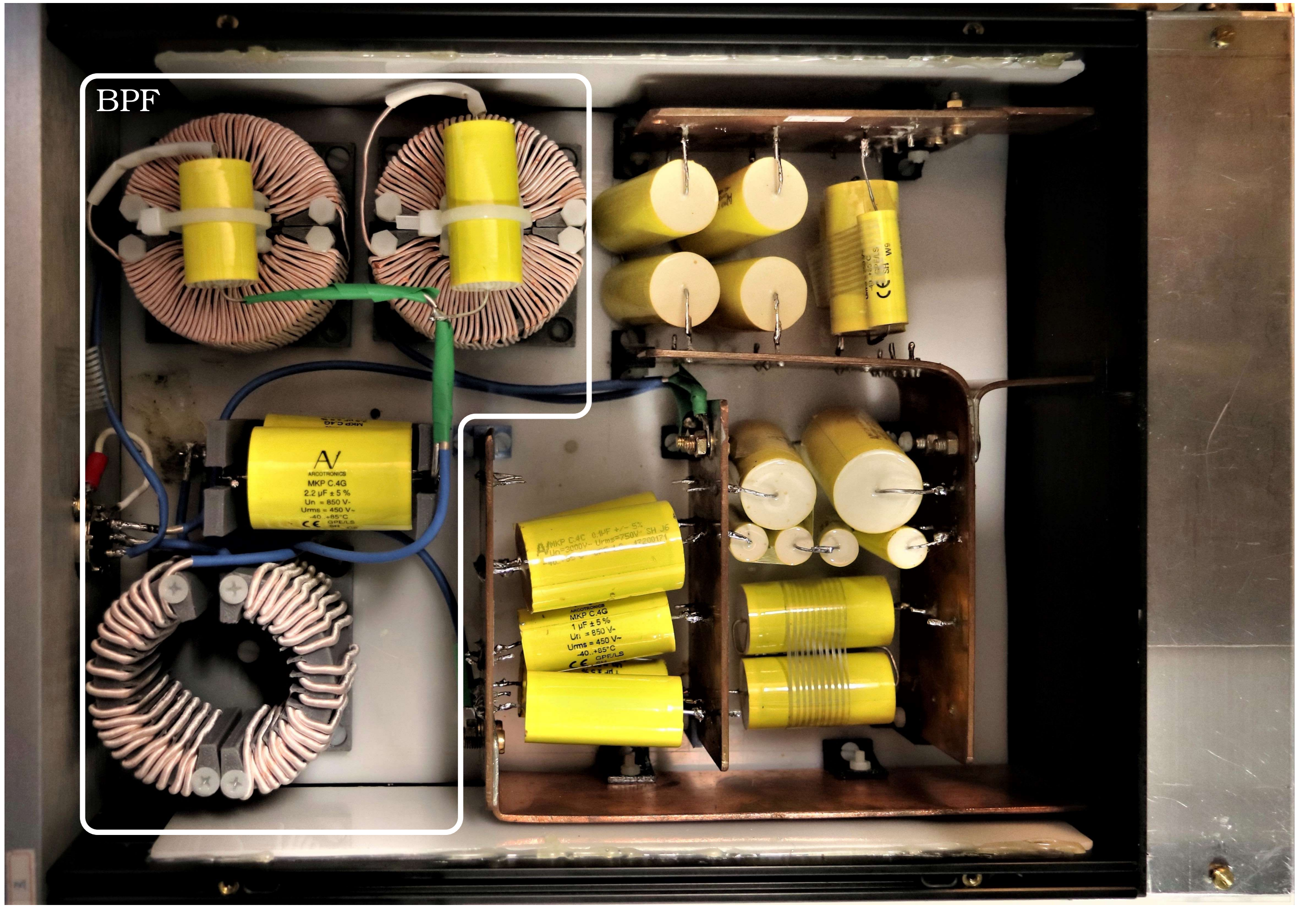

Figure 3.26: Installed BPF in the chassis. The solid frame indicates the three-order LC BPF. Note that the installed BPF in only one transmit channel is shown.

signals at each harmonic frequency to the power amplifier. The voltage signals at the input and the output of the BPF were measured by an oscilloscope, HDO6104-MS (Teledyne LeCroy, New York, United States), and then the attenuation values were calculated. The results are shown in Table 3.10. Note that the attenuation results are normalized to the ones at the fundamental frequencies in each channel. Compared to the simulation values (see Table 3.9), the measured values show good compliance.

Table 3.10: Measured attenuation results of the BPFs

Channel	2nd [dB]	3rd [dB]	4th [dB]
T_x	−46.5	−65.6	−73.9
T_y	−38.2	−61.3	−79.8
T_z	−41.1	−63.3	−78.1

3.4.4 Discussion

During the simulation of the BPF, the input impedance of the entire transmit chain was also checked. See the specifications of the amplifier mentioned in Section 3.2, the minimum required load impedance is $2\,\Omega$. As shown in Fig. 3.27, near the excitation signal frequency at the T_x-channel, the safe impedance range is only about 300 Hz. Extra caution is required when applying signals to the transmit channels. It can be solved by just adding an extra resistor, but it will consume more power. Another possible way is to use different impedance matching methods. For instance, instead of using an L network, a T or Pi network could be used. The advantage is that the quality factor of the matching network can then be adjusted. With the adopted BPF, the safe input impedance range is possible to be improved. However, this improvement has not been made in this work.

3.5 DC Source and H-Bridge

In order to generate the static offset fields, DC sources were used to apply the DC on the transmit coils. The DC sources SM7.5-80 and SM18-50 (Delta Elektronika, Zierikzee, Netherlands) were used in this study. The

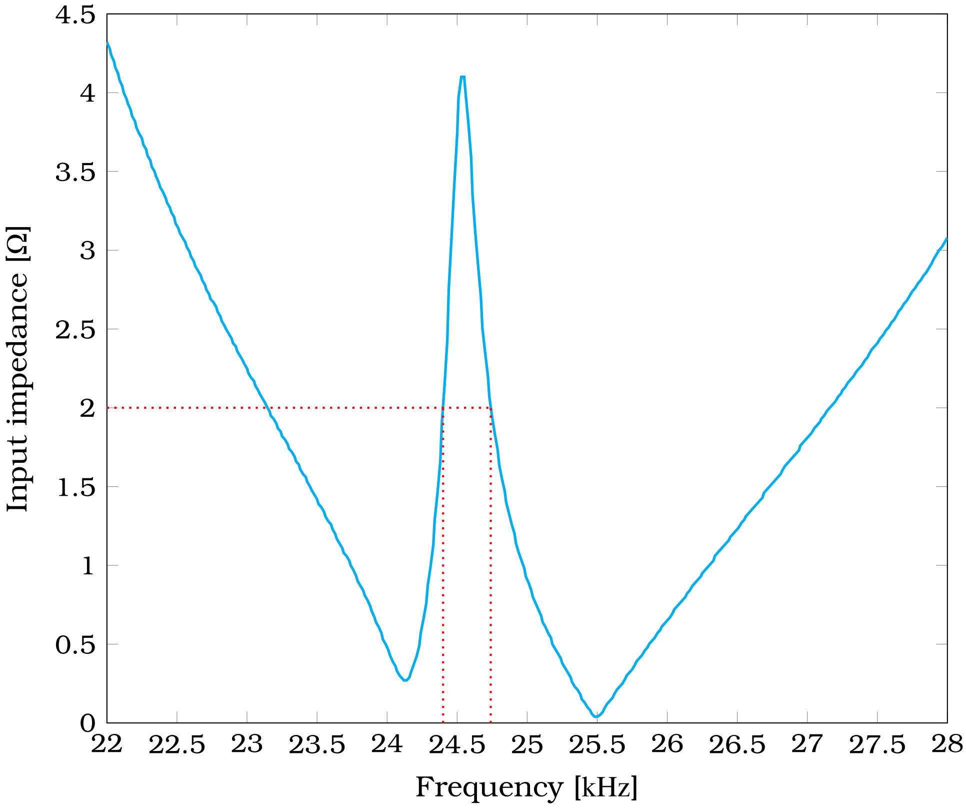

Figure 3.27: Simulated input impedance of the T_x-channel. Near the excitation signal frequency 24.51 kHz, the safe impedance range of over 2 Ω is only about 300 Hz.

SM7.5-80, which could supply a maximum voltage of 7.5 V and current of 80 A, were used in T_x- and T_y-channel, while the SM18-50 with a maximum voltage of 18 V and current of 50 A was used in T_z-channel. For detailed specifications, refer to [65]. There are two methods to control the output voltage and current. One is digital programming, which sends the standard commands for programmable instruments (SCPI) from the PC to the DC source via the RS-232 port. The other method is analog programming, which uses an external analog voltage in the range of 0–5 V via the 15-pin data bus (DB) connector. For fast programming speed, analog programming was usually used in this study. Note that "switch 1-1" needs to change the position when switching between digital and analog programming.

To change the polarity of the offset fields, the direction of currents applied to the coils needed to be switched. Since the DC sources used here were not bipolar, external hardware was implemented to switch the direction of the current. The devices used for this purpose are H-bridges, UMS00100.80T (Camtec Power Supplies, Pfinztal, Germany), which has a rated voltage of 30 V and rated current of 80 A [66]. Each H-bridge was controlled via the 15-pin DB interface. Note that the control voltage level was 24 V. Fig. 3.28 shows where the DC source and the H-bridge are connected in the transmit chain.

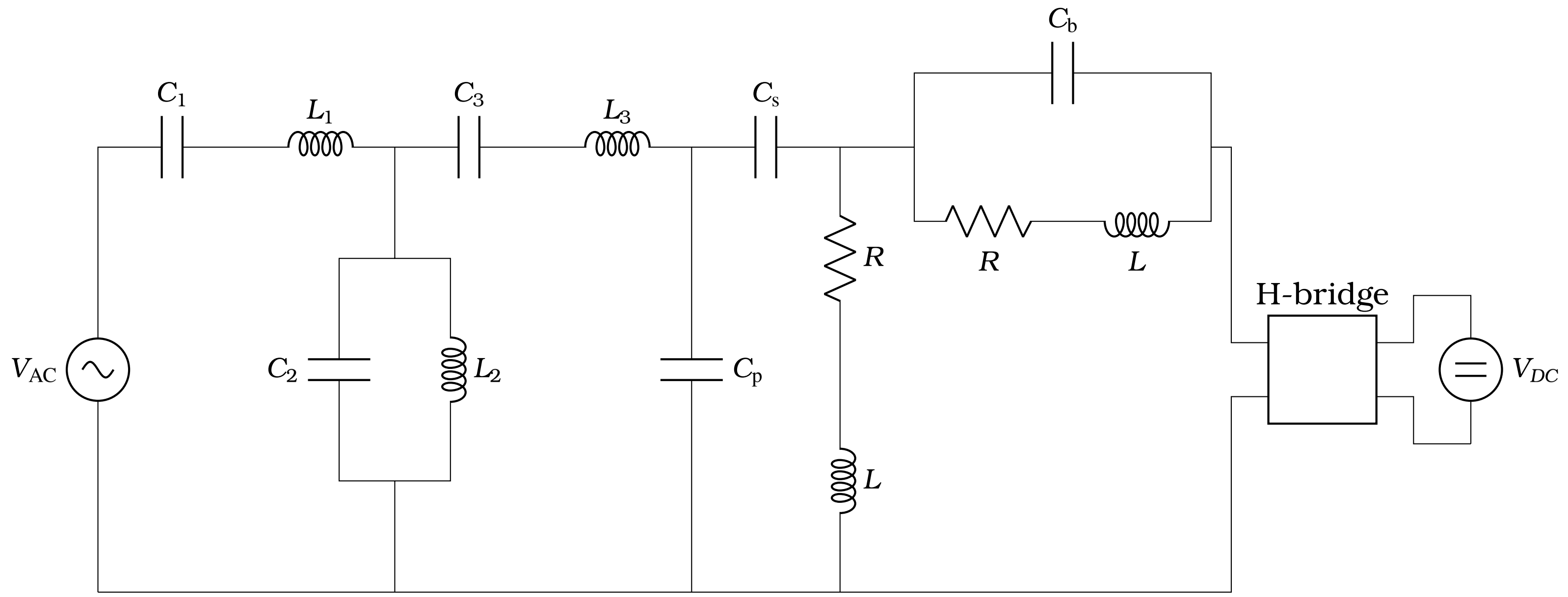

Figure 3.28: Schematic of the transmit chain. The block denotes the H-bridge, V_{DC} denotes the DC source, and V_{AC} denotes the power amplifier. Note that the schematic shows the transmit chain in only one channel.

CHAPTER 4

RECEIVE CHAIN

4.1 Receive Coils

4.1.1 Design Considerations

The changing magnetization of the MNPs induces a voltage signal in the receive coil. As mentioned in Section 2.3.3, two receive coils were built identically and connected in series with inverse polarity. Using the gradiometer coils as the receive coils could reduce the coupled excitation signals [67]. However, in a multidimensional MPS, designing the gradiometer coils for all receive channels is challenging, especially considering the limited space in the central bore. Therefore, the gradiometer coils were not considered in this study.

In general, the goal of the receive coil design is to achieve a high SNR, which in principle can be done by increasing the amplitude of the receive signals and/or reducing the amplitude of the noise signal. The induced voltage in a receive coil can be described by Eq. (2.8). Increasing the sensitivity of the receive coil, namely increasing the field generated by the coil per unit current (see Eq. (2.9)), results in an increase in the received signal. According to the Biot-Savart law (see Eq. (3.2)), a coil with a closer distance to the FoV and a larger number of windings can generate a higher magnetic field with a unit current, i.e., higher sensitivity. However, coils with a larger number of windings will have higher resistance, which results in higher intrinsic noise. The intrinsic thermal noise is given as

$$U_\mathrm{n} = \sqrt{4k_\mathrm{B}T\Delta fR}, \tag{4.1}$$

where k_B is the Boltzmann constant, T is the absolute temperature, R is the resistance of receive coil, and Δf is the sampling bandwidth.

From the previous study (see the setup in [25]), the receive coils had very low resistance, which was in the range of 100–200 mΩ. Therefore, their noise voltage was less than $60\,\mathrm{pV}/\sqrt{Hz}$ at room temperature. When comparing the noise voltage of the LNA [68], which was in a range of few $\mathrm{nV}/\sqrt{Hz}$, the receive coils were not the dominant noise source in the receive chain. Thus, the receive coils in this study were aimed to achieve high sensitivity.

4.1.2 Design and Construction

Inside the transmit T_x-coil, a cylindrical volume with 13 mm radius was reserved for fitting the receive coils and the water pipe of the temperature control unit (see Section 5.3). To achieve high sensitivity, the receive coils were placed as close to the sample vial as possible, while the water pipes were placed outside the receive coils. Thus, between the sample vial and the water pipes, a cylindrical volume with 4 mm inner radius and 8.5 mm outer radius was left for constructing the receive coils. The shapes of the receive coils were similar to those in [25]. The receive coil in the x-axis direction (named R_x-coil in the following) was a circular solenoid, the receive coils in perpendicular y- and z-axis directions were two Helmholtz-like pairs of curved rectangular coils (named respectively R_y-coils and R_z-coils in the following).

In order to have more windings in the coils, a thin Litz wire (Elektrisola, Reichshof-Eckenhagen, Germany) was used to build the coil, which has 500×0.02 mm strands, 0.6 mm diameter, and 114.4 mΩ/m resistance. Due to the space limitation, it was challenging to build the receive coils the same way as building the transmit coils. Instead of using the coil mold and the adhesive to form the shapes of the coil, the receive coils were wound directly on the coil formers. As seen in Fig. 4.1, the coil formers for the receives coils are three concentric cylindrical shells with 1.5 mm wall thickness. The number of windings was maximized to achieve maximal coil sensitivity. The maximum winding numbers of R_y-coils and R_z-coils were limited by the radius of the cylindrical shell, while for R_x-coil the winding number was decided in consideration of the mechanical structure of the former. The designed R_x-coil had 4.8 mm inner radius and 25 number of windings; the R_y-coils had 6.3 mm curvature radius and 10 number of windings; the R_z-coils had 7.8 mm curvature radius and 13 number of windings. See Fig. 4.1, the grooves on the formers of the R_y-coils and R_z-coils have very thin walls, which has a thickness of 0.3 mm. This value is experiential, depending on the material used to manufacture the coil formers and the manufacturing methods. In this study, a 3D printer, Form 2 (Formlabs, Massachusetts, United States), was used to print the coil formers. The printing material was the standard clear resin (FLGPCL04) [69]. The built coils are shown in

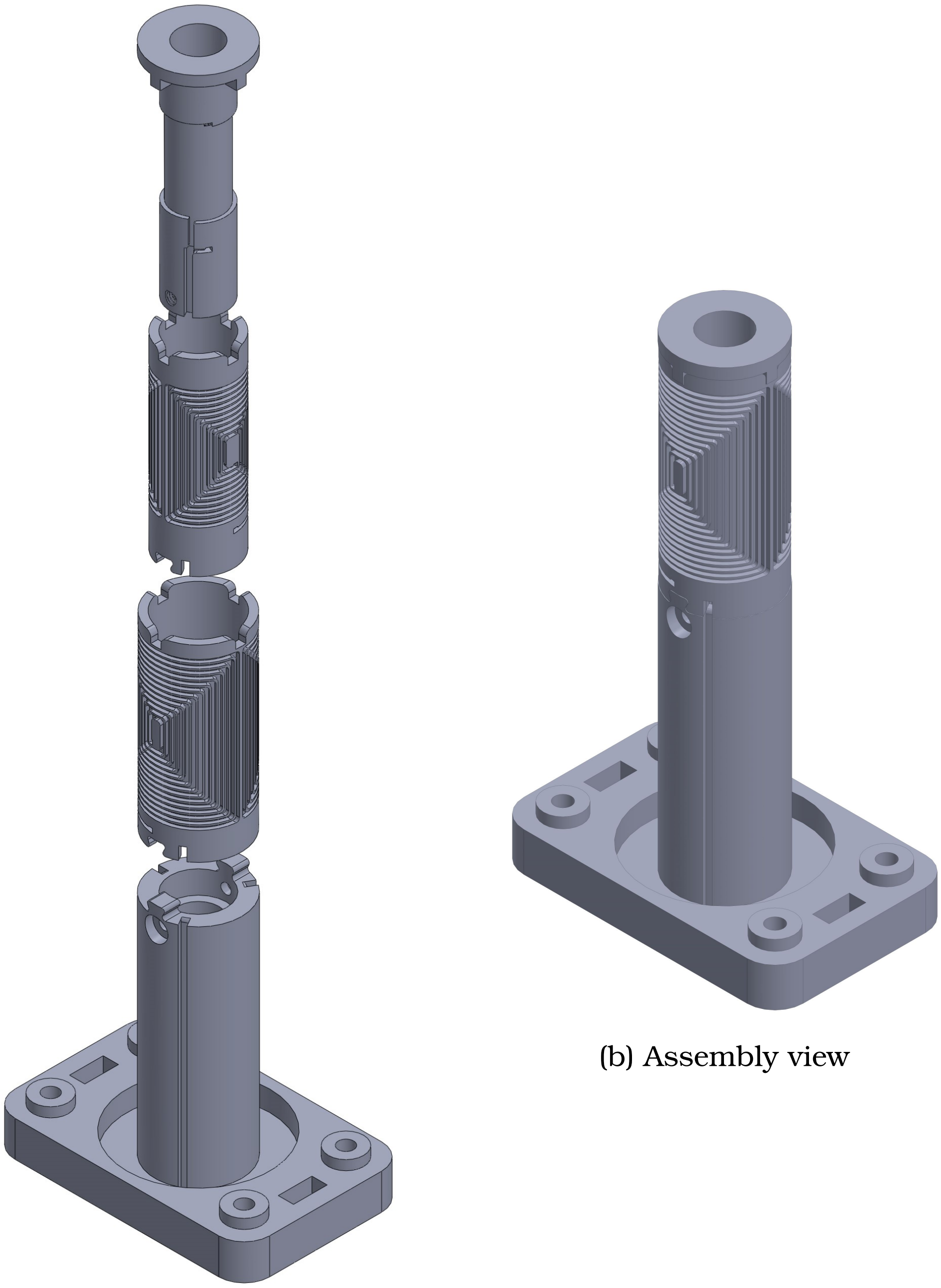

(b) Assembly view

(a) Coil formers

Figure 4.1: CAD models of the receive coil formers. (a) from the top down, it is former for the R_x-coil, R_y-coils, and R_z-coils, respectively; on the bottom is the base part used to connect the receive coil formers to the transmit coil frame. (b) is the assembled view of the coil formers, three cylindrical shells are mounted concentrically with the axis of each receive coil pointing in perpendicular directions.

Figure 4.2: Constructed receive coils in the coil formers. From left to right, it is former for the R_x-coil, R_y-coils, and R_z-coils, respectively; on the right is the base part used to connect the receive coil formers to the transmit coil frame.

Fig. 4.2. When being assembled, the three cylindrical shells were mounted concentrically with the axis of each receive coil pointing in perpendicular directions. The base part is an adapter, which is used to mount the receive coil formers to the transmit coil frame shown in Fig. 3.17.

4.1.3 Results and Discussion

After being assembled and mounted on the transmit coil frame, the parameters of the receive coils were measured. The results are shown in Table 4.1. The resistance of the coils in different coil units has slight variations due to the manufacturing, and the inductance values are nearly the same. From the measured resistance of the receive coils, the calculated averaged noise voltage for R_x, R_y, and R_z-coils are $49.2\,\mathrm{pV}/\sqrt{Hz}$, $55.3\,\mathrm{pV}/\sqrt{Hz}$, and $64.0\,\mathrm{pV}/\sqrt{Hz}$, respectively, at the temperature of $300\,\mathrm{K}$. The noise voltages are low enough so that the receive coils are not the dominant noise source in the receive chain. Hence, to achieve a high SNR, it is essential to build the receive coils with the highest possible sensitivity.

Table 4.1: Parameters of the receive coils

Coil Unit	R_x		R_y		R_z	
	R [mΩ]	L [µH]	R [mΩ]	L [µH]	R [mΩ]	L [µH]
Generation	145.4	2.6	179.6	3.0	249.8	5.4
Cancellation	146.9	2.7	188.9	3.0	244.8	5.4

The performance of the cancellation method was checked. A waveform generator, DG1032Z (RIGOL Technologies, Beijing, China), was used to send excitation signals at the fundamental frequency of each channel. An oscilloscope, HDO6104-MS (Teledyne LeCroy, New York, United States), first measured the received signals from the generation unit. Then, the receive coils from the generation and cancellation unit were connected in series with the inverse phase. The received signals were measured again to calculate the attenuation values. Excitation signals of different amplitudes were sent, and the attenuation values were averaged. The results are shown in Table 4.2. The receive chains in x-, y-, and z-channel are denoted by

R_x-, R_y-, and R_z-channel, respectively, according to the denotations of the receive coils. Compared to the −75 dB attenuation from [55], those values are not comparable. And the attenuation in R_x-channel is even worse than that in the other two channels. The lower attenuation values are because of the hardware imperfection. It is challenging to build two identical transmit coil and receive coil setups. However, more effort could be put into the construction process of the coils. Since the R_x-coil is a circular solenoid, another possible method is to design a gradiometer coil in the R_x-channel.

Table 4.2: Attenuation results of the cancellation method

Channel	R_x	R_y	R_z
Attenuation [dB]	−26.1	−43.1	−44.2

To further increase the sensitivity, the receive coil should be constructed in a shell with a smaller radius so that the coil could be closer to the sample vial, or the number of windings should be increased. The cylindrical shell had 1.5 mm thickness, and the wire used to wind the coils had 0.6 mm diameter, namely the thinnest part of the shell had only 0.9 mm thickness. The thickness of the groove wall on the formers was 0.3 mm. This pushed the limit of the 3D printer and the printing material. A better printer and material could be used to print the coil formers, but it is unlikely at a reasonable cost. It is more likely to improve the design to fit more windings. The grooves in the formers were designed to confine the wires. Though the thickness of the wall was only 0.3 mm, it still took up a lot of space. It could be possible to find a fast-cured adhesive to fix the wires so that the groove structure can be removed from the coil formers.

4.2 Band-Stop Filter

The receive coils can detect the changing magnetization of the MNPs, as well as the excitation signals sent from the transmit coils, which are orders of magnitude greater than the received particle signals. Since the excitation signal is at a single frequency in each channel, BSFs are commonly used to attenuate the coupled excitation signal. As mentioned in Section 2.3.3, a

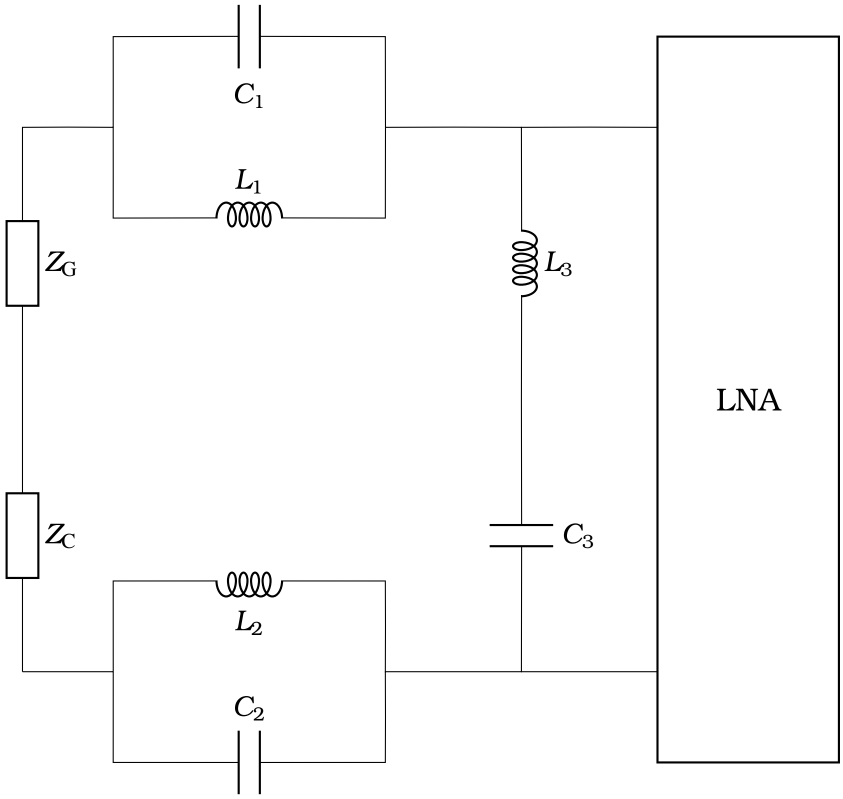

Figure 4.3: Schematic of the BSF. It is a second-order balanced LC filter. Z_G and Z_C denote the impedance of the receive coils in the generation unit and cancellation unit, respectively. Note that the schematic shows the BSF in only one channel.

cancellation unit was built. However, the results showed only attenuation of about 25–45 dB (see Table 4.2). BPFs were implemented to reduce the coupled excitation signals further.

The schematic of a second-order balanced BSF is shown in Fig. 4.3. As the LNA used later had differential inputs, the BSFs were designed to be balanced. A Bassel filter was chosen due to its flat response in phase, which reduces the waveform distortion. With the parameters of the receive coils (see Table 4.1), the BSFs were designed in FilterSolutions. Considering that the inductors would be self-built, while the capacitors would be chosen from commercially available capacitors or combinations of them, the values of the LC components were adjusted. The results are shown in Table 4.3. The simulated attenuation results of the BSFs are shown in Table 4.4.

Table 4.3: Values of the LC components in the BSFs

Channel	C_1, C_2 [nF]	L_1, L_2 [µH]	C_3 [µF]	L_3 [µH]
R_x	340	124.0	1.68	25.1
R_y	340	109.9	1.68	22.2
R_z	340	116.8	1.68	23.6

Table 4.4: Simulated attenuation results of the BSFs

Channel	1st [dB]	2nd [dB]	3rd [dB]
R_x	−65.3	−11.2	2.2
R_y	−65.6	−10.8	3.0
R_z	−71.6	−13.6	−0.9

The inductors L_3 were built similarly to the tunable inductors described in Section 3.4.2. However, the inductors L_1 and L_2 were built with iron powder cores. Since the receive signals were low in amplitude, it was unlikely to saturate the iron powder cores, limiting the disadvantages of contaminating the signals with higher harmonics. With the use of iron powder cores, it was able to build inductors with higher inductance but in smaller dimensions. The used iron powder cores T200-2 (Micrometals, California, United States) feature good performance in high frequency and low core losses. The tuning process of inductors L_3 was the same as described in Section 3.4.2, while the tuning of inductors L_1 and L_2 was done by increasing and decreasing the number of windings. The installed BSF is shown in Fig. 4.4. Note that the BSF in each receive channel is installed in a separate chassis.

After connecting the BSFs to the receive chain, a waveform generator, DG1032Z (RIGOL Technologies, Beijing, China), was used to send excitation signals at the fundamental frequency of each channel to the power amplifier. The voltage signals at the input and the output of the BSFs were measured by an oscilloscope, HDO6104-MS (Teledyne LeCroy, New York, United States), and then the attenuation values were calculated. The results are shown in Table 4.5. Compared to the simulation values (see Table 4.4), the measured results are lower than expected. However, these results are in an acceptable range. Together with the attenuation from

[redacted]

Figure 4.4: Installed BSF in the chassis. The receive coils in the generation and cancellation units are illustrated by Z_G and Z_C, respectively. Note that the BSF in each receive channel is installed in a separate chassis.

the cancellation method, the overall attenuation of the coupled excitation signals is about 90 dB.

Table 4.5: Measured attenuation results of the BSFs

Channel	R_x	R_y	R_z
Attenuation [dB]	−60.9	−51.5	−48.6

4.3 Low-Noise Amplifier

The induced nanoparticle signals in the receive coils are relatively low in amplitude, therefore, it is necessary to amplify the signals to match the dynamic range of the DAQ card. Matching the dynamic range of the DAQ card ensures a higher resolution when converting the analog signals to digital signals for post-processing. While amplifying, the noise introduced by the amplifier itself should be minimized to achieve higher SNR. An LNA is designed for this purpose.

A self-developed LNA [68] based on the LMH6553 (Texas Instrument, Texas, United States) was used in this study. The LMH6553 is a 900 MHz differential amplifier with an integrated adjustable output limiting clamp [70]. With the external gain set resistors, the LMH6553 was configured as a differential input to differential output and adjusted to match the dynamic range of the DAQ card. Fig. 4.5 shows the installed LNA together with the BSF in one chassis. Note that the LNA in only one channel is shown.

Figure 4.5: Installed LNA in the chassis. The printed circuit board (PCB) board is the self-developed LNA. It is installed together with the BSF in the same chassis. Note that the LNA in only one channel is shown.

CHAPTER 5

CONTROL UNIT

5.1 Data Acquisition Card

The DAQ card is a hardware with the analog to digital converter (ADC) and the digital to analog converter (DAC) that allow the input and output of analog and digital signals. In this study, different DAQ cards from Innovative Integration (California, United States) were used. X3-A4D4 [71] is a switched mezzanine card, or XMC, which features four 16-bit, 4 mega sample per second (MSPS) ADC channels, and four 16-bit, 50 MSPS DAC channels. It has differential inputs with (±10, ±5, ±2.5, ±1.25) V input ranges, and ±10 V output ranges. X3-10M [72] has eight 16-bit, 50 MSPS DAC channels with (±2, ±1, ±0.4, ±0.2) V input ranges. To synchronize the performance of multiple DAQ cards, an X3-Timing card [73] is needed. It has four output clocks, four output triggers, a clock/reference input, and a trigger input. As seen from Fig. 5.1, two X3-A4D4 cards, one X3-10M card, and one X3-Timing card are used in this MPS.

With the help of the XMC to peripheral component interconnect (PCI) adapter cards [74], all DAQ cards were installed directly on the motherboard of the PC. Breakout boards (Institute of Medical Engineering, University of Lübeck, Germany) were used to bring the 68-pin mini delta ribbon (MDR) connectors on the adapter cards out to subminiature version A (SMA) connectors. SMA connectors are coaxial radio frequency connectors that minimize reflections and attenuation at higher frequencies. Note that the adapter cards and the breakout cards are not shown in Fig. 5.1. On one X3-A4D4 card, 3 DAC ports were used to send excitation signals to the power amplifier, 3 ADC ports were used to receive the signals from the feedback, and the digital input/output (I/O) ports were used to control the H-bridges. On the second X3-A4D4 card, 3 DAC ports were used for analog programming of the DC sources. The X3-10M card was used to receive the signals from the LNAs. The X3-Timing card synchronized the performance of other DAQ cards.

5.2 Feedback

To precisely generate the desired magnetic fields, a feedback mechanism was implemented to monitor the current flowing in the coil. According to the

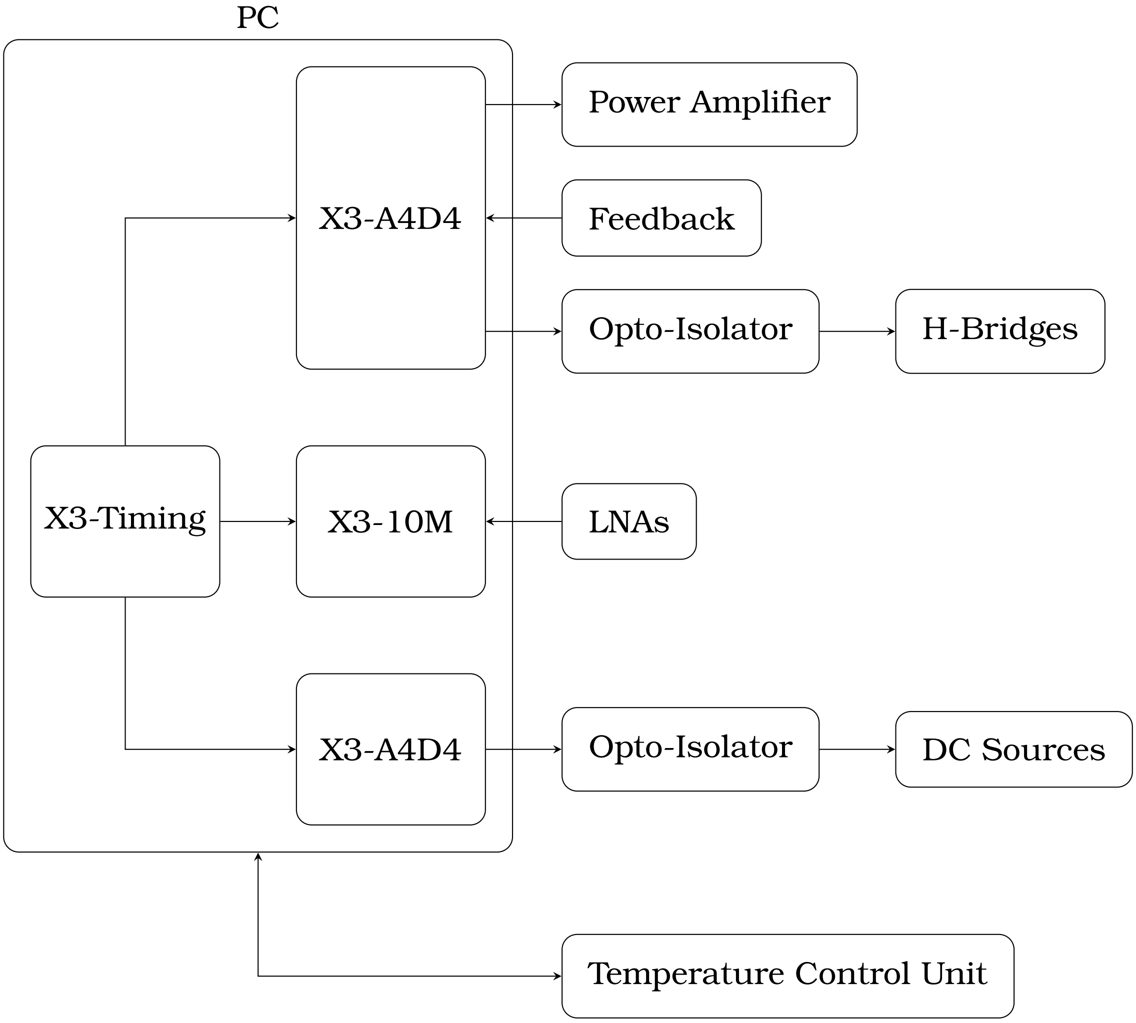

Figure 5.1: Connection diagram of the control units. On one X3-A4D4 card, 3 DAC ports are used to send excitation signals to the power amplifier, 3 ADC ports to receive the signals from the feedback, and the digital I/O ports are used to control the H-bridges. On the second X3-A4D4 card, 3 DAC ports are used for analog programming of the DC sources. The X3-10M card receives the signals from the LNAs. The X3-Timing synchronizes the performance of other DAQ cards. The temperature control unit is connected to the PC via universal serial bus (USB) ports. Two opto-isolator circuitries are used to control the H-bridges and DC sources safely and precisely.

Biot-Savart law (see Eq. (3.2)), the magnetic fields generated by the transmit coils are proportional to the currents flowing in them. For monitoring the magnetic fields, instead of directly measuring the field strength, an easier method is to measure the current. In order to minimize the disturbance to the transmit coils, in this study, Rogowski coils were used as feedback components.

A Rogowski coil is an electrical device commonly used to measure AC, and it works on the principle of Faraday's law. As shown in Fig. 5.2, a typical Rogowski coil is a toroidal coil with a non-magnetic core that encircles the conductor which carries the current. The output of the Rogowski coil is proportional to the rate of change of current flowing through the conductor.

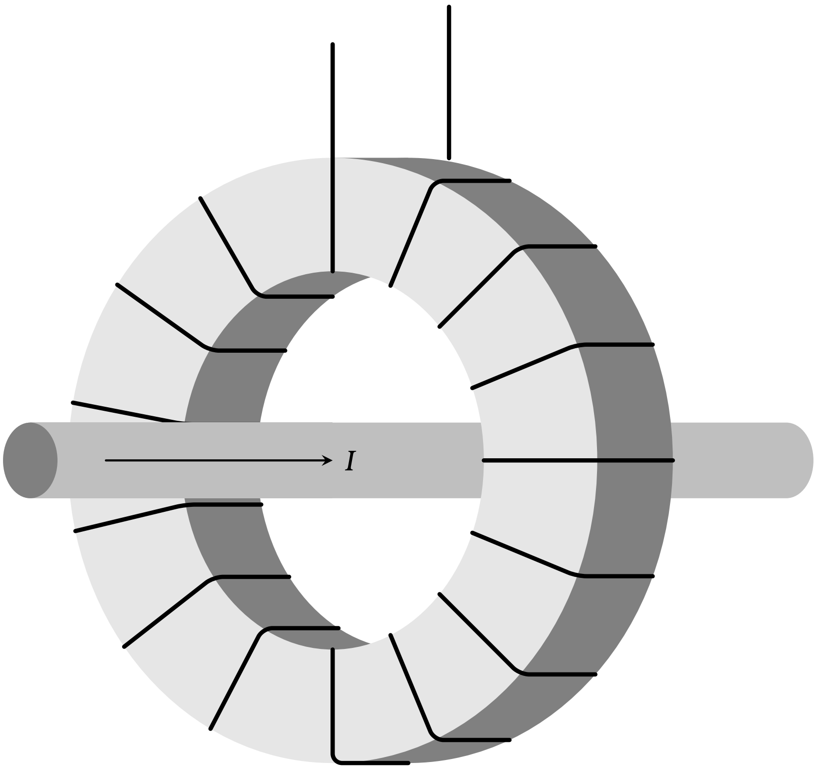

Figure 5.2: Illustration of a Rogowski coil. It is a toroidal coil with a non-magnetic core that measures the current through a conductor encircled by the coil.

According to the Ampère's circuital law, the integrated magnetic field B around a closed loop C is expressed as

$$\oint_C B \cdot \mathrm{d}\ell = \mu_0 I \,, \tag{5.1}$$

where $\mathrm{d}\ell$ is the infinitesimal element of C, I is the current flowing through the conductor enclosed by C, and μ_0 is the vacuum permeability. Taking Eq. (5.1) into consideration, for a Rogowski coil of rectangular cross-section, which is illustrated in Fig. 5.3, the induction electromotive force can be calculated as [75]

$$\begin{aligned}\epsilon &= -N\frac{\mathrm{d}\varphi}{\mathrm{d}t} \\ &= -N\frac{\mathrm{d}}{\mathrm{d}t}\iint_S B\, dS \\ &= -N\frac{\mathrm{d}}{\mathrm{d}t}\int_a^b \frac{\mu_0 Ih}{2\pi r}\,\mathrm{d}r \\ &= -\frac{N\mu_0 h}{2\pi}\cdot \ln\frac{b}{a}\cdot\frac{\mathrm{d}I}{\mathrm{d}t} \,,\end{aligned} \tag{5.2}$$

where S is the cross-section area, which equals the height h times the difference between the inner radius a and the outer radius b. φ is the magnetic flux, and N is the number of windings. Let M be the mutual inductance between the conductor and the Rogowski coil, Eq. (5.2) can be written as

$$\epsilon = M\frac{\mathrm{d}I}{\mathrm{d}t} \,. \tag{5.3}$$

If the current I flowing through the conductor is sinusoidal of magnitude I_m and frequency f, then the voltage induced is given by

$$\epsilon = M \cdot \mathrm{I}_m \cdot 2\pi f \cos 2\pi f t \,. \tag{5.4}$$

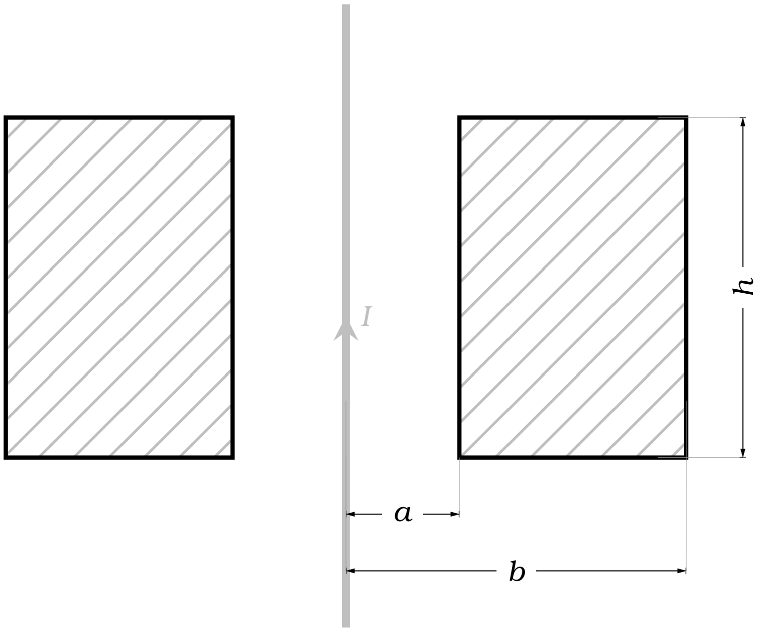

Figure 5.3: Rogowski coil with a rectangular cross-section. The Rogowski coil of inner radius a, outer radius b, and height h encircles a conductor with current I.

Figure 5.4: Self-built Rogowski coil. The copper wire is wounded on a 3D printed coil former with a rectangular cross-section. The former has 12 mm inner radius, 15 mm outer radius, and 40 mm height.

Hence, the magnitude of the induced signal is proportional to the current flowing through the conductor and the frequency of the current.

In each transmit channel, the Rogowski coil was used to measure the current at a single frequency. Therefore, an integrator circuit normally associated with the Rogowski coil was not implemented in this study. The Rogowski coils were connected directly to the DAQ card. The geometrical sizes of the Rogowski coils were not optimized to achieve the highest voltage output. Instead, the primary design consideration was the space limitation of the chassis in which the Rogowski coils needed to be installed. A self-built Rogowski coil is shown in Fig. 5.4. The coil former was printed with the PLA material by Ultimaker 2 (Ultimaker, Utrecht, Netherlands). It has 12 mm inner radius, 15 mm outer radius, and 40 mm height. The number of windings was adjusted to match the ±1.25 V input range of the X3-A4D4 card.

5.3 Temperature Control Unit

In order to maintain and adjust the temperature of the nanoparticle samples, a temperature control unit needs to be built. According to the Section 3.1.3, the inner radius of the T_x-coil is 13 mm. This cylindrical space is where the components of the temperature control unit should be constructed.

As shown in Fig. 5.5, two pipes with different diameters are placed concentrically. The outer pipe has a diameter of 25 mm and the inner pipe has a diameter of 20 mm. Both pipes have a wall thickness of 1 mm, which forms a 1.5 mm thick cylindrical shell in between. Two fixtures are used to constrain the positions of the pipes, and they are fastened to the transmit coil frame shown in Fig. 3.17. The inlet and outlet on the fixtures are connected to the water tubes so that the water can flow between the pipes. The same structures are built in both the generation unit and the cancellation unit. The space inside the inner pipe has a diameter of 18 mm, which is the place for measuring the nanoparticle sample, called the sample chamber. When the water of a specific temperature is circulating, the heat dissipated from the water transfers to the sample chamber, which leads to a thermal equi-

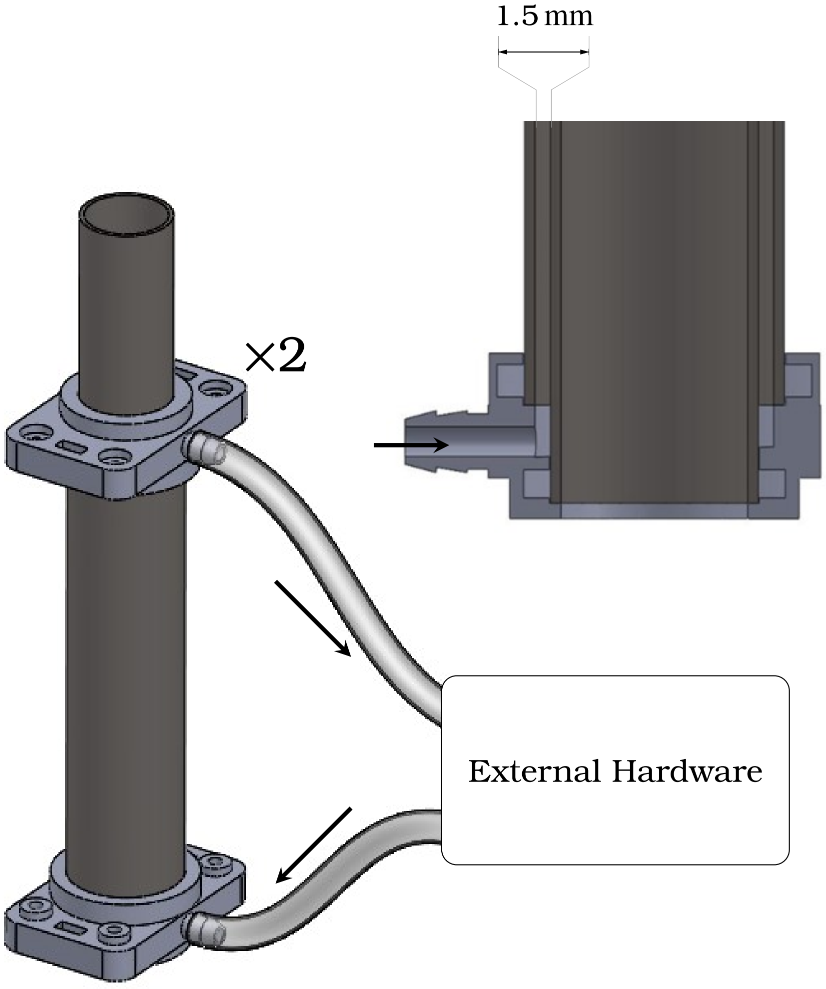

Figure 5.5: Illustration of the temperature control unit. The outer pipe has a diameter of 25 mm, and the inner pipe has a diameter of 20 mm. Both pipes have a wall thickness of 1 mm, which forms a 1.5 mm thick cylindrical shell in between. Two fixtures are used to constrain the positions of the pipes, and they are fastened to the transmit coil frame shown in Fig. 3.17. The inlet and outlet on the fixtures are connected to the water tubes so that the water can flow between the pipes. A cross-section view of the lower fixture and part of the pipes is shown in the upper right corner. The arrows indicate the flow of the water. The same structures were built in both the generation unit and the cancellation unit. The detail of the external hardware is shown in Fig. 5.6.

librium in this space. Therefore, when the sample is placed in the sample chamber, the temperature change of the circulating water will influence the temperature of the samples. Moreover, the water between the pipes works as an isolation to prevent the heat of transmit coils from transferring to the sample chamber.

The system diagram of the temperature control unit is shown in Fig. 5.6. The water is circulated by a water pump DC-LT 3600 (Alphacool, Braunschweig, Germany). A water reservoir for the DC-LT pump made by Alphacool is also used. It is the fill point in the hydronic system. Since it is made of transparent material, the water level could be directly monitored from outside. A temperature sensor, DS18B20 (AZ-Delivery, Deggendorf, Germany), in the form of a waterproof stainless steel probe is inserted into the reservoir to monitor the water temperature. The water flows through a cold plate CP4A-114B-108E (Ohmite, Illinois, United States), on which four Peltier elements, TEC-40-36-127 (Wakefield-Vette, New Hampshire, United States), are attached. A cooling plate is often an aluminum block embedded with metal tubes. A Peltier element or thermoelectric cooler (TEC) is usually a flat plate component that uses electricity to transfer heat from one side to the other, namely making one side hot and one side cold. Depending on the current direction, it can be used for heating or cooling. Four Peltier elements are attached to the cooling plate so that the heat from the Peltier elements can transfer by conduction through the cooling plate and the embedded metal tubes to the water flowing in it. The other sides of the Peltier elements are attached to a heat sink with fans mounted on it. The performance of the Peltier elements largely depends on the temperature difference between the two sides. The power supply, HRPG-600-12 (Mean Well, Taiwan, China), has an output power of 600 W and an output voltage of 12 V. It powers the Peltier elements, the pump, and the fans via relays. Three 4-channel 5 V relay modules (Elegoo, Shenzhen, China) are installed so that the Peltier elements, the pump, and the fans can be turned on or off. A single-board microcontroller, Arduino Mega 2560, is used to receive the temperature measurement from the sensor and to control the relays. The Peltier elements are connected to the relay in a way, that the current directions can be controlled via the Arduino board. The components inside

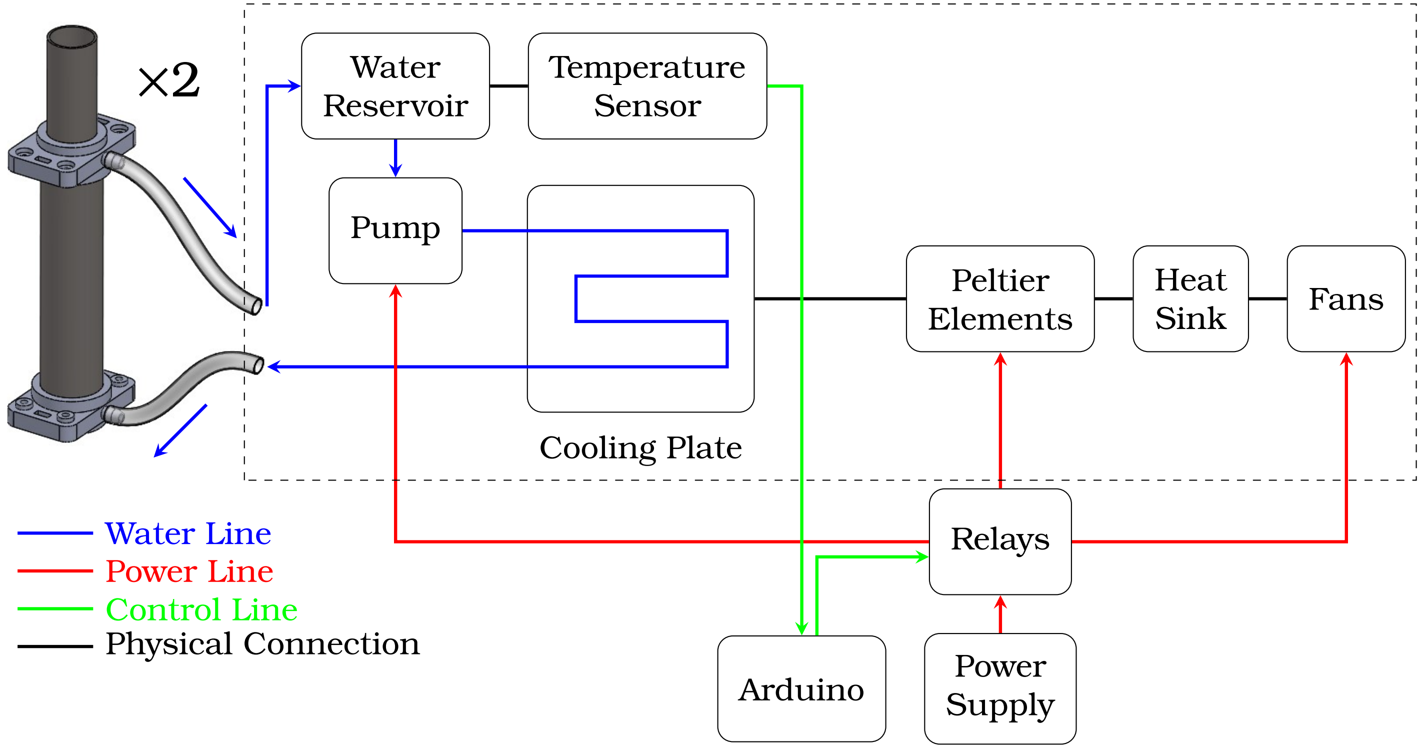

Figure 5.6: Diagram of the temperature control unit. The water is circulated by the pump through the cooling plate, where the Peltier elements are attached. The heat from the Peltier elements could transfer by conduction through the cooling plate to the water flowing in it. The other sides of the Peltier elements are attached to the heat sink with fans mounted on it. A temperature sensor is inserted into the water reservoir to monitor the water temperature, which is measured by the Arduino to control the relays. The components in the dashed frame are shown in Fig. 5.7. The power supply, relays, and Arduino board were installed together into a chassis shown in Fig. 2.6(a).

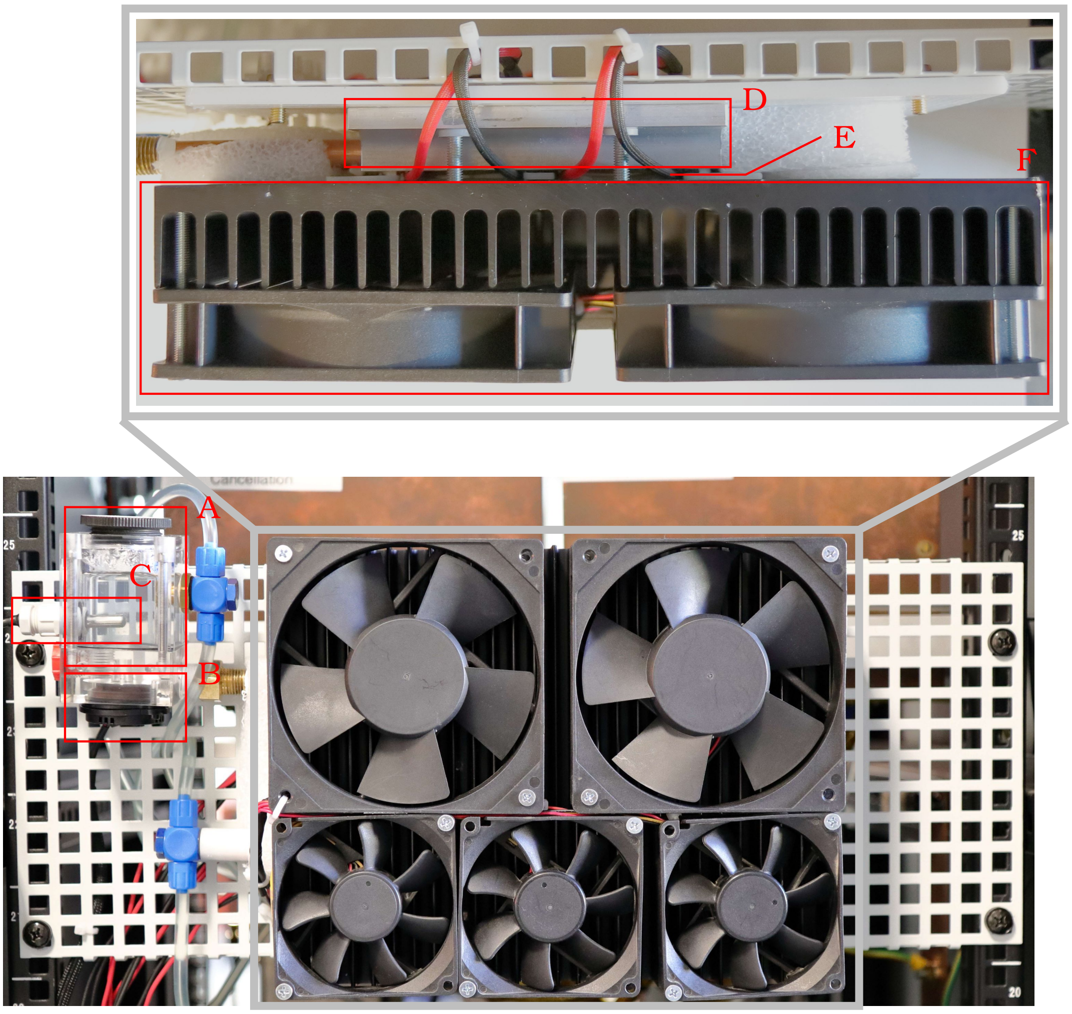

Figure 5.7: Components of the temperature control unit. The upper picture is the top view of the indicated part. A: water reservoir; B: pump; C: temperature sensor; D: cooling plate; E: Peltier elements; F: heat sink with fans. Note that only part of the components is shown. The Peltier elements are pressed in between the cooling plate and the heat sink. These components are mounted on a pegboard and then installed on a 19-inch rack (see Fig. 2.6(b)).

the dashed frame in Fig. 5.6 are shown in Fig. 5.7. These components were mounted on a pegboard and then installed on a 19-inch rack (see Fig. 2.6(b)). The power supply, relays, and Arduino board were installed together into a chassis shown in Fig. 2.6(a). The Arduino board was connected to the PC via a USB port.

A self-developed program was implemented to control the temperature of the circulating water. Part of the codes is shown in Appendix B. According to the difference between the set temperature and the water temperature, the Peltier elements could heat or cool the water. A hysteresis control was designated to avoid frequently switching on and off. The temperature control unit is able to adjust the circulating water from 10 °C to 60 °C with a deviation of 0.2–0.5 °C. In order to monitor the temperature in the sample chamber, a water sample is prepared and placed in the sample chamber of the cancellation unit. A fiber-optic probe, PRB-100 (Osensa Innovations, Burnaby, Canada), is inserted into the water sample to measure the temperature. Since the structures for controlling the temperature are identical in both the generation unit and the cancellation unit, the temperatures in both sample chambers are identical. Therefore, it is reasonable to assume that the temperature of the water sample is equal to the particle sample if it is in water suspension.

For the samples to reach the set temperature, an equilibrium in the sample chamber should be reached. Depending on the set temperatures, a delay of about 10–20 min would occur after setting. Additionally, a temperature difference between the set temperature and the temperature in the sample chamber happened at a higher or lower temperature. However, it could be easily improved by including the reading of the fiber-optic probe into the control loop of the program, which unfortunately has not been done during this study. Another improvement to decrease the delay time, as well as increase the stability of the temperature, is to implement the so-called proportional–integral–derivative (PID) controller in the program.

5.4 Opto-Isolator and Power Supply

An opto-isolator is an electronic component that transfers electrical signals from one circuit to another by optical transmission. The optoisolator typically converts the electrical signals into light using an LED and then directs the light towards a photodiode, which converts the optical signals back into electrical signals. This isolates the two circuits, prevents voltage spikes, and decreases noise and interference. As seen from Fig. 5.1, two opto-isolator circuitries are implemented to safely and precisely control the H-bridges and the DC sources, respectively. Noted from Section 3.5, the control signal level for the H-bridges is 24 V. While the logic signal level of the digital I/O ports on the A4D4 card is 2.5 V low voltage transistor–transistor logic (LVTTL). In order to isolate the H-bridges and the DAQ card, an opto-isolator circuitry utilizing the 4N25 (Vishay Intertechnology, Pennsylvania, United States) [76] was designed. See Section 3.5, the output of the DC sources could be controlled via analog programming, which utilizes an external analog voltage. However, to prevent earth loops that could cause programming errors, an opto-isolator circuitry was implemented. A linear optocoupler IL300 (Vishay Intertechnology, Pennsylvania, United States) [77] was used, which was able to compensate for the LED's non-linear, time, and temperature characteristics. So that the stability of the input–output gain was insured. The circuit diagrams are shown in Appendix C. The two opto-isolator circuitries were built into separate chassis, shown in Fig. 2.6(b).

Due to the high-frequency electrical noise associated with the switched-mode power supply, the linear power supply was used to reduce interference. A 5 V power supply, CD 5.1,5 (Kniel, Karlsruhe, Germany) [78], was used to supply the LNAs. A 24 V power supply, CLDO 24.2,5 (Kniel, Karlsruhe, Germany) [79], was used to supply the H-bridges and the opto-isolator circuitry for the H-bridges. A 12 V power supply, PSM 112 (Schroff, Straubenhardt, Germany) [80], was used to supply the opto-isolator circuitry for the DC sources and the fans in the MPS system. All the power supplies were mounted directly on the 19-inch rack shown in Fig. 2.6(a).

CHAPTER 6

MEASUREMENTS

6.1 Calibration

Before conducting any quantitative measurement, the MPS system was calibrated. In the transmit chain, the calibration was made so that the magnetic fields could be generated accurately. In the receive chain, the measured voltage signals could then be transferred to the magnetic moment of the MNPs.

6.1.1 Calibration Coil

Calibration coils were designed for calibrating the drive fields (Section 6.1.2) and recording the transfer function (Section 6.1.4). In Fig. 6.1, calibration coils with different tips are shown. Since the transmit coils in each channel are in perpendicular directions, the calibration coil with tip A is designed for the x-channel, while the one with tip B is for the y-channel and the z-channel. The calibration coils were built by winding a thin copper wire (BLOCK, Verden, Germany) of $0.1\,\mathrm{mm}$ diameter at the tip part to form a circular solenoid coil of $3\,\mathrm{mm}$ diameter. The winding number is 4. The body part of the calibration coil was printed by Projet 3510 HD Plus (3D Systems, South Carolina, United States) because of its high accuracy.

The circuit schematic of the calibration coil is shown in Fig. 6.2. For calibrating the drive fields, the applied magnetic field is measured by the calibration coils. Derived from Faraday's law of induction, the applied time-varying magnetic field can be calculated as

$$B(t) = -\frac{u_{\mathrm{Port1}}(t)}{\omega AN}\,, \tag{6.1}$$

where u_{Port1} is the voltage signal measured at Port1, N is the number of windings of the calibration coil, A is the cross-section, and ω is the angular frequency.

For recording the transfer function, the calibration coils are used to generate the magnetic moment. The magnetic moment generated by the coil is calculated as

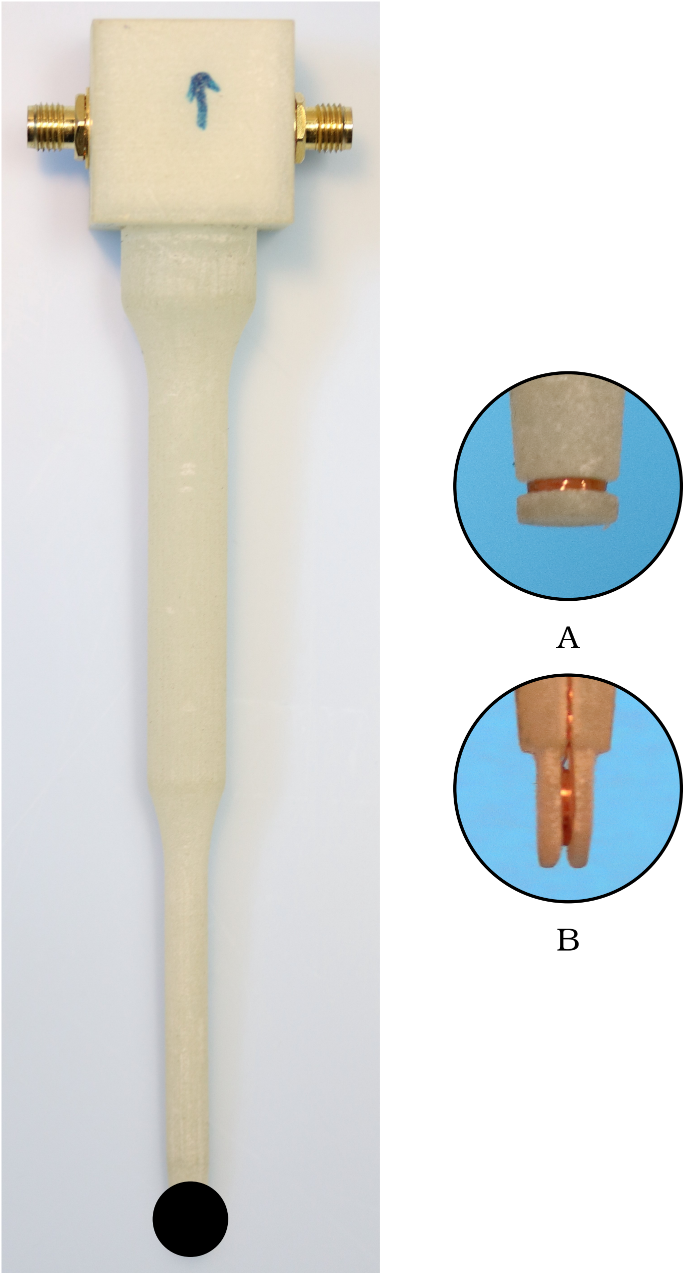

Figure 6.1: Calibration coil with different tips. The copper wire is wound on at the tip part to form a circular solenoid coil. Since the transmit coils in each channel are in perpendicular directions, the calibration coil with tip A is designed for the *x*-channel, while tip B is for the *y*-channel and *z*-channel.

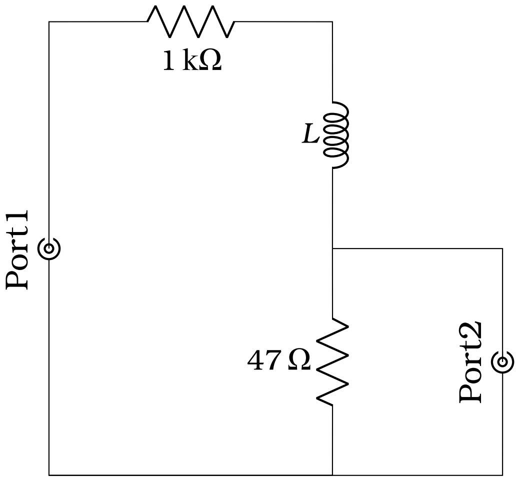

Figure 6.2: Schematic of the calibration coil. L indicates the coil wound at the tip of the calibration coil. Port1 and Port1 are SMA connectors used in the calibration process.

$$\begin{aligned}\mathbf{m} &= NIA\hat{\mathbf{n}} \\ &= N\frac{u_{\text{Port2}}}{47\,\Omega}A\hat{\mathbf{n}}\,,\end{aligned} \tag{6.2}$$

where N is the number of windings, A is the cross-section, and $\hat{\mathbf{n}}$ is the unit normal vector of the cross-section. I is the current applied on the coil, which can be calculated by the voltage measured at Port2 divided by the known resistance of 47 Ω.

6.1.2 Drive Field Calibration

The drive fields produced by the transmit coils are controlled by the excitation signals sent from the PC. A common consideration of the calibration is to calculate the ratio between the voltage of the signal sent from the PC and the magnetic field measured at the central point in the transmit coils, where the particle samples are placed. However, during the measurement, the temperature of the coils would change, which leads to a change in the resistance and then a change in the power needed to be applied. Therefore, the voltage of the sending signals should be varied to compensate for any interference. Namely, a fixed ratio value will lead to a deviation in the generated magnetic field. According to the Biot-Savart law (see Eq. (3.2)), the generated magnetic field is proportional to the current in the coil. Thus, a more acceptable calibration method involves the feedback coil introduced in Section 5.2. The generated magnetic field is proportional to the voltage signal of the feedback coil at a known frequency.

During the calibration of the drive field, the tip of the calibration coil was inserted into the center of the transmit coils. An excitation signal was sent from the DAQ cards to the power amplifier, then the Port1 of the calibration coil and the feedback coils were connected to the DAQ cards to record the voltage signals. Because the impedance of the calibration coil is frequency-dependent, the excitation signals were sent at every drive field frequency (24.51 kHz, 26.04 kHz, and 25.25 kHz) in each channel. The recorded voltage signals from the calibration coil were used to calculate the magnetic field (see Eq. (6.1)). Then, the magnetic field and the feedback signals were calculated to get the amplitude ratio with a unit of [V/mT] and the phase shift between them. With the calibration data, the drive fields could be accurately generated with the desired amplitude and phase by monitoring the feedback. During measurement, the deviation of the feedback signals was used to adjust the excitation signals sent to the power amplifier.

6.1.3 Offset Field Calibration

The offset fields are generated by the DC sources applying currents on the transmit coils. Noted from Section 3.5, there are two methods of controlling the current applied by the DC sources. One is digital programming, while the other is analog programming. Both programming methods were calibrated in this study. For measuring the static magnetic field, a 3-channel Gaussmeter, Model 460 (Lake Shore, Ohio, United States), with a hall probe (MMZ-2508-UH) was used.

First, for digital programming, the current values are sent by the PC via SCPI commands. In the calibration process, defined current values with steps were sent by the PC, and the produced magnetic field was measured at the center point of the transmit coils by the Gaussmeter. A mean ratio with unit [A/mT] was then calculated for each transmit channel. With the ratio values, the desired offset fields were generated by sending the correct current values to the DC sources.

Second, for analog programming, the signal level sent from the DAQ cards controls the current sent by the DC sources. As mentioned in Section 5.4, an opto-isolator circuitry was built to prevent earth loops. The input–output gain was adjusted. Despite linear optocouplers being utilized, the calibration was indispensable for accurately controlling the current. In the calibration process, defined voltages were sent with steps from the DAQ cards, and the produced magnetic field was measured by the Gaussmeter. A ratio array with unit [V/mT] was then calculated for each channel. With the ratio arrays, the desired offset fields were generated by sending correct voltage signals from the DAQ cards to the DC sources.

6.1.4 Transfer Function

The MNP signals are induced as a voltage in the receive coil (see Eq. (2.8)). In order to restore the magnetic moment of the measured MNPs, the transfer function is indispensable. The transfer function describes the transformation from the magnetic moment of the MNPs to the receive voltage signals [24].

During the calibration, a sawtooth wave at calibration frequency f_c was sent to the calibration coil through Port1. The receive channels of the MPS and the Port2 of the calibration coil were connected to the DAQ cards. The received time signals were then processed in the frequency domain to calculate the transfer function as

$$\hat{\mathrm{TF}} = \frac{\hat{u}_{\mathrm{rec}}}{\hat{m}}, \tag{6.3}$$

where $\hat{u}_{\mathrm{rec}}$ is the receive signals, and $\hat{m}$ is the calculated magnetic moment (see Eq. (6.2)). The sawtooth wave was chosen because it contains every harmonic of the fundamental frequency f_c, and therefore covers the bandwidth of the MPS system. However, during the calibration, sine waves at

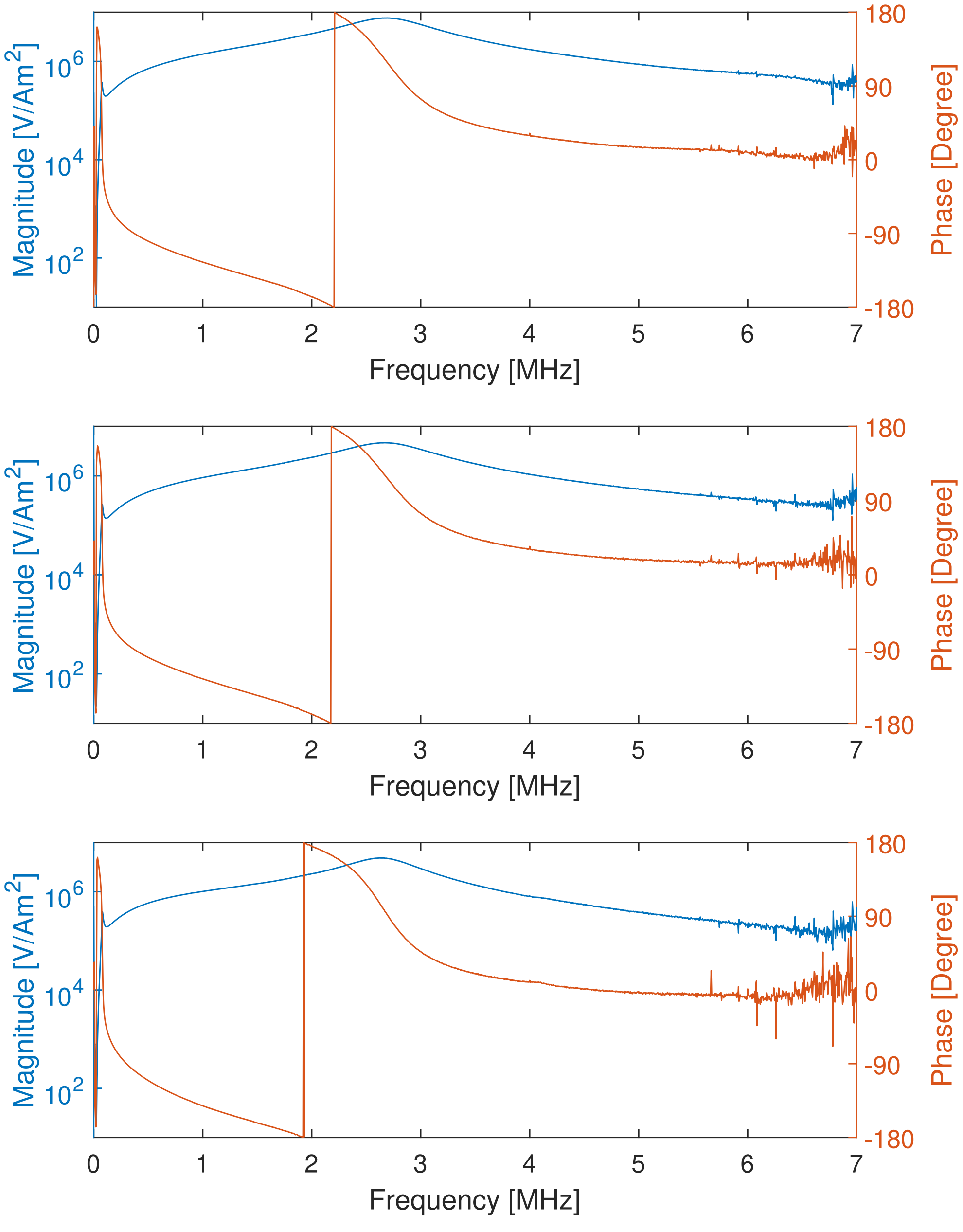

Figure 6.3: Transfer function of each receive channel. From top to bottom, is the transfer function for R_x-, R_y-, R_z-channel, respectively. The magnitude of the transfer function is shown in blue, while the phase is shown in red.

an internal of f_c from 0 to 200 kHz were applied to the calibration coils as well. This was to increase the accuracy of the transfer function in the low-frequency range due to the filter stages. The measured transfer function of each receive channel is shown in Fig. 6.3.

6.2 Nanoparticle Sample

Before conducting the measurement, the nanoparticles were prepared in a sample vial (0.6 mL micro-centrifuge tube). A sample holder was specifically designed to fit the vial in and then insert it into the sample chamber. A mechanical structure was also designed to be mounted on the outside of the coil shield. It ensured that the sample holder could be fastened during the measurement, and its vertical positions could be slightly adjusted so that the sample vial would be placed in the center position. For nanoparticle measurement, the DC sources and the H-bridges were not connected to the system since the offset field was not necessary to generate.

6.2.1 Resovist

In order to test the functionality of the 3D MPS, Resovist (Bayer Schering Pharma, Berlin, Germany) as a "good standard" nanoparticle was used. It is a carboxydextrane-coated SPION consisting of clusters of single domain particles, and its undiluted iron concentration is 500 mmol/L, or 27.9 mg/mL.

A 10 µL sample was prepared for measurement. The temperature of the sample was at room temperature 22 °C. The drive field amplitudes were $20\,\mathrm{mT}/\mu_0$, and the frequencies were 24.51 kHz, 26.04 kHz, and 25.25 kHz, for the T_x-, T_y-, and T_z-channel, respectively, as mentioned in Section 2.3.1. One period of measurement was about 21.54 ms, and 100 periods were measured for averaging. Two empty measurements were taken without the samples being placed. The magnitude spectra of the particle sample are shown in Fig. 6.4. The blue spectra are the particle measurement subtracting the empty measurement. The red spectra are the difference between two empty measurements, which are the remaining background signals. In the R_x-channel, the highest received harmonic is 81st harmonic

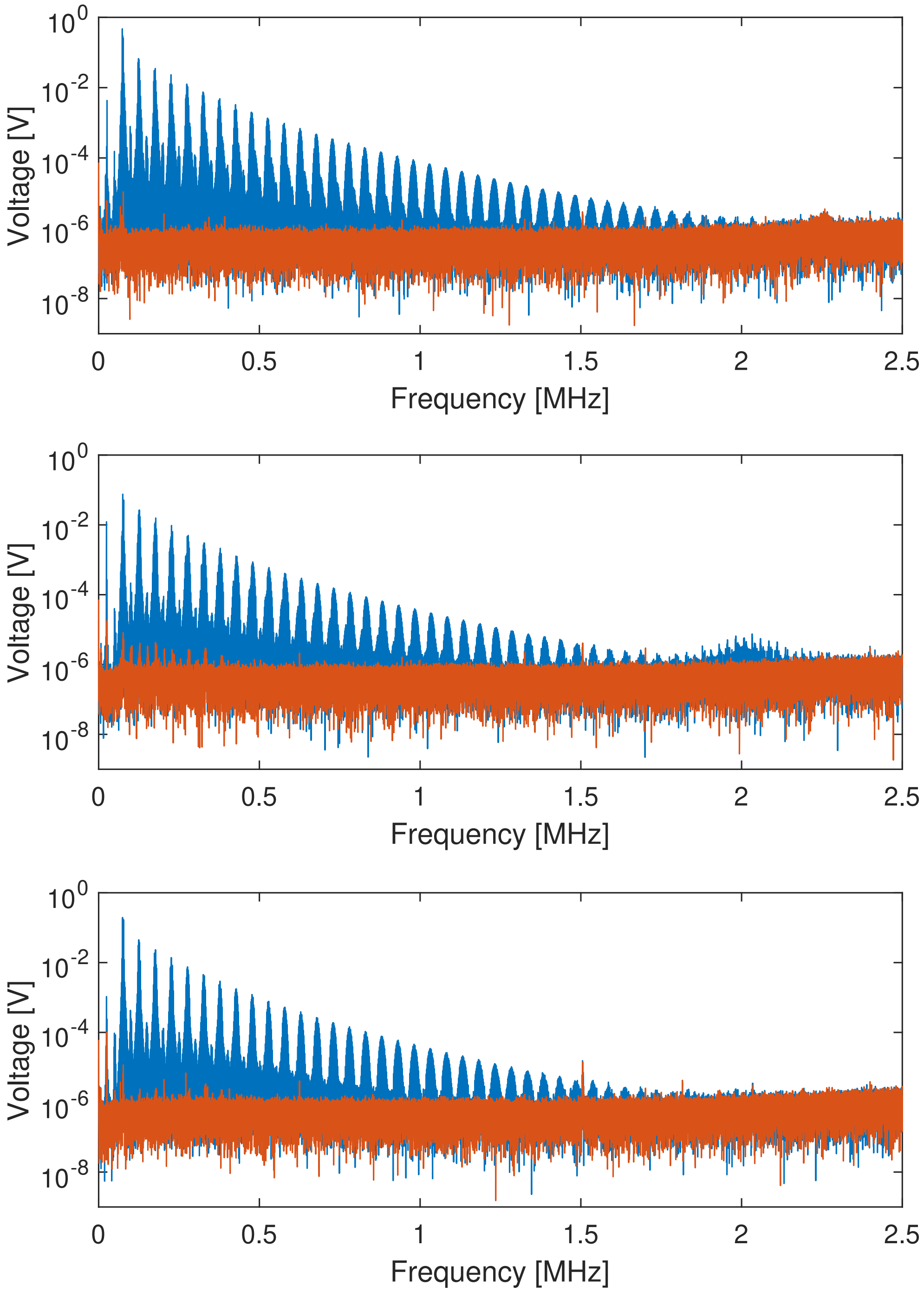

Figure 6.4: Magnitude spectra of the Resovist sample. The results of the particle measurement with empty measurement subtraction are shown in blue. The red spectra are the difference between two empty measurements, which are the remaining background signals. Upper: R_x-channel; middle: R_y-channel; lower: R_z-channel.

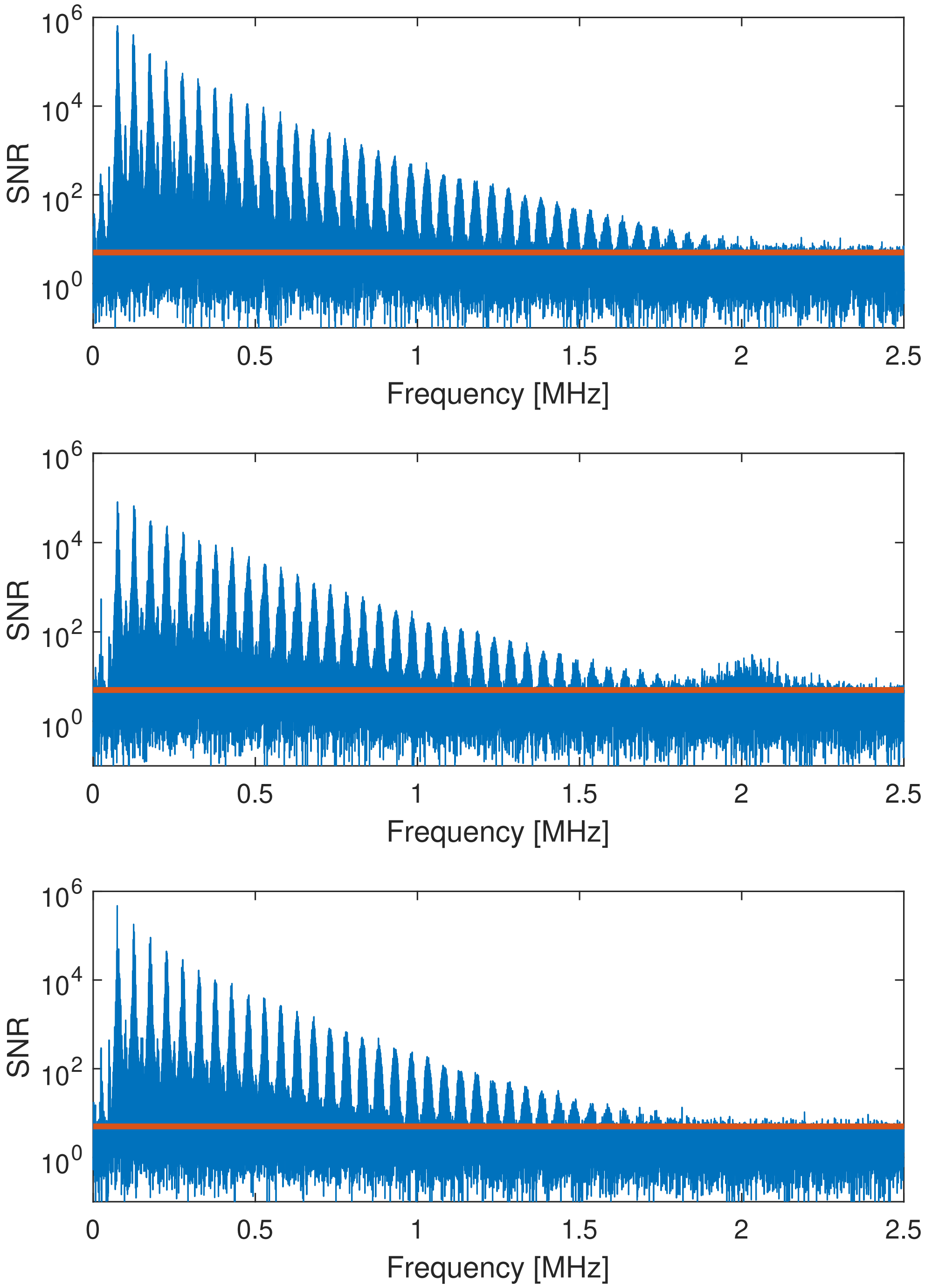

Figure 6.5: SNR results of the Resovist sample. The SNR results are shown in blue, and the red line indicates SNR = 5. Upper: R_x-channel; middle: R_y-channel; lower: R_z-channel.

at about 2.0 MHz, while in the R_y-channel it is 71st harmonic at about 1.9 MHz , and in the R_z-channel 69th harmonic at about 1.7 MHz. However, it could be observed that there is a resonance peak at about 2 MHz in the R_y-channel. Further inspection should be conducted to find out the causes.

According to the Rose criterion [81], an SNR of at least 5 is considered to distinguish the harmonics from the background noise. The SNR at frequency k is calculated by

$$\mathrm{SNR}_k = \frac{\hat{u}_k}{\mathrm{std}(\hat{n}_k)}\,, \tag{6.4}$$

where $\hat{u}_k$ is the magnitude spectra of the particle measurement with empty measurement subtraction, $\mathrm{std}(\hat{n}_k)$ is the standard deviation of the remaining background signals. Here, the empty measurement was recorded 100 times to calculate the standard deviation. As seen from Fig. 6.5, the largest SNR appears at the 3rd harmonic frequency in every channel. In the R_x-channel, the largest SNR is 6.5×10^5. While in the R_y- and R_z-channel, it is 8.1×10^4 and 4.7×10^5, respectively. In comparison to an MPI scanner of SNR about 100–1000, this is a huge advantage. The SNR results are comparable with that of the 2D MPS introduced in [24]. Although the drive field in this study was higher, the averages were only half. Compared to the previously developed 3D MPS [25], the SNR results are about 10 times better.

6.2.2 Nanomag

In the next experiments, nanoparticles with different diameters were compared. Four different nanoparticles (see Table 6.1) from micromod Partikeltechnologie (Rostock, Germany) were chosen. These nanoparticles are comprised of a small iron core embedded in a dextran matrix, with additional plain surface functionality [82]. Samples of 10 µL without dilution were prepared for measurement.

The drive field amplitudes and frequencies were the same as the previous measurement, as well as the temperature of the particle sample and the measurement sequence. In Fig. 6.6, the magnitude spectra of different sample measurements with empty measurement subtraction are shown,

Table 6.1: Nanomag particle sample list

Particle name	Production name	Diameter [nm]	Iron Concentration [mg/ml]
Sample A	Nanomag-D	500	*
Sample B	Nanomag-D	250	*
Sample C	Nanomag-D-spio	100	2.4
Sample D	Nanomag-D-spio	20	2.4

* no information found.

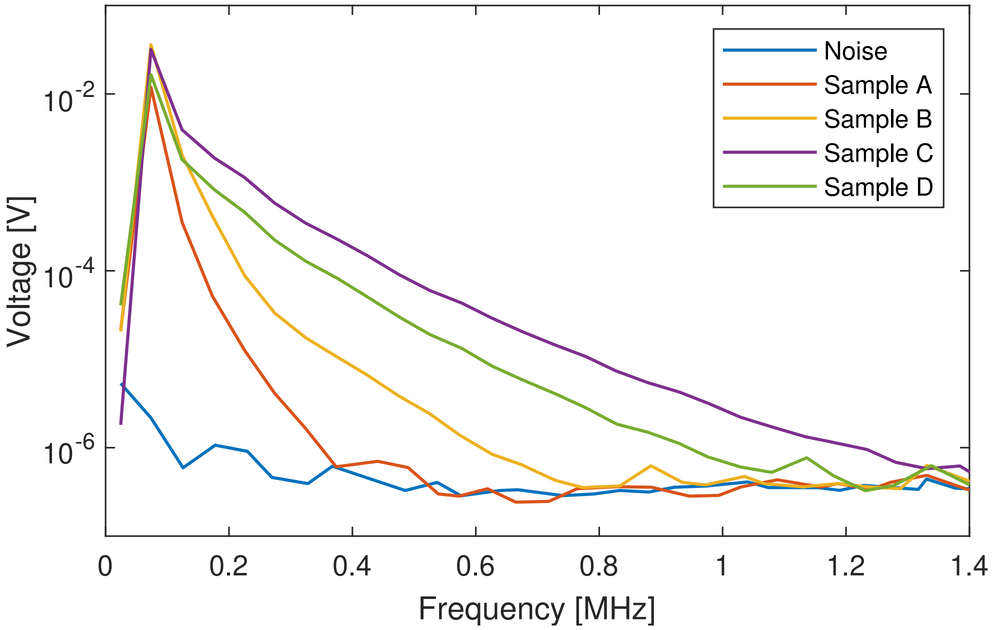

Figure 6.6: Magnitude spectra of the Nanomag samples. Four different particle samples, as well as the background noise, are plotted for comparison. Note that only the signals of the R_x-channel are shown here, while in the R_y- and R_z-channels the results are similar.

and the difference between two empty measurements is plotted as remaining background noise. Note that only the spectra at the odd harmonic frequencies are plotted. In the lower frequency range, it isn't easy to see the difference between samples. However, from the 5th harmonic and on, the spectra of sample A and sample B quickly descend to the noise level. It is because of the larger size of the nanoparticles, which is 500 nm and 250 nm for sample A and sample B, respectively. See Section 2.1.1, the nanoparticles must be sufficiently small to behave the superparamagnetic characteristics. For sample C, it reaches the noise level at about 1.1 MHz, while for sample D at around 1.3 MHz. Sample C, with nanoparticles of 100 nm, has a higher magnitude than sample D. The result is in compliance with the principle stated in Section 2.1.2, which is a larger particle core leads to a higher magnetic moment [6] and therefore a higher magnitude spectrum.

6.2.3 Perimag

The impact of the temperature on the MNPs is not negligible. With the temperature control unit (see Section 5.3) implemented in the MPS, the temperature of the MNPs could be adjusted during the measurement.

Perimag with plain surface functionalities from micromod Partikeltechnologie (Rostock, Germany) was used to prepare a 10 µL sample. Perimag is a multi-core MNP with the hydrodynamic size of 130 nm, it showed a great performance to be used in MPI [83]. The drive field amplitudes and frequencies were the same as in the previous measurement. The temperature was set from 10 °C to 60 °C with a step of 10 °C at the temperature control unit. A fiber-optic probe, PRB-100 (Osensa Innovations, Burnaby, Canada), was used to measure the temperature of a water sample in the sample chamber, which is assumed to be equal to the particle sample. 1000 periods were measured for averaging with the particle sample as well as an empty measurement at each temperature.

The magnitude spectra of the particle sample with empty measurement subtraction are shown in Fig. 6.7, as well as the remaining background noise at each temperature. The remaining background noise shows no

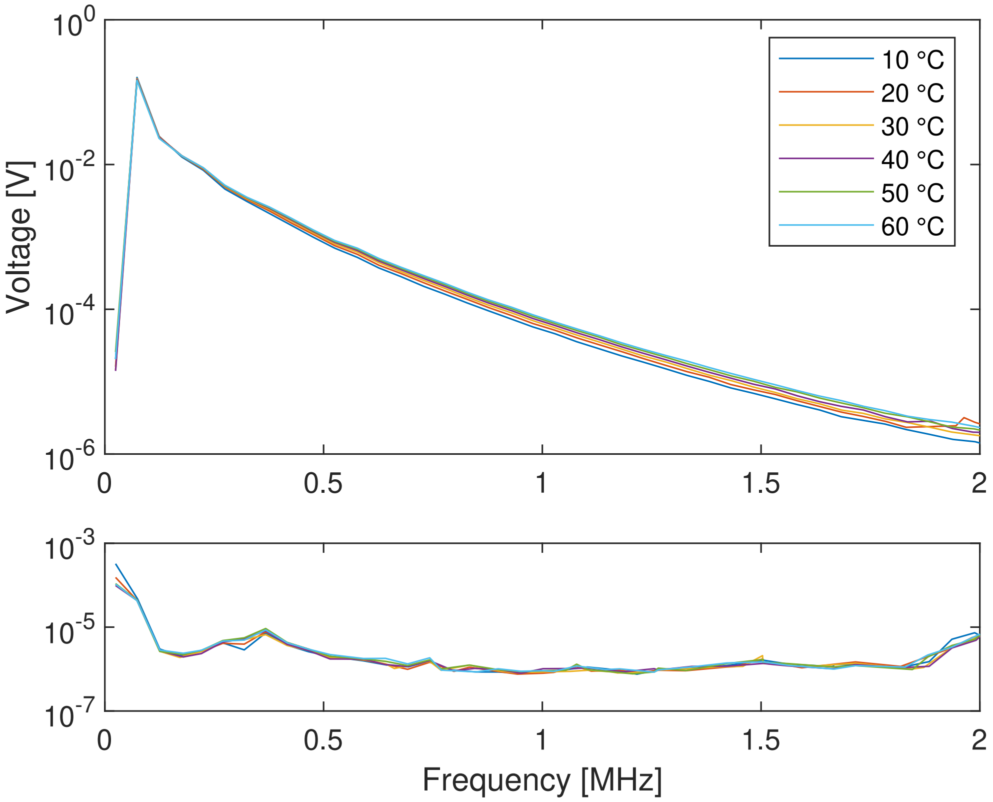

Figure 6.7: Magnitude spectra of the Perimag at different temperatures. From 10 °C to 60 °C, the sample is measured with a step of 10 °C. The magnitude spectra are plotted with empty measurement subtraction. The remaining background noise at each temperature is also plotted. Note that only the signals of the R_x-channel are shown here, while in the R_y- and R_z-channels the results are similar.

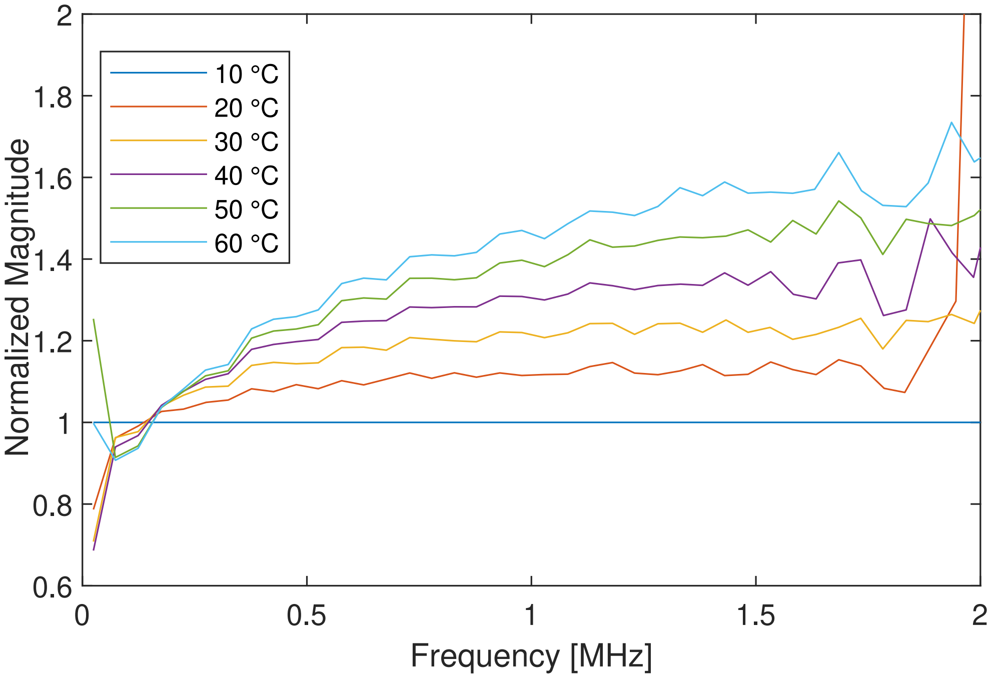

Figure 6.8: Normalized magnitude spectra of the Perimag at different temperatures. The magnitude spectra of the particle sample are normalized to the one at 10 °C. Note that only the signals of the R_x-channel are shown here, while in the R_y- and R_z-channels the results are similar.

distinguishable difference between each other at different temperatures. It means that the influence of the temperature changes on the receive coils is negligible, and it also proves that the thermal noise of the receive coils is not the dominant noise source in the receive chain. The sample spectra are measured till about 1.8 MHz before it drops down the noise level. However, the difference between each spectrum is difficult to distinguish on a logarithm scale. Therefore, in Fig. 6.8, the magnitude spectra of the particle sample are normalized to the one at 10 °C. From the 11th harmonics, which is about 270 kHz, the difference can be clearly distinguished. The spectra are higher in magnitude at a higher temperature. The observation is in agreement with the measurement in [52, 53, 84]. The magnitude ratio increases with the increase of the frequency until it reaches a plateau. The higher the temperature, the slower the ratio increases. Hence, the magnitude ratio and the temperature are not simply linear related. However, further experiments should be conducted to study the relationship between temperature and spectrum magnitude.

6.3 System Matrix

Besides measuring the particle samples, the newly developed 3D MPS was capable of recording SMs. For measuring the SM, DC sources were used to generate the offset fields, and the H-bridges were used to switch the polarities of the currents applied to the transmit coils.

6.3.1 1D System Matrix

A 10 µL Resovist sample was prepared for measurement. The temperature of the sample was stable at room temperature 22 °C. The drive field amplitudes were $12\,\mathrm{mT}/\mu_0$, and the frequencies were 24.51 kHz, 26.04 kHz, and 25.25 kHz, for the T_x-, T_y-, and T_z-channel, respectively. First, a 1D SM was recorded while the offset field varied with a step of 0.5 mT in the range $[-14, 14]\,\mathrm{mT}$ in the T_x-channel. It resulted in a 1D SM with grid size $57 \times 1 \times 1$. At each grid position, the sample was measured 10 times for averaging. Actually, during measurement, 11 periods were measured at each grid position. Considering the rising time of the output voltage step from the DC sources, the first period of measurement was not used for averaging. So, the total measurement time was about 13.5 s when ignoring the waiting time between each octant. In the operating program, a stop was made after finishing measuring each octant for safety reasons. Under the same condition, the 1D SMs were also recorded while varying the offset fields in the T_y-channel or T_z-channel. It resulted in one 1D SM with grid size $1 \times 57 \times 1$ and another with grid size $1 \times 1 \times 57$, respectively.

Fig. 6.9, Fig. 6.10, and Fig. 6.11 show the measurement results of the 1D SMs. Note that the measurement results are corrected by the transfer function. The magnitude spectrum values are used for plotting. At each odd harmonic frequency, the values at different grid positions are normalized to those at the center position, where the offset field is 0 mT. Fig. 6.9 shows that the SM has a symmetric pattern until about the 39th harmonic or 975.56 kHz. Fig. 6.10 shows the SM with a symmetric pattern until about 29th harmonic or 730.51 kHz. However, it clearly shows an influence of the resonance peaks above the 31st harmonic. Further investment should be conducted to examine the hardware in the y-channel. In Fig. 6.11, the SM shows a symmetric pattern until about 33rd harmonic or 829.25 kHz. The results verify the functionality of applying offset fields in all three channels.

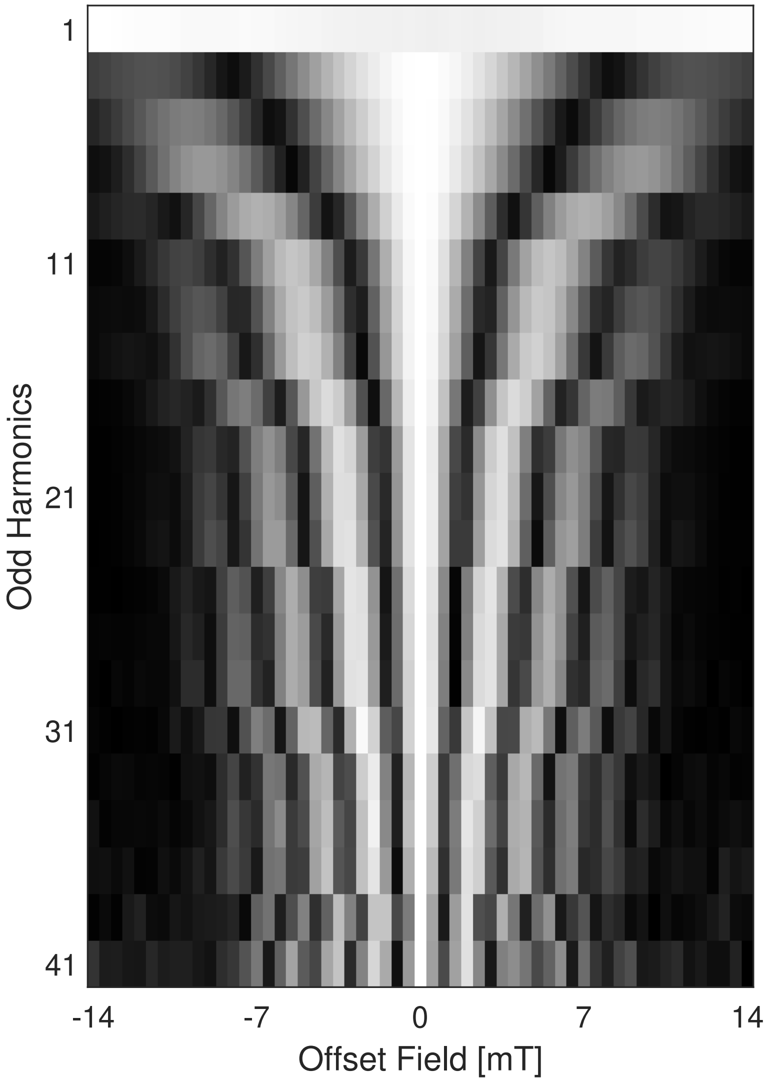

Figure 6.9: 1D SM with grid size $57 \times 1 \times 1$. The offset field varies with a step of $0.5\,\mathrm{mT}$ in range $[-14, 14]\,\mathrm{mT}$ in the T_x-channel. Note that only the received signals from the R_x-channel are shown. At each odd harmonic frequency, the magnitude spectrum values at different grid positions are normalized to the one at the center position, where the offset field is $0\,\mathrm{mT}$.

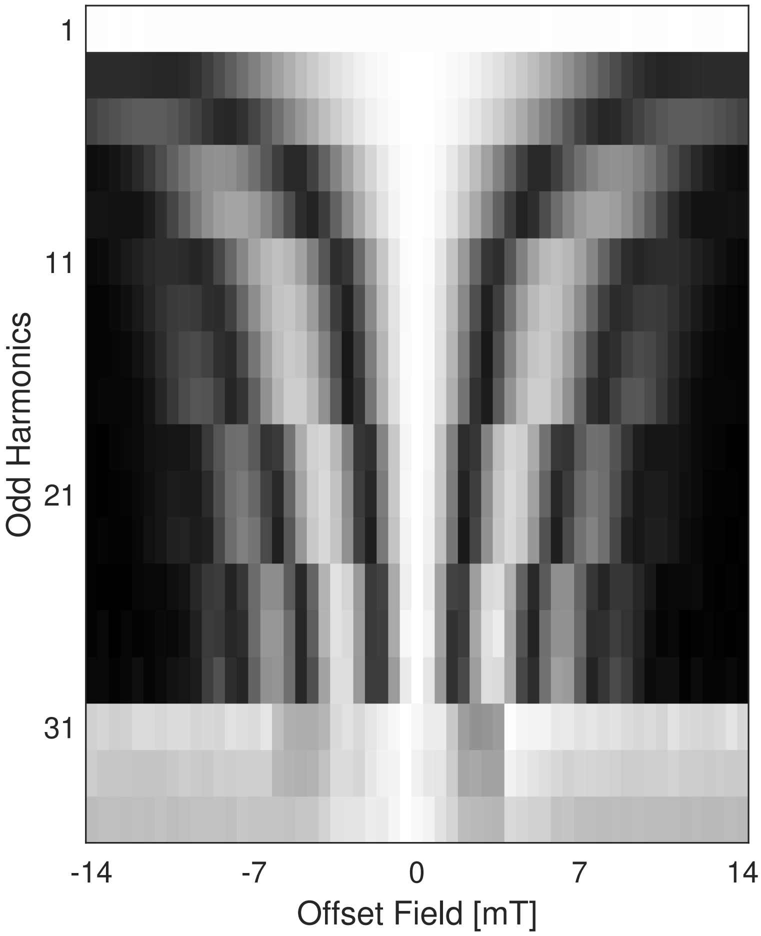

Figure 6.10: 1D SM with grid size $1 \times 57 \times 1$. The offset field varies with a step of $0.5\,\mathrm{mT}$ in range $[-14, 14]\,\mathrm{mT}$ in the T_y-channel. Note that only the received signals from the R_y-channel are shown. At each odd harmonic frequency, the magnitude spectrum values at different grid positions are normalized to the one at the center position, where the offset field is $0\,\mathrm{mT}$.

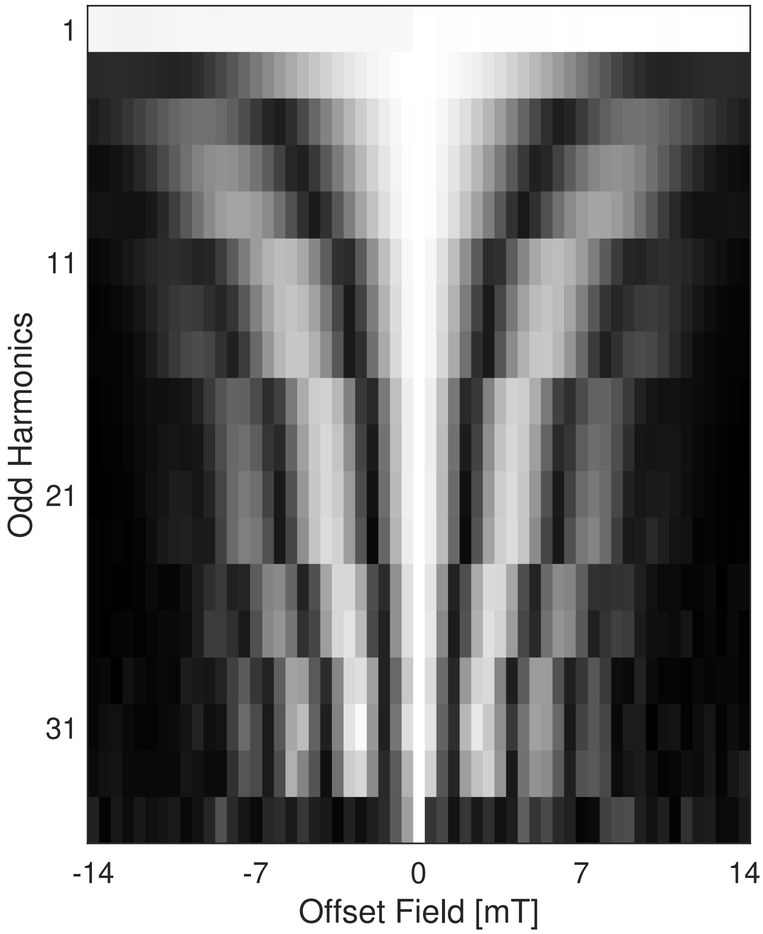

Figure 6.11: 1D SM with grid size $1 \times 1 \times 57$. The offset field varies with a step of $0.5\,\mathrm{mT}$ in range $[-14, 14]\,\mathrm{mT}$ in the T_z-channel. Note that only the received signals from the R_z-channel are shown. At each odd harmonic frequency, the magnitude spectrum values at different grid positions are normalized to the one at the center position, where the offset field is $0\,\mathrm{mT}$.

6.3.2 2D System Matrix

A 10 µL Resovist sample was used for measurement. The temperature of the sample was stable at room temperature 22 °C. The drive field amplitudes were $12\,\mathrm{mT}/\mu_0$, and the frequencies were 24.51 kHz, 26.04 kHz, and 25.25 kHz, for the T_x-, T_y-, and T_z-channel, respectively. The offset fields in range $[-14, 14]\,\mathrm{mT}$ varied with a step of 0.5 mT in both T_x-channel and T_y-channel. So, a 2D SM was recorded with grid size $57 \times 57 \times 1$. At each grid position, the sample was measured 11 times while 10 were used for averaging. Hence, the total measurement time was about 12.8 min when ignoring the waiting time between each octant. Fig. 6.12 shows the measured SM results. Note that the measurement results are corrected by the transfer function. The magnitude spectrum values are used to plot the SM. At each odd harmonic, the SM is normalized to the magnitude value at grid position $(29, 29, 1)$, where the offset field is 0 mT. Each row shows the SM at a different odd harmonic frequency. The columns show the SM measured from different receive channels. The exact frequency is shown on the top of each SM frame.

As seen from Fig. 6.12, a finer structure is clearly observed at higher frequencies. However, at a higher frequency, the structure of the SM faded at the grid position with higher offset fields. At the 1st harmonic, the receive signals were heavily filtered, so no pattern is shown. In the R_x-channel the symmetric structure of the SM can be seen till about 39th harmonics (978.63 khz), while in the R_y-channel 29th harmonics (730.51 kHz), and in the R_z-channel 33rd harmonic (829.25 kHz). The worse behavior in the y-channel has been explained in Section 6.3.1. It can be observed that in the R_x-channel the SM patterns are stretched in the horizontal direction, in which the offset field in the T_y-channel changes. For simplicity, the horizontal direction is named the y direction. Likewise, the vertical direction is named the x direction. As expected, in the R_y-channel the SM patterns are stretched in the x direction. In R_z-channel the SM is similar to that in the R_x-channel. The reason is the coupling of the signals from the x-channel is stronger than that from the y-channel while taking the geometries of the receive coils into consideration.

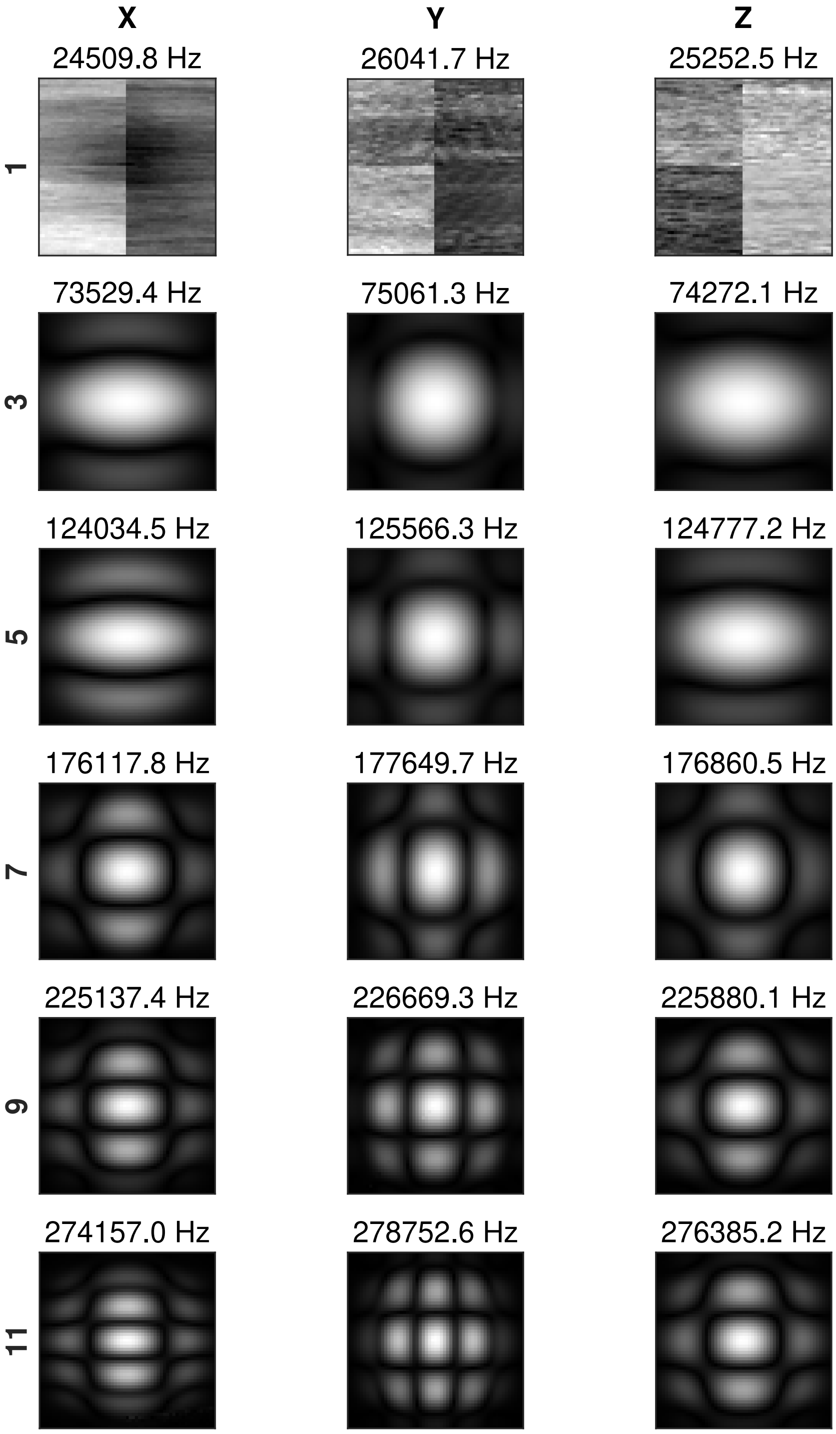

Figure 6.12: 2D SM with grid size $57 \times 57 \times 1$. The offset field is in range $[-14, 14]\,\mathrm{mT}$ with a step of $0.5\,\mathrm{mT}$. Each row shows a different odd harmonic, and the columns show the different receive channels.

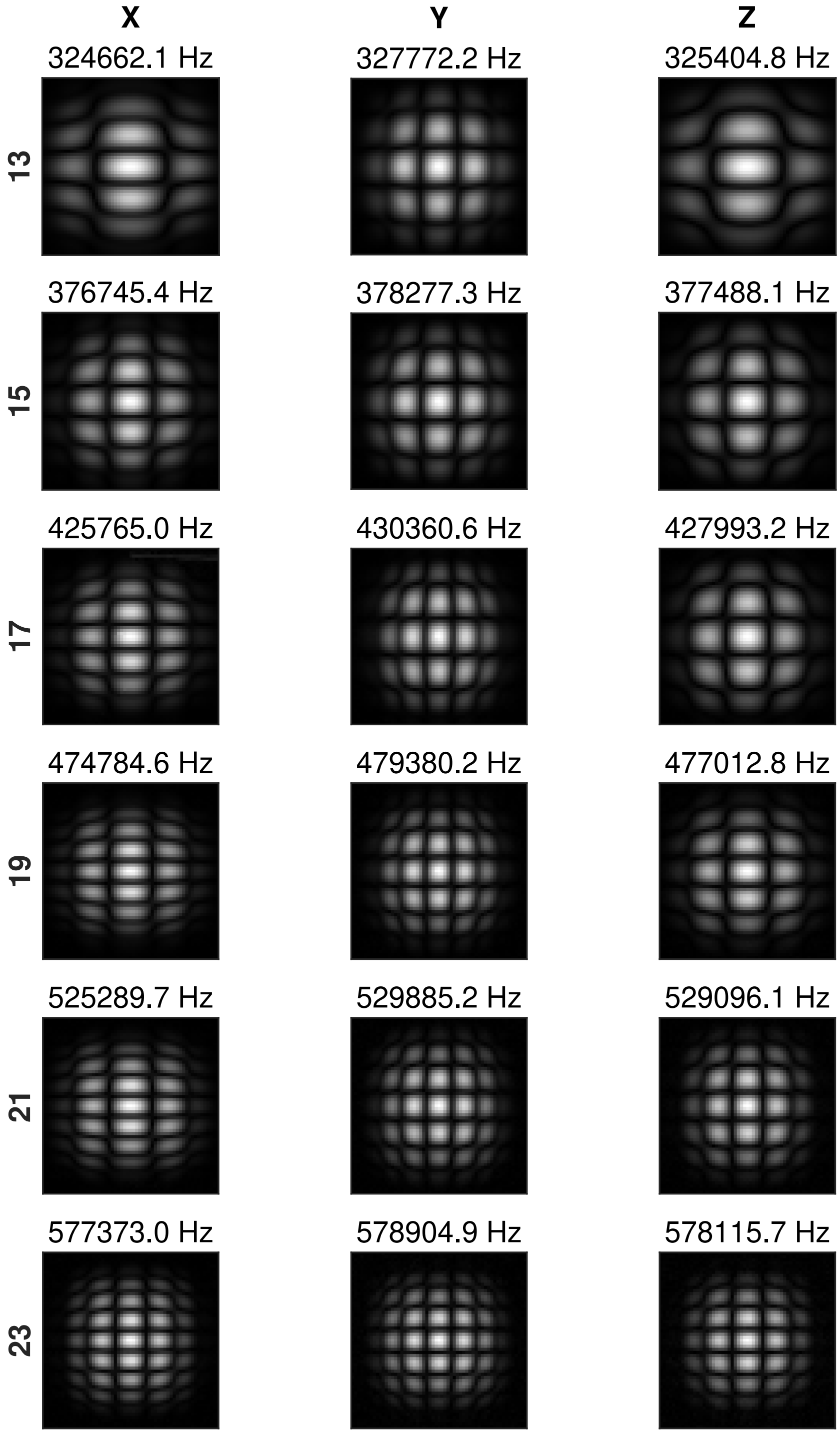

Figure 6.12 (cont.): 2D SM with grid size $57 \times 57 \times 1$.

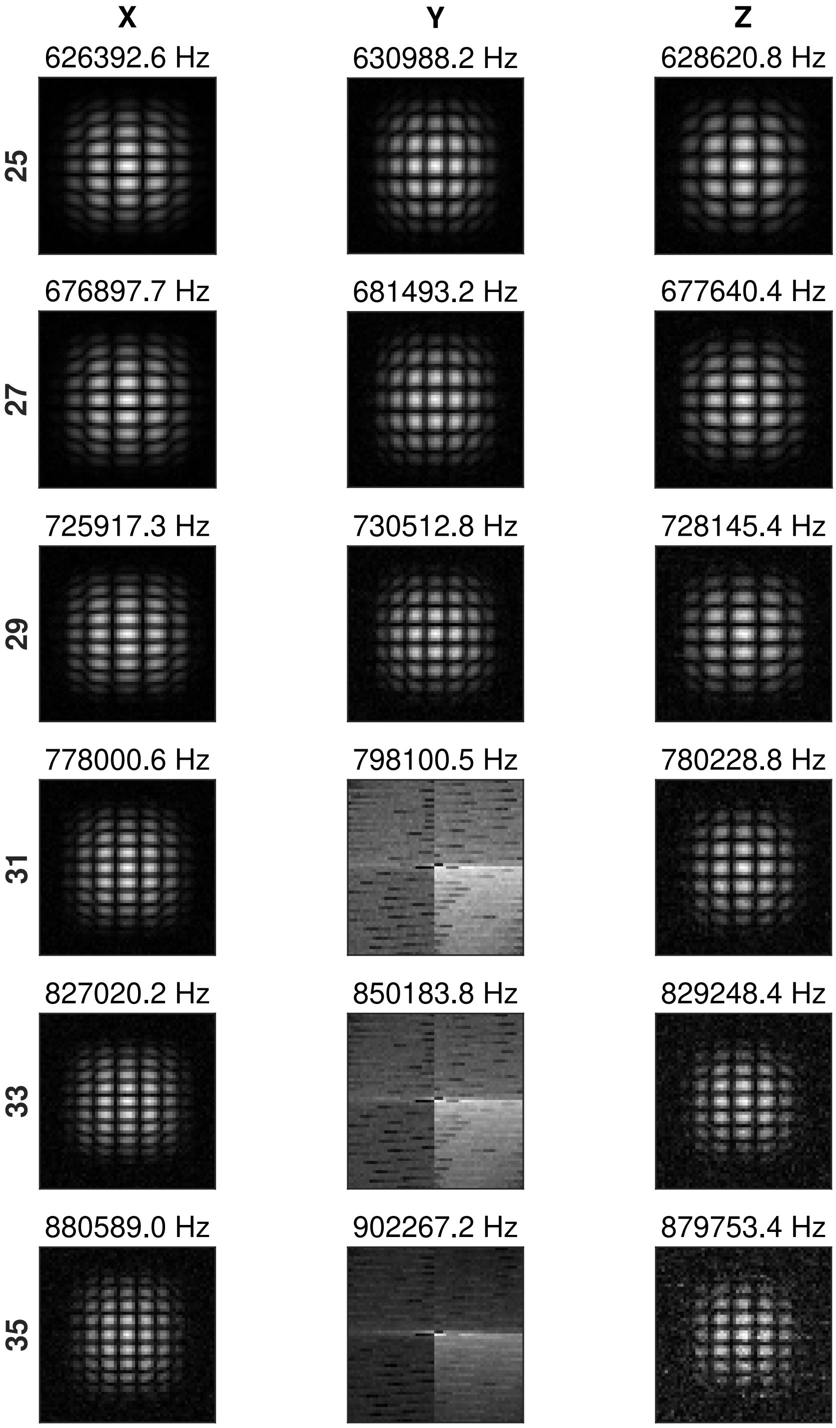

Figure 6.12 (cont.): 2D SM with grid size $57 \times 57 \times 1$.

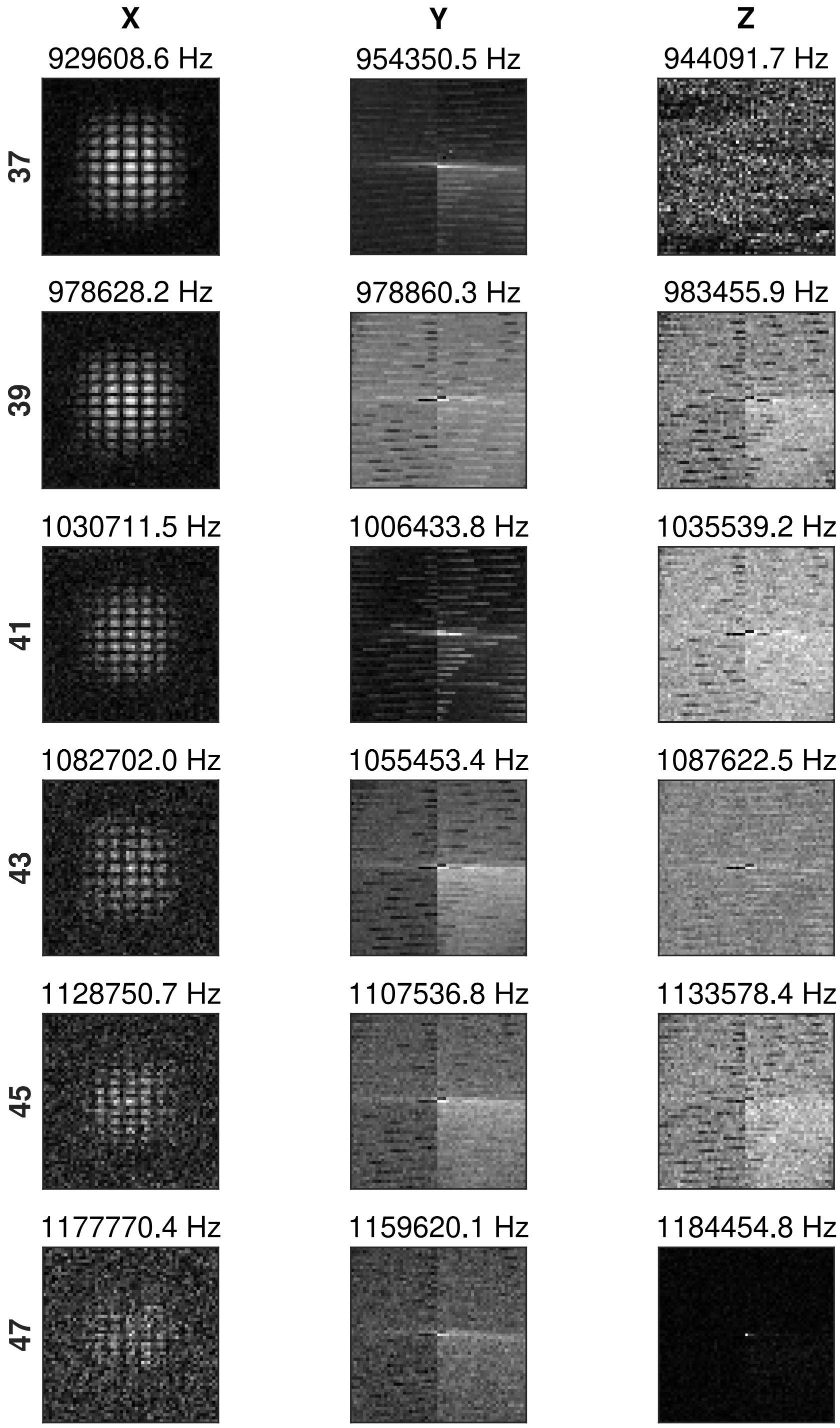

Figure 6.12 (cont.): 2D SM with grid size $57 \times 57 \times 1$.

6.3.3 3D System Matrix

A 10 µL Resovist sample was used for measurement. The temperature of the sample was stable at room temperature 22 °C. The drive field amplitudes were 12 mT/μ_0, and the frequencies were 24.51 kHz, 26.04 kHz, and 25.25 kHz, for the T_x-, T_y-, and T_z-channel, respectively. The offset fields in range $[-14, 14]$ mT varied with a step of 1 mT in the T_x-, T_y-, and T_z-channel. It resulted in a 3D SM with grid size $29 \times 29 \times 29$. At each grid position, the sample was measured 6 times while 5 were used for averaging. Hence, the total measurement time was about 52.5 min when ignoring the waiting time between each octant. Fig. 6.13 shows the measured SM results from the R_x-channel. Note that the measurement results are corrected by the transfer function. The magnitude spectrum values are used to plot the SM. At each odd harmonic, the SM is normalized to the magnitude value at grid position $(15, 15, 15)$, where the offset field is 0 mT. In Fig. 6.13, the 3D SM is sliced along the z direction, in which the offset field in the T_z-channel changes. Each row shows one slice in the z direction, and each column shows the SM frame at a different odd harmonic frequency. In each SM frame, the vertical direction is the x direction, while the horizontal direction is the y direction.

As observed in 2D SM, the structures of the SM faded at the grid position with higher offset fields. At slices 1 and 29, where the offset field is ±14 mT, the SM frames are already noisy at the 21st harmonic. While at slices 8 and 22, where the offset field is ±7 mT, the SM frames still show symmetric patterns. At slice 15, where the offset field is 0 mT, the results are in accord with the results shown in Fig. 6.12 (first column). Fig. 6.14 shows a 3D visualization of the SM. An online script [85] was used to help with the plotting. The SM is plotted at each odd harmonic. The structures of the SM are clearly visualized till the 35th harmonic or 877.5 kHz. With the increase of the frequency, the structure of the SM becomes finer. However, it shrinks towards the center.

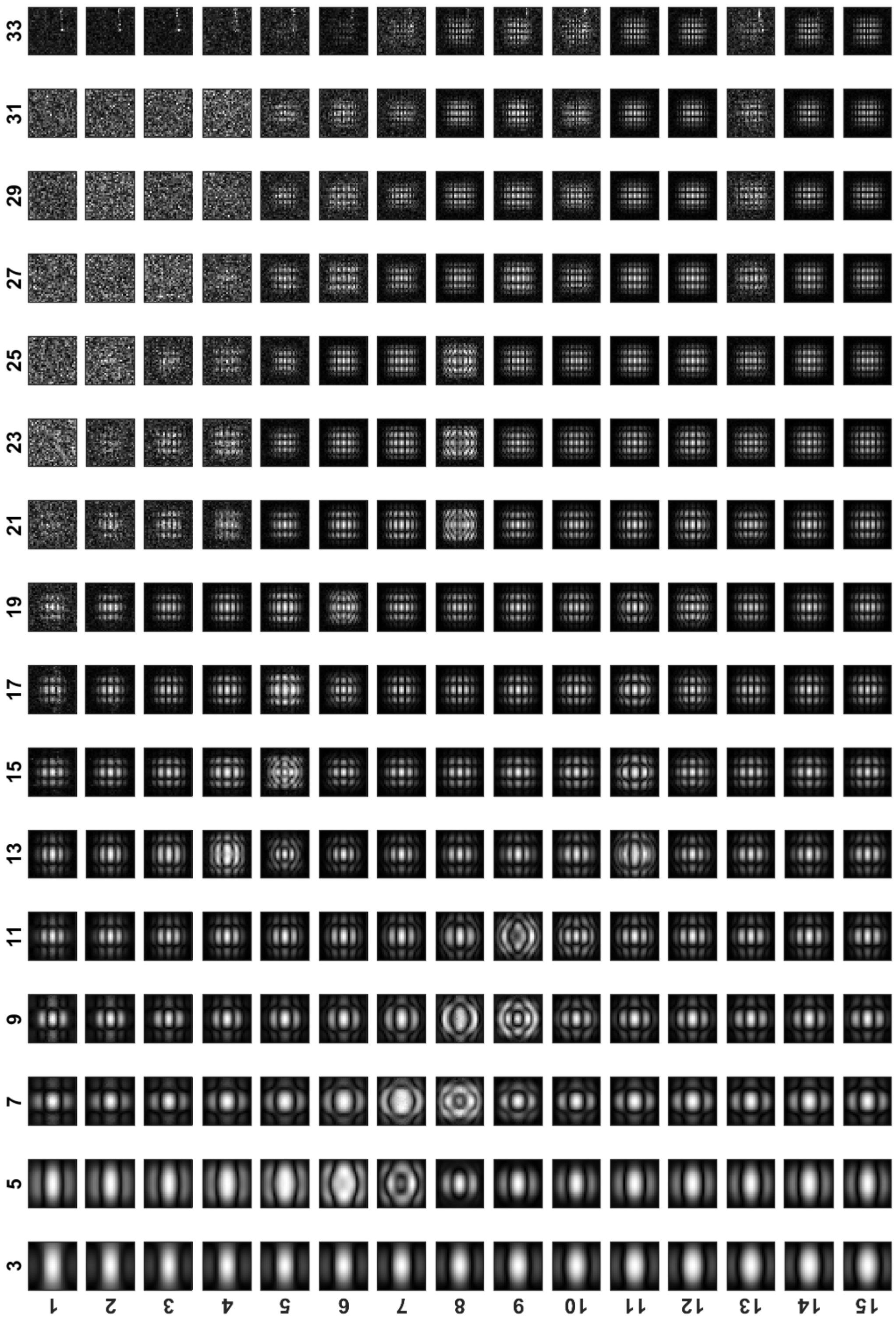
33
31
29
27
25
23
21
19
17
15
13
11
9
7
5
3
1
2
3
4
5
6
7
8
9
10
11
12
13
14
15

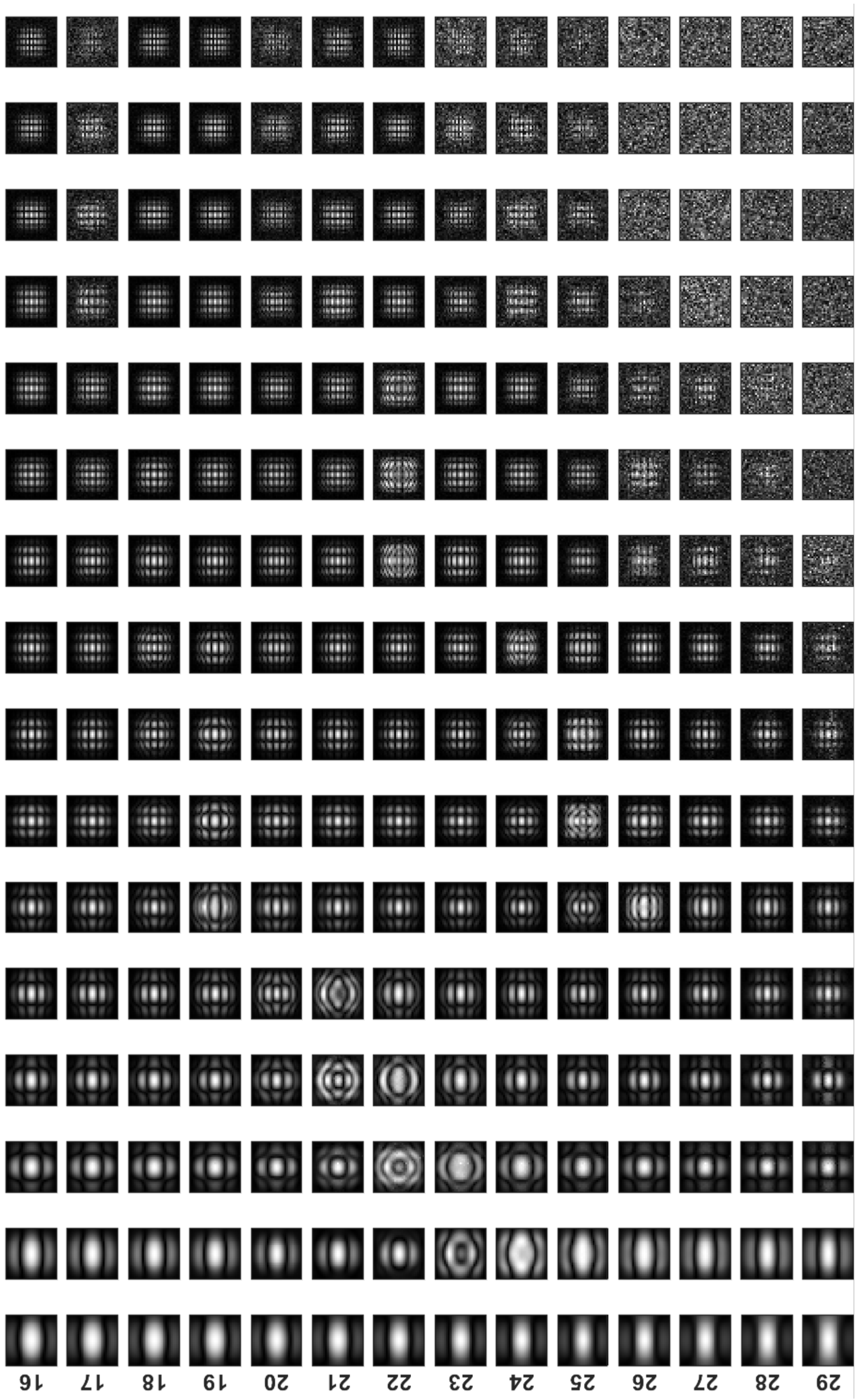

Figure 6.13: 3D SM (slice view). The grid size is $29 \times 29 \times 29$. The offset field is in range $[-14, 14]$ mT. Each row shows one slice in the z direction, and each column shows the SM frame at a different odd harmonic.

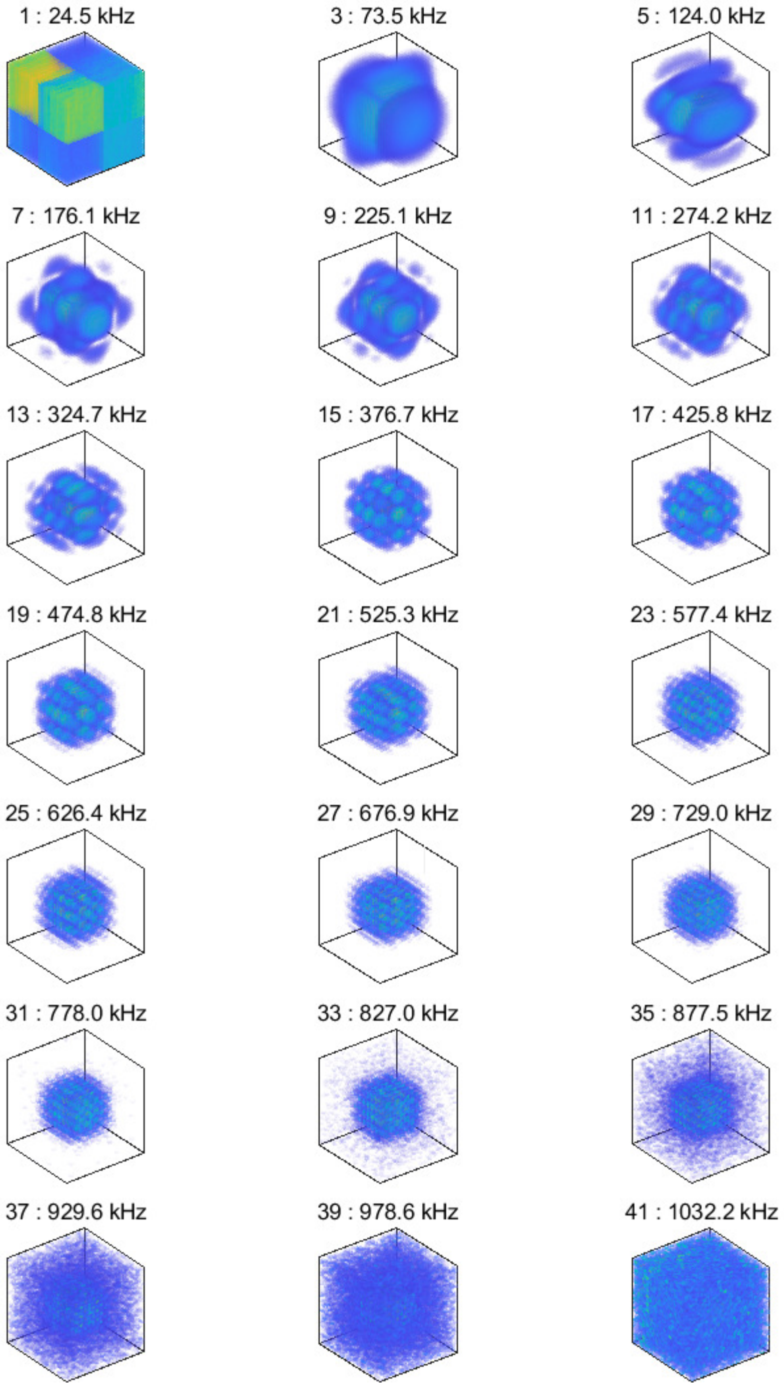

Figure 6.14: 3D SM (3D visualisation). The grid size is $29 \times 29 \times 29$. The offset field is in range $[-14, 14]\,\mathrm{mT}$. The SM is plotted at each odd harmonic.

CHAPTER 7

SUMMARY AND DISCUSSION

This thesis thoroughly describes the development of a 3D MPS. It can apply drive fields up to $20\,\mathrm{mT}/\mu_0$ and offset fields in the range of $[-20, 20]\,\mathrm{mT}$ in all three channels. The drive field frequencies are $24.51\,\mathrm{kHz}$, $26.04\,\mathrm{kHz}$, and $25.25\,\mathrm{kHz}$ for the x-, y-, and z-channel, respectively. Referring to the system diagram in Fig. 2.5, the MPS system consists of three parts, which are the transmit chain, the receive chain, and the control unit.

The main hardware of an MPS is the transmit coils. Derived from the Biot-Savart law, the magnetic fields produced by a circular loop, a rectangular loop, a quasi-rectangular loop, a quasi-circular loop, a curved rectangular loop, and a curved circular loop were expressed numerically. A coil was considered a combination of multiple wire loops of the same geometry. A self-developed program was used to optimize the size of the coils regarding the powerloss and field homogeneity. For a 3D coil setup, the combinations of different shapes of coils in all channels were optimized as a whole. The result showed that an optimized coil setup with a circular T_x-coil, a pair of quasi-rectangular T_y-coils, and a pair of curved rectangular T_z-coils (see Fig. 3.14). If the T_y-coils were changed from quasi-rectangular shape to curved rectangular shape, the total powerloss would increase slightly. However, the larger surface area would benefit the cooling, and it is easier to fabricate. Hence, in the future, it could be taken into consideration to choose the curved rectangular shape for both T_y-coils and T_z-coils. In order to drive the transmit coils, the impedance of the coils was matched by an impedance matching network to the power amplifier. The power amplifier was a self-built class-AB amplifier with commercially available components. In the impedance matching network, the used capacitors were carefully calculated, selected, and tuned. It was a time-consuming process, but one possible method to improve is to use variable capacitors in the tuning process. Additionally, the variable capacitors make the maintenance process easier when the capacitance of the capacitors drifts with time. BPFs were used to purify the amplified signals from the power amplifier by removing the higher harmonics. Third-order LC BPFs were designed and simulated. Tunable air core inductors were designed since the BPFs needed to be precisely tuned at the specific frequencies. Although the impedance of the transmit coils was matched to the power amplifier, with the combination of the BPFs in the circuit, the impedance changed dramatically when the frequency drifted (see Fig. 3.27). A safe range was about a few hundred Hz. Under some extreme conditions, this may bring hazards to the system, e.g., overheating of the power amplifier. However, such a situation has never happened during the operation of the MPS. One possible way to improve is to use different impedance matching methods. For instance, instead of the currently implemented L network, a T or Pi network can be used. The advantage is that the quality factor of the matching network can then be adjusted. However, more research needs to be conducted. In order to generate the offset fields, DC sources were used to apply current to the transmit coils, and the H-bridges were used to switch the direction of the currents.

To achieve high SNR, the receive coils were placed as close as possible to the nanoparticle sample. Since they were not the dominant noise source in the receive chain, the maximum number of windings was used to wind the receive coils according to the space limitation. Special coil formers were designed to hold the coils in position. To further improve the sensitivity of the receive coils, the design of the coil former can be modified to fit more windings. Because the excitation signal from the transmit coils can directly couple into the receive coils, which is several orders higher than the received particle signals. In this work, a combination of the filter method and the cancellation method was used. From the cancellation method, an attenuation value of about 25–45 dB (see Table 4.2) was reached. However, it is lower than expected, especially in the R_x-channel. Although it is difficult to build two identical coils, more effort can be put into the construction of the coils. Since the R_x-coil is a circular solenoid, another possible method is to design a gradiometer coil in the R_x-channel. To further reduce the coupled excitation signals, second-order BSFs were built. Hence, the total attenuation reached about 90 dB. At the end of the receive chain, LNAs were used to amplify the received signals to match the dynamic range of the DAQ cards in the PC.

In the control unit, multiple DAQ cards were used (see Fig. 5.1). For monitoring the currents flowing in the transmit coils, Rogowski coils were built as feedback components. Since the impact of the temperature on the nanoparticles was not negligible, a temperature control unit was dedicatedly designed to maintain and adjust the temperature in the sample chamber. Two pipes with different diameters were placed concentrically, and the circulating water between the pipes dissipated the heat into the sample chamber to establish a thermal equilibrium. Additionally, the water prevented the heat from the transmit coils from influencing the sample chamber. The temperature of the circulating water was able to be changed from 10 °C to 60 °C with a deviation of 0.2–0.5 °C. However, only the sensor monitoring the circulating water was read by the microcontroller (see Fig. 5.6). The reading of the fiber-optic sensor monitoring the sample chamber should be implemented in the temperature control codes to improve the control loop. To increase the speed of reaching the thermal equilibrium, as well as the stability of the temperature, a PID control should be implemented in the program. The opto-isolator circuitries were built to control the H-bridges and the DC sources safely and precisely. Power supplies were used to supply different components in the MPS system.

Before performing the measurement, calibration was conducted with the help of the calibration coils. For the transmit chain, the drive field and offset field were calibrated so that the magnetic fields could be generated with accuracy. For the receive chain, the transfer function was recorded so that the measured voltage signals could then be transferred to the magnetic moment of the nanoparticles. The Resovist was measured since it was used as a "good standard" nanoparticle in MPI. 10 µL undiluted Resovist excited by $20\,\mathrm{mT}/\mu_0$ drive field exhibited 81st harmonics (about 2.0 MHz), 71st harmonics (about 1.9 MHz), and 69st harmonics (about 1.7 MHz) in the R_x-, R_y-, and R_z-channel, respectively. It could be observed that there is a resonance peak at about 2 MHz in the R_y-channel, further inspection should be conducted to find out the causes. Additionally, SNR results were also plotted to show the high SNR of the 3D MPS. Nanomag samples with different diameters were measured for comparison. The results showed that the MNPs need to be sufficiently small to behave the superparamagnetic characteristic, and a larger particle core led to a higher magnitude spectrum. Perimag samples were measured with different temperature from 10 °C to 60 °C with a step of 10 °C. The normalized magnitude showed a clear difference at higher frequencies. The magnitude ratio increased with the increase of the frequency until it reached a plateau. The relationship between the spectrum magnitude and the temperature was not linear, since the spectrum increased slower at higher temperatures. However, further experiments should be conducted to study. The measurement results show that the 3D MPS is capable of measuring nanoparticle samples with high sensitivity at different temperatures. Another usage of the 3D MPS is to record the hybrid SM. Three 1D SMs were measured with offset fields varying in the T_x-, T_y-, and T_z-channel, respectively. The results verify the functionality of applying offset fields in all three channels. But the worse behavior in the y-channel than in the z-channel indicates that the signals in the y-channel could be further improved after solving the resonance issues. 2D and 3D SMs showed a finer structure at higher frequencies, however, the structure also shrank, i.e., the structure faded at the edges and corners of the SMs, where the grid position with higher offset fields. The results verify the ability of the 3D MPS to measure SMs.

This thesis presents the development of a 3D MPS in detail, and the measurement results verify its ability to measure the spectrum of the nanoparticles and record the SM. The improvements mentioned above could be made in the future to increase the performance of the MPS. It could be a useful tool to help with the research study in MPI.

APPENDIX A

CALCULATION OF TWO WIRE PATHS

A.1 Arc Wire

As shown in Fig. A.1, an arc wire path lying in the x-y plane subtends an angle π at the origin O. The vector $\boldsymbol{\ell}$ from O to the wire element on the arc path is written as

$$\boldsymbol{\ell} = (R\cos\theta, R\sin\theta, 0)\,,$$

where R is the radius of the arc, θ is the angle between the vector $\boldsymbol{\ell}$ and the x-axis. Thus, an infinitely small increment of the wire element is

$$\mathrm{d}\boldsymbol{\ell} = (-R\sin\theta, R\cos\theta, 0)\,\mathrm{d}\theta\,,$$

The magnetic field is calculated at the point P on the y-z plane, the vector $\mathbf{r}_\mathrm{p}$ from O to P is given as $\mathbf{r}_\mathrm{p} = (0, y, z)$. The displacement vector $\mathbf{r}$ from the wire element to P is

$$\mathbf{r} = \mathbf{r}_\mathrm{p} - \boldsymbol{\ell} = (-R\cos\theta, y - R\sin\theta, z)\,,$$

with a magnitude of

$$|\mathbf{r}| = \sqrt{R^2 + y^2 + z^2 - 2Ry\sin\theta}\,, \tag{A.1}$$

The vector product $\mathrm{d}\boldsymbol{\ell} \times \mathbf{r}$ is written as

$$\mathrm{d}\ell \times \mathbf{r} = \begin{vmatrix} \hat{\mathbf{i}} & \hat{\mathbf{j}} & \hat{\mathbf{k}} \\ -R\sin\theta\,\mathrm{d}\theta & R\cos\theta\,\mathrm{d}\theta & 0 \\ -R\cos\theta & y - R\sin\theta & z \end{vmatrix}$$

$$= (Rz\cos\theta, Rz\sin\theta, R^2 - Ry\sin\theta)\,\mathrm{d}\theta\,, \tag{A.2}$$

where $\hat{\mathbf{i}}$, $\hat{\mathbf{j}}$, and $\hat{\mathbf{k}}$ are the standard unit vectors in x-, y-, and z-axis directions. Substituting Eq. (A.1) and Eq. (A.2) into Eq. (3.2), the contribution of the current I in the arc wire path to the magnetic field at P is written as

$$\mathbf{B}(P) = \frac{\mu_0 IR}{4\pi}\int_0^{\pi} \frac{z\cos\theta\hat{\mathbf{i}} + z\sin\theta\hat{\mathbf{j}} + (R - y\sin\theta)\hat{\mathbf{k}}}{(R^2 + y^2 + z^2 - 2Ry\sin\theta)^{3/2}}\,\mathrm{d}\theta\,. \tag{A.3}$$

Thus, the y-component of $\mathbf{B}$ can be derived as

$$B_y = \frac{\mu_0 IRz}{4\pi} \int_0^{\pi} \frac{\sin\theta}{(R^2 + y^2 + z^2 - 2Ry\sin\theta)^{3/2}} \, d\theta \,, \tag{A.4}$$

which involves elliptic integrals and can be evaluated numerically.

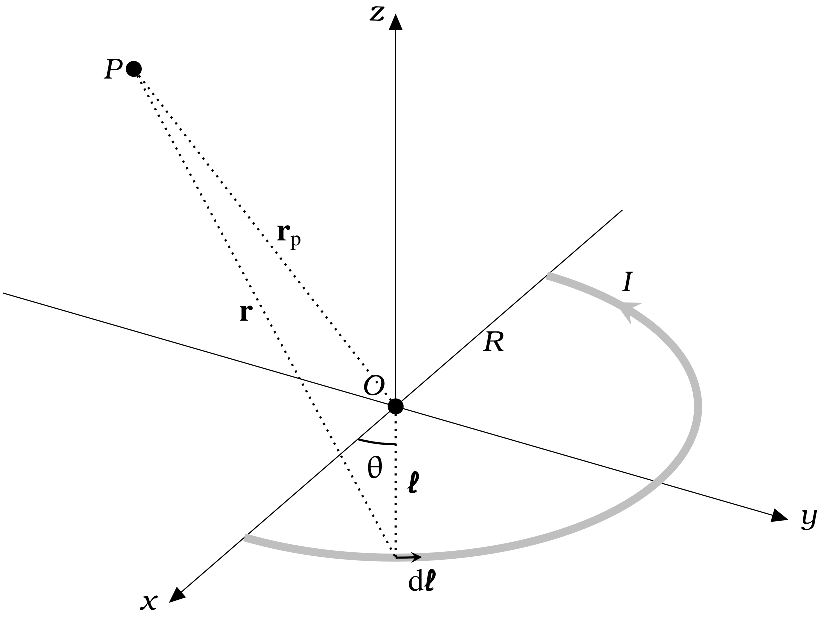

Figure A.1: Geometry of an arc wire path. I is the current flowing in the wire; R is the radius of the arc; $\mathbf{r}_p$ is the vector from the origin O to the point P on the y-z plane, where the magnetic field is evaluated; $\boldsymbol{\ell}$ is the vector from O to the wire element on the wire; θ is the angle between the vector $\boldsymbol{\ell}$ and the x-axis; $\mathbf{r}$ is the displacement vector from the wire element to P.

A.2 Finite Straight Wire

As shown in Fig. A.2, the magnitude of the magnetic field created at the point P by a finite straight wire path from point M to point N is

$$B = \frac{\mu_0 I}{4\pi r}(\cos\alpha + \cos\beta) \,, \tag{A.5}$$

where α is the angle between $\overline{MP}$ and the wire path $\overline{MN}$, β is the angle between $\overline{NP}$ and $\overline{MN}$, k is the perpendicular distance from P to $\overline{MN}$. Here, the direction of B points out of the paper. Note that angles α and β are positive numbers only. If the point P locates on the perpendicular bisector of the wire, namely $\alpha = \beta$, and let $2L$ be the length of the wire, Eq. (A.5) can be written as

$$B = \frac{\mu_0 I \cos\alpha}{2\pi k} = \frac{\mu_0 I}{2\pi k} \cdot \frac{L}{\sqrt{L^2 + k^2}}. \tag{A.6}$$

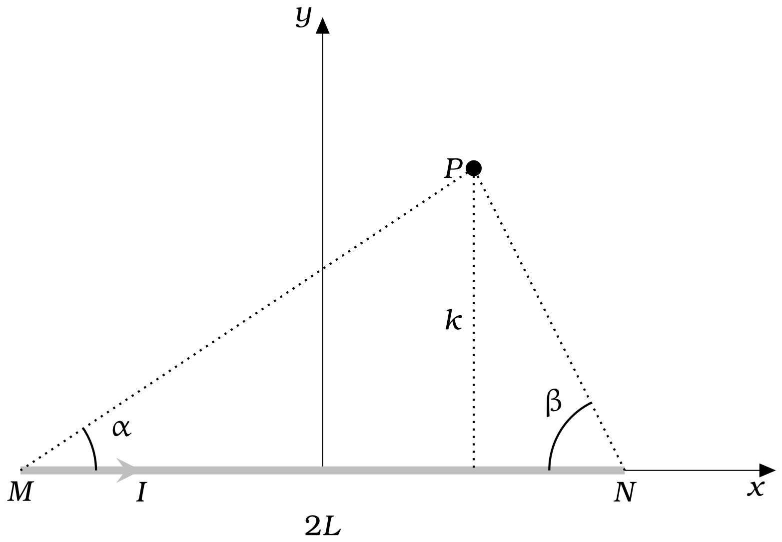

Figure A.2: Geometry of a finite straight wire path. I is the current flowing in the wire; $2L$ is the length of the wire; the points M and N are the endpoints of the wire; P is the point where the magnetic field is evaluated; α is the angle between $\overline{MP}$ and the wire path $\overline{MN}$; β is the angle between $\overline{NP}$ and $\overline{MN}$; k is the perpendicular distance from P to $\overline{MN}$.

APPENDIX B

TEMPERATURE CONTROL CODES

```
//this is main part of the Arduino codes used to
//control the temperature of circulating water

float Ts;          // setting temperature
float Tw;          // water temperature
...

//define the heating states
void heating(int state){
  digitalWrite(pinPtElementC1,HIGH);
  digitalWrite(pinPtElementC2,HIGH);
  switch (state){
    case 0:        // heating off
      digitalWrite(pinPtElementH1,HIGH);
      digitalWrite(pinPtElementH2,HIGH);
      break;
    case 1:        // heating with two Peltier elements
      digitalWrite(pinPtElementH1,LOW);
      digitalWrite(pinPtElementH2,HIGH);
      break;
    case 2:        // heating with four Peltier elements
      digitalWrite(pinPtElementH1,LOW);
      digitalWrite(pinPtElementH2,LOW);
      break;
  }
}

//define the cooling states
void cooling(int state){
  digitalWrite(pinPtElementH1,HIGH);
  digitalWrite(pinPtElementH2,HIGH);
  switch (state){
    case 0:        // cooling off
      digitalWrite(pinPtElementC1,HIGH);
      digitalWrite(pinPtElementC2,HIGH);
      break;
    case 1:        // cooling with two Peltier elements
      digitalWrite(pinPtElementC1,LOW);
      digitalWrite(pinPtElementC2,LOW);
      break;
    case 2:        // cooling with four Peltier elements
```

```
      digitalWrite(pinPtElementC1,LOW);
      digitalWrite(pinPtElementC2,LOW);
      break;
  }
}

//define the pump states
void circulation(int state){
  switch (state){
    case 0:        // off
      digitalWrite(pinPump,HIGH);
      break;
    case 1:        // on
      digitalWrite(pinPump,LOW);
      break;
  }
}

//define the fan states
void fan(int state) {
  switch (state){
    case 0:        // off
      digitalWrite(pinFan,HIGH);
      break;
    case 1:        // on
      digitalWrite(pinFan,LOW);
      break;
  }
}

...

void loop(void)
{
  ...
  if (systemrunnung) {
      // heating function on
      if (Ts>Tw+1 and heatstate==0){
          if(Ts-Tw>=5){
             heating(2);
          }
          else{
```

```
             heating(1);
          }
          heatstate=1;
          preservestate=0;
      }
      // hysteresis state with only pump and fans on
      if (Ts<=Tw+1 and Ts>=Tw-1 and preservestate==0){
          heatstate=0;
          coolstate=0;
          preservestate=1;
          heating(0);
          cooling(0);
      }
      // cooling function on
      if (Ts<Tw-1 and coolstate==0){
          if(Ts-Tw<=5){
             cooling(2);
          }
          else{
             cooling(1);
          }
          coolstate=1;
          preservestate=0;
       }
    }
}  // loop end
```

APPENDIX C

OPTO-ISOLATOR CIRCUIT DIAGRAMS

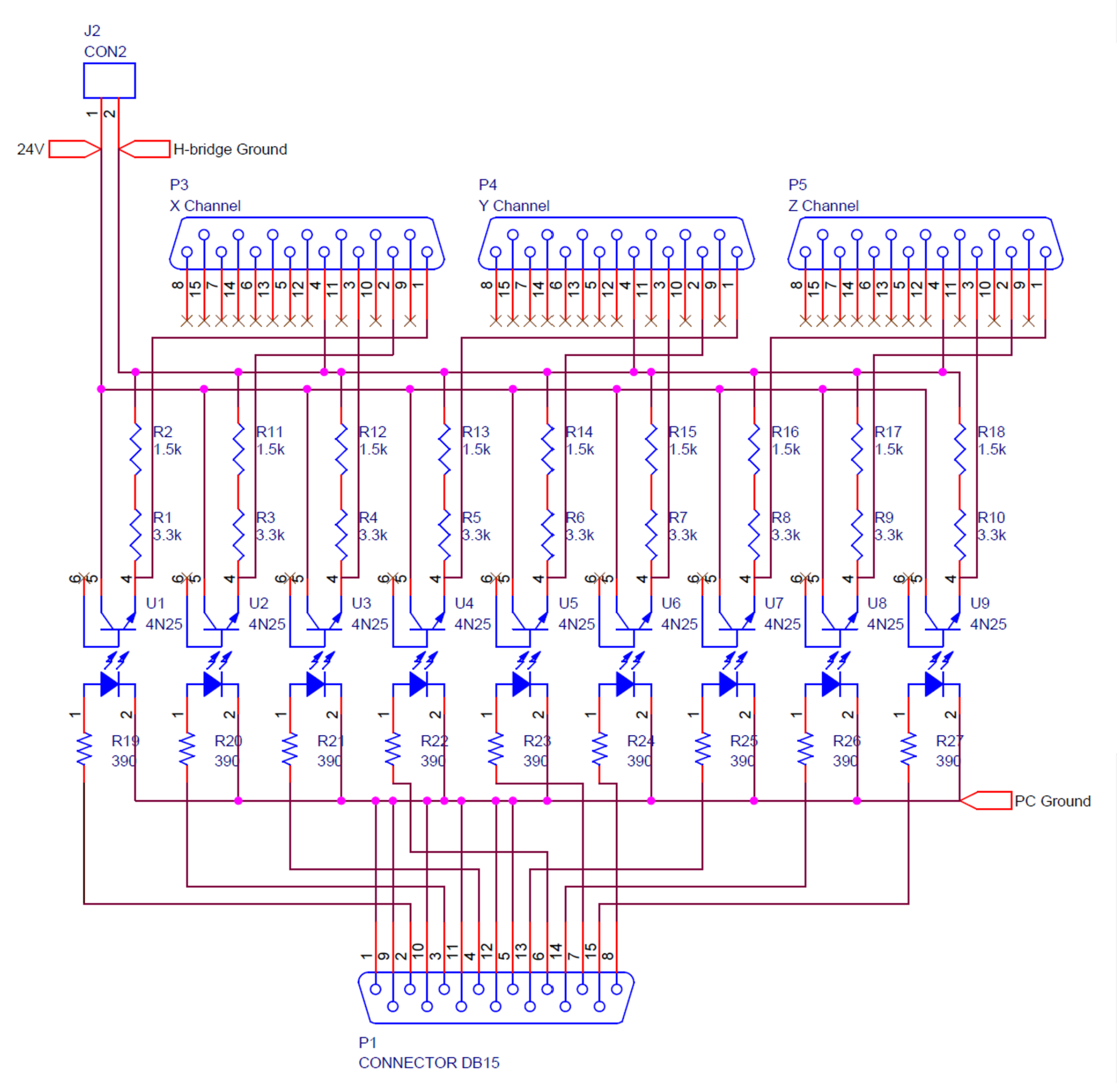

Figure C.1: Schematic of the opto-isolator for the H-bridges. Input and outputs are all 15-pin DB connectors. In the input port, pin 2, 3, and 4 are used to control the H-bridge in T_x-channel; pin 6, 7, and 8 are used to control the H-bridge in T_y-channel; pin 13, 14, and 15 are used to control the H-bridge in z-channel; other pins are connected to the PC ground via the breakout board of the DAQ card. The circuitry is built in a chassis shown in Fig. 2.6(b).

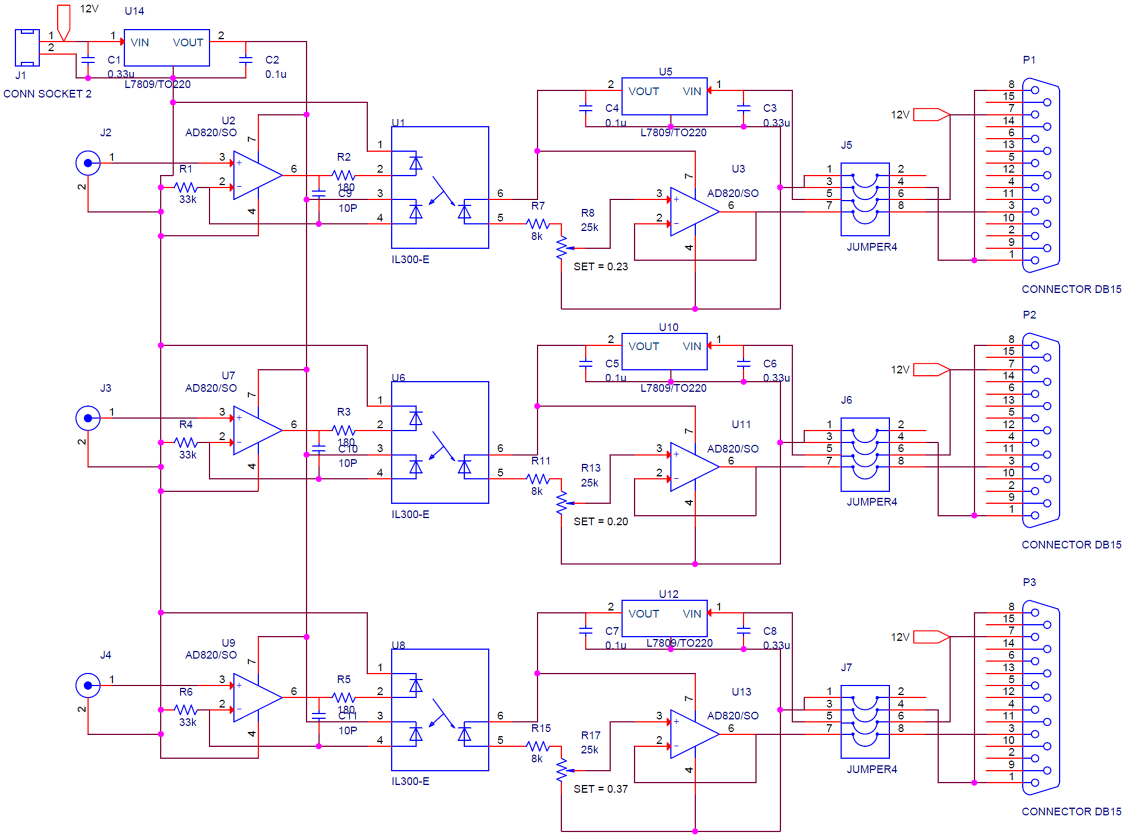

Figure C.2: Schematic of the opto-isolator for the DC sources. The input ports are three SMA connectors, and the output ports are three 15-pin DB connectors. Since the output current range of the DC sources is much larger than the demand, the variable resistors are adjusted to change the output voltage levels. The maximum output current of the DC sources is adjusted to 25 A. The circuitry is built in a chassis shown in Fig. 2.6(b).

BIBLIOGRAPHY

1. Gleich, B. *German Patent No.* DE10151778A1. https://patents.google.com/patent/DE10151778A1(2001).
2. Gleich, B. & Weizenecker, J. Tomographic imaging using the nonlinear response of magnetic particles. *Nature* **435,** 1214–1217. doi:10.1038/nature03808 (2005).
3. Wang, Y. X. Superparamagnetic iron oxide based MRI contrast agents: Current status of clinical application. *Quantitative Imaging in Medicine and Surgery* **1,** 35–40. doi:10.3978/j.issn.2223-4292.2011.08.03 (2011).
4. Billings, C., Langley, M., Warrington, G., Mashali, F. & Johnson, J. A. Magnetic particle imaging: Current and future applications, magnetic nanoparticle synthesis methods and safety measures. *International Journal of Molecular Sciences* **22,** 7651. doi:10.3390/ijms22147651 (2021).
5. Goodwill, P. W. *et al.* Ferrohydrodynamic relaxometry for magnetic particle imaging. *Applied Physics Letters* **98,** 262502. doi:10.1063/1.3604009 (2011).
6. Panagiotopoulos, N. *et al.* Magnetic particle imaging: Current developments and future directions. *International Journal of Nanomedicine* **10,** 3097. doi:10.2147/IJN.S70488 (2015).

7. Weizenecker, J., Gleich, B., Rahmer, J., Dahnke, H. & Borgert, J. Three-dimensional real-time *in vivo* magnetic particle imaging. *Physics in Medicine and Biology* **54,** L1–L10. doi:10.1088/0031-9155/54/5/l01 (2009).
8. Schmale, I., Gleich, B., Mende, O. & Borgert, J. *On the design of human-size MPI drive-field generators using RF Litz wires* in *2015 5th International Workshop on Magnetic Particle Imaging* (IEEE, 2015), 1–1. ISBN: 978-1-4799-7271-5. doi:10.1109/IWMPI.2015.7107071.
9. Graeser, M. *et al.* Human-sized magnetic particle imaging for brain applications. *Nature Communications* **10,** 1–9. doi:10.1038/s41467-019-09704-x (2019).
10. Weaver, J. B., Rauwerdink, A. M., Sullivan, C. R. & Baker, I. Frequency distribution of the nanoparticle magnetization in the presence of a static as well as a harmonic magnetic field. *Medical Physics* **35,** 1988–1994. doi:10.1118/1.2903449 (2008).
11. Biederer, S. *et al. A spectrometer for magnetic particle imaging* in *4th European Conference of the International Federation for Medical and Biological Engineering* (eds Vander Sloten, J., Verdonck, P., Nyssen, M. & Haueisen, J.) **22** (Springer, Berlin, Heidelberg, 2009), 2313–2316. ISBN: 978-3-540-89208-3. doi:10.1007/978-3-540-89208-3_555.
12. Wawrzik, T., Ludwig, F. & Schilling, M. Multivariate magnetic particle spectroscopy for magnetic nanoparticle characterization. *AIP Conference Proceedings* **1311,** 267–270. doi:10.1063/1.3530024 (2010).
13. Biederer, S. *et al.* Magnetization response spectroscopy of superparamagnetic nanoparticles for magnetic particle imaging. *Journal of Physics D: Applied Physics* **42,** 205007. doi:10.1088/0022-3727/42/20/205007 (2009).
14. Weaver, J. B., Rauwerdink, A. M. & Hansen, E. W. Magnetic nanoparticle temperature estimation. *Medical Physics* **36,** 1822–1829. doi:10.1118/1.3106342 (2009).
15. Rauwerdink, A. M. & Weaver, J. B. Measurement of molecular binding using the Brownian motion of magnetic nanoparticle probes. *Applied Physics Letters* **96,** 033702. doi:10.1063/1.3291063 (2010).

16. Rauwerdink, A. M. & Weaver, J. B. Viscous effects on nanoparticle magnetization harmonics. *Journal of Magnetism and Magnetic Materials* **322,** 609–613. doi:10.1016/J.JMMM.2009.10.024 (2010).
17. Zhang, X. *et al.* Molecular sensing with magnetic nanoparticles using magnetic spectroscopy of nanoparticle Brownian motion. *Biosensors and Bioelectronics* **50,** 441–446. doi:10.1016/j.bios.2013.06.049 (2013).
18. Wu, K. *et al.* Magnetic particle spectroscopy for detection of influenza a virus subtype H1N1. *ACS Applied Materials & Interfaces* **12,** 13686–13697. doi:10.1021/acsami.0c00815 (2020).
19. Loewa, N. *et al.* Cellular uptake of magnetic nanoparticles quantified by magnetic particle spectroscopy. *IEEE Transactions on Magnetics* **49,** 275–278. doi:10.1109/TMAG.2012.2218223 (2013).
20. Gräfe, C. *et al.* Magnetic particle spectroscopy allows precise quantification of nanoparticles after passage through human brain microvascular endothelial cells. *Physics in Medicine and Biology* **61,** 3986–4000. doi:10.1088/0031-9155/61/11/3986 (2016).
21. Poller, W. C. *et al.* Magnetic particle spectroscopy reveals dynamic changes in the magnetic behavior of very small superparamagnetic iron oxide nanoparticles during cellular uptake and enables determination of cell-labeling efficacy. *Journal of Biomedical Nanotechnology* **12,** 337–346. doi:10.1166/JBN.2016.2204 (2016).
22. Gruettner, M. *et al.* *1D-image reconstruction for magnetic particle imaging using a hybrid system function* in *2011 IEEE Nuclear Science Symposium Conference Record* (IEEE, 2011), 2545–2548. ISBN: 978-1-4673-0120-6. doi:10.1109/NSSMIC.2011.6152687.
23. Schmidt, D., Graeser, M., von Gladiss, A., Buzug, T. M. & Steinhoff, U. Imaging characterization of MPI tracers employing offset measurements in a two dimensional magnetic particle spectrometer. *International Journal on Magnetic Particle Imaging* **2,** 1–4. doi:10.18416/ijmpi.2016.1604002 (2016).

24. Graeser, M., von Gladiss, A., Weber, M. & Buzug, T. M. Two dimensional magnetic particle spectrometry. *Physics in Medicine and Biology* **62,** 3378–3391. doi:10.1088/1361-6560/aa5bcd (2017).
25. Chen, X., Graeser, M., Behrends, A., von Gladiss, A. & Buzug, T. M. First Measurement and SNR Results of a 3D Magnetic Particle Spectrometer. *International Journal on Magnetic Particle Imaging* **4,** 1–7. doi:10.18416/IJMPI.2018.1810001 (2018).
26. Yoshida, T., Othman, N. B. & Enpuku, K. Characterization of magnetically fractionated magnetic nanoparticles for magnetic particle imaging. *Journal of Applied Physics* **114,** 173908. doi:10.1063/1.4829484 (2013).
27. Bauer, L. M., Situ, S. F., Griswold, M. A. & Samia, A. C. S. Magnetic particle imaging tracers: State-of-the-art and future directions. **6,** 2509–2517. doi:10.1021/acs.jpclett.5b00610 (2015).
28. Chikazumi, S. *Physics of Magnetism.* ISBN: 978-0-471-15535-5 (John Wiley & Sons, 1964).
29. Cornell, R. M. & Schwertmann, U. *The Iron Oxides. Structure, Properties, Reactions, Occurences and Uses.* 2nd. ISBN: 978-3-527-60209-4. doi:10.1002/3527602097 (Wiley-VCH Verlag, 2003).
30. Biederer, S. *et al. Estimation of magnetic nanoparticle diameter with a magnetic particle spectrometer* in *World Congress on Medical Physics and Biomedical Engineering* (eds Dössel, O. & Schlegel, W. C.) **25/8** (Springer, Berlin, Heidelberg, 2010), 61–64. ISBN: 978-3-642-03887-7. doi:10.1007/978-3-642-03887-7_17.
31. Eberbeck, D., Wiekhorst, F., Wagner, S. & Trahms, L. How the size distribution of magnetic nanoparticles determines their magnetic particle imaging performance. *Applied Physics Letters* **98,** 182502. doi:10.1063/1.3586776 (2011).
32. Draack, S., Viereck, T., Kuhlmann, C., Schilling, M. & Ludwig, F. Temperature-dependent MPS measurements. *International Journal on Magnetic Particle Imaging* **3,** 3–6. doi:10.18416/ijmpi.2017.1703018 (2017).

33. Bean, C. P. & Livingston, J. D. Superparamagnetism. *Journal of Applied Physics* **30,** S120. doi:10.1063/1.2185850 (2009).

34. Coffey, W. T., Kalmykov, Y. P. & Waldron, J. T. *The Langevin Equation.* 2nd. ISBN: 978-981-238-462-1. doi:10.1142/5343 (World Scientific, 2004).

35. Deissler, R. J., Wu, Y. & Martens, M. A. Dependence of Brownian and Néel relaxation times on magnetic field strength. *Medical Physics* **41,** 012301. doi:10.1118/1.4837216 (2014).

36. Dieckhoff, J., Eberbeck, D., Schilling, M. & Ludwig, F. Magnetic-field dependence of Brownian and Néel relaxation times. *Journal of Applied Physics* **119,** 043903. doi:10.1063/1.4940724 (2016).

37. Gleich, B. *Principles and Applications of Magnetic Particle Imaging.* ISBN: 978-3-658-01961-7. doi:10.1007/978-3-658-01961-7 (Springer Vieweg, 2013).

38. Weizenecker, J., Gleich, B. & Borgert, J. Magnetic particle imaging using a field free line. *Journal of Physics D: Applied Physics* **41,** 105009. doi:10.1088/0022-3727/41/10/105009 (2008).

39. Knopp, T., Sattel, T. F., Biederer, S. & Buzug, T. M. Field-free line formation in a magnetic field. *Journal of Physics A: Mathematical and Theoretical* **43,** 012002. doi:10.1088/1751-8113/43/1/012002 (2009).

40. Erbe, M., Sattel, T. F. & Buzug, T. M. Improved field free line magnetic particle imaging using saddle coils. *Biomedizinische Technik* **58,** 577–582. doi:10.1515/bmt-2013-0030 (2013).

41. Knopp, T. *et al.* Trajectory analysis for magnetic particle imaging. *Physics in Medicine and Biology* **54,** 385–397. doi:10.1088/0031-9155/54/2/014 (2009).

42. Weizenecker, J., Borgert, J. & Gleich, B. A simulation study on the resolution and sensitivity of magnetic particle imaging. *Physics in Medicine and Biology* **52,** 6363–6374. doi:10.1088/0031-9155/52/21/001 (2007).

43. Gleich, B., Weizenecker, J. & Borgert, J. Experimental results on fast 2D-encoded magnetic particle imaging. *Physics in Medicine and Biology* **53,** 2005–2008. doi:10.1088/0031-9155/53/6/N01 (2008).
44. Grüttner, M. *et al.* On the formulation of the image reconstruction problem in magnetic particle imaging. *Biomedizinische Technik* **58,** 583–591. doi:10.1515/bmt-2012-0063 (2013).
45. Goodwill, P. W. & Conolly, S. M. The X-space formulation of the magnetic particle imaging process: 1-D signal, resolution, bandwidth, SNR, SAR, and magnetostimulation. *IEEE Transactions on Medical Imaging* **29,** 1851–1859. doi:10.1109/TMI.2010.2052284 (2010).
46. Goodwill, P. W. & Conolly, S. M. Multidimensional X-space magnetic particle imaging. *IEEE Transactions on Medical Imaging* **30,** 1581–1590. doi:10.1109/TMI.2011.2125982 (2011).
47. Rahmer, J., Weizenecker, J., Gleich, B. & Borgert, J. Analysis of a 3-D System function measured for magnetic particle imaging. *IEEE Transactions on Medical Imaging* **31,** 1289–1299. doi:10.1109/tmi.2012.2188639 (2012).
48. Knopp, T. *et al.* Model-based reconstruction for magnetic particle imaging. *IEEE Transactions on Medical Imaging* **29,** 12–18. doi:10.1109/TMI.2009.2021612 (2010).
49. Knopp, T. *et al.* 2D model-based reconstruction for magnetic particle imaging. *Medical Physics* **37,** 485–491. doi:10.1118/1.3271258 (2010).
50. Von Gladiss, A., Graeser, M., Szwargulski, P., Knopp, T. & Buzug, T. M. Hybrid system calibration for multidimensional magnetic particle imaging. *Physics in Medicine and Biology* **62,** 3392–3406. doi:10.1088/1361-6560/aa5340 (2017).
51. Zhong, J., Liu, W., Kong, L. & Morais, P. C. A new approach for highly accurate, remote temperature probing using magnetic nanoparticles. *Scientific Reports* **4,** 6638. doi:10.1038/srep06338 (2014).
52. Wells, J., Paysen, H., Kosch, O., Trahms, L. & Wiekhorst, F. Temperature dependence in magnetic particle imaging. *AIP Advances* **8,** 056703. doi:10.1063/1.5004506 (2018).

53. Salamon, J. *et al.* Visualization of spatial and temporal temperature distributions with magnetic particle imaging for liver tumor ablation therapy. *Scientific Reports* **10,** 7480. doi:10.1038/s41598-020-64280-1 (2020).
54. Graeser, M., Knopp, T., Sattel, T. F., Gruettner, M. & Buzug, T. M. *Signal separation in magnetic particle imaging* in *2012 IEEE Nuclear Science Symposium and Medical Imaging Conference Record* (IEEE, 2012), 2483–2485. ISBN: 978-1-4673-2030-6. doi:10.1109/NSSMIC.2012.6551566.
55. Graeser, M., Knopp, T., Grüttner, M., Sattel, T. F. & Buzug, T. M. Analog receive signal processing for magnetic particle imaging. *Medical Physics* **40,** 042303. doi:10.1118/1.4794482 (2013).
56. Chen, X., Behrends, A., Graeser, M., Neumann, A. & Buzug, T. M. *Optimizing the coil setup for a three-dimensional magnetic particle spectrometer* in *International Workshop on Magnetic Particle Imaging* (eds Buzug, T. M., Borgert, J. & Knopp, T.) (Infinite Science Publishing, 2016), 59. ISBN: 978-3-945954-19-5.
57. Misakian, M. Equations for the magnetic field produced by one or more rectangular loops of wire in the same plane. *Journal of Research of the National Institute of Standards and Technology* **105,** 557–564. doi:10.6028/jres.105.045 (2000).
58. Holton Precision Audio. Accessed: 1 January 2020. https://holtonprecisionaudio.com/.
59. Bowick, C. *RF Circuit Design.* 2nd. ISBN: 978-0-7506-8518-4. doi:10.1016/B978-0-7506-8518-4.X5001-2 (Elsevier, 2007).
60. Boylestad, R. L. *Introductory Circuit Analysis.* 10th. ISBN: 978-0-13-097417-4 (Pearson, 2003).
61. KEMET Electronics Corporation. *A72, Polypropylene Film/Foil, Axial.* 2014. https://content.kemet.com/datasheets/KEM_F3039_A72_AXIAL.pdf.
62. KEMET Electronic Corporation. *C4C, Axial Round, 850–3000 VDC / 450–750 VAC.* 2014. https://content.kemet.com/datasheets/KEM_F3042_C4C_AXIAL.pdf.

63. KEMET Electronics Corporation. *C4G, Axial Round, 250–850 VDC / 160–450 VAC.* 2014. https://content.kemet.com/datasheets/KEM_F3040_C4G_AXIAL.pdf.

64. Murgatroyd, P. N. & Belahrache, D. *Economic designs for single-layer toroidal inductors* in *IEE Proceedings B (Electric Power Applications)* **132** (1985), 315–318. doi:10.1049/ip-b.1985.0047.

65. Delta Elektronika B.V. *Product Manual SM800.* 2021. https://www.delta-elektronika.nl/en/products/dc-power-supplies-800w-sm800-series.html.

66. Camtec Power Supplies GmbH. *UMS Manual.* 2021. https://www.camtec-powersupplies.com/ums00100.

67. Malhotra, A. *et al.* Tracking the growth of superparamagnetic nanoparticles with an in-Situ magnetic particle spectrometer (INSPECT). *Scientific Reports* **9,** 10538. doi:10.1038/s41598-019-46882-6 (2019).

68. Malhotra, A., Schwegmann, H., Schumacher, J., Chen, X. & Buzug, T. M. Fully differential low noise amplifier for MPI/MPS. *International Journal on Magnetic Particle Imaging* **6,** Suppl. 1. doi:10.18416/IJMPI.2020.2009006 (2020).

69. Formlabs Incorporated. *Material Data Sheet Standard.* 2017. https://formlabs.com/de/materials/standard/.

70. Texas Instruments Incorporated. *LMH6553 900 MHz Fully Differential Amplifier With Output Limiting Clamp.* 2013. https://www.ti.com/product/LMH6553.

71. Innovative Integration. *X3-A4D4 PCI Express XMC Module with Four 4 MSPS A/Ds, Four 50 MSPS DACs and 1.8M Spartan3A DSP FPGA.* 2007. https://isipkg.com/product/x3-a4d4/.

72. Innovative Integration. *X3-10M PCI Express XMC Module with 8 simultaneous channels of 25 MSPS 16-bit A/D, and 1.8M FPGA with DSP.* 2007. https://isipkg.com/wp-content/uploads/2020/02/X3-10M_datasheet.pdf.

73. Innovative Integration. *X3-Timing Precision Sampling Rate Generation and Triggering Controls with GPS and High Precision Reference.* 2016. https://isipkg.com/product/x3-timing/.

74. Innovative Integration. *XMC Adapter for PCI/PCI-X.* 2008. https://www.entegra.co.uk/wp-content/uploads/2014/03/xmc_to_pci_adapter_board.pdf.

75. Pang, F., Gao, L., Yuan, Y., Bu, Q. & Ji, J. *Effects of geometrical parameters on the performance of Rogowski coil for current measuring* in *2016 IEEE PES Asia-Pacific Power and Energy Engineering Conference* (IEEE, 2016), 232–236. ISBN: 978-1-5090-5418-3. doi:10.1109/APPEEC.2016.7779503.

76. Vishay Intertechnology Incorporated. *Optocoupler, Phototransistor Output, with Base Connection.* 2010. https://www.vishay.com/docs/83725/4n25.pdf.

77. Vishay Intertechnology Incorporated. *Linear Optocoupler, High Gain Stability, Wide Bandwidth.* 2014. https://www.vishay.com/docs/83622/il300.pdf.

78. Kniel System-Electronic GmbH. *Double Output CD 5.1,5.* 2007. https://kniel.de/download/96320682.01.pdf.

79. Kniel System-Electronic GmbH. *Double Output CLDO 24.2,5.* 2007. https://kniel.de/download/96320551.00.pdf.

80. Schroff GmbH. *PSx Single (PSx 1xx).* 2008. https://schroff.nvent.com/sites/g/files/hdkjer281/files/acquiadam/2021-11/73972-020_nV_.pdf?asset_type=Data%5C%20Sheet.

81. Burgess, A. E. The Rose model, revisited. *Journal of the Optical Society of America A* **16,** 633–646. doi:10.1364/josaa.16.000633 (1999).

82. micromod Partikeltechnologie GmbH. *Modular Designed Nano and Micro particles.* 2019. https://www.micromod.de/en/produkte-2-magnetic-particles.html.

83. Eberbeck, D. *et al.* Multicore magnetic nanoparticles for magnetic particle imaging. *IEEE Transactions on Magnetics* **49,** 269–274. doi:10.1109/TMAG.2012.2226438 (2013).

84. Chen, X., Behrends, A., Malhotra, A., Neumann, A. & Buzug, T. M. Temperature-dependent spectrum measurement using a magnetic particle spectrometer. *International Journal on Magnetic Particle Imaging* **6,** Suppl. 1. doi:10.18416/ijmpi.2020.2009034 (2020).

85. Woodford, O. *vol3d v2.* Retrieved: 10 January 2022. https://www.mathworks.com/matlabcentral/fileexchange/22940-vol3d-v2.

Xin CHEN

ADDRESS

Durlacher Str. 21,
10715 Berlin
Germany

PHONE

+49 17680828055

EMAIL

chenxin1034@hotmail.com

WEBSITE

Linkedin.com/in/xin-chen-05675894/

EXPERIENCE

02/2023 - PRESENT

System Engineer | W.O.M World of Medicine | Germany

03/2017 – 12/2021

Research Assistant | Institute of Medical Engineering, University of Lübeck | Germany

EDUCATION

03/2017 – PRESENT

University of Lübeck, Germany
Doctor of Engineer (Expecting)

10/2014 – 08/2016

University of Lübeck & Lübeck University of Applied Sciences, Germany | Biomedical Engineering
Master of Science

09/2010 – 06/2014

Zhengzhou University, China | Biomedical Engineering
Bachelor of Engineer

PUBLICATION

Implementation and imaging with a versatile 180 mm magnetic-particle-imaging field-generator
Jan Stelzner, Anna Bakenecker, André Behrends, Gael Bringout, **Xin Chen**, Anselm von Gladiss, Ksenija Gräfe, Jonas Schumacher, and Thorsten M. Buzug
(2022) Journal of Magnetism and Magnetic Materials. Volume 559: 169509. https://doi.org/10.1016/j.jmmm.2022.169509

MPI of soft ferromagnetic needles
Justin Ackers, Anna Bakenecker, **Xin Chen**, Thorsten Buzug, and Matthias Graeser
(2022) International Journal on Magnetic Particle Imaging. Vol. 8 No. 1 Suppl 1. https://doi.org/10.18416/IJMPI.2022.2203088

Recent developments in magnetic particle imaging
Alexander Neumann, Ksenija Gräfe, Anselm von Gladiss, Mandy Ahlborg, André Behrends, **Xin Chen**, Jonas Schumacher, Yvonne Blancke Soares, Thomas Friedrich, Humin Wei, Ankit Malhorta, Eric Aderhold, Anna C. Bakenecker, Kerstin Lüdtke-Buzug, and Thorsten M. Buzug
(2022) Journal of Magnetism and Magnetic Materials. Volume 550: 169037. https://doi.org/10.1016/j.jmmm.2022.169037

Magnetic particle imaging
André Behrends, Anna C. Bakenecker, Mandy Ahlborg, Ksenija Gräfe, Jonas Schumacher, Jan Stelzner, Franz Wegner, Alexander Neumann, Yvonne Blancke Soares, Kerstin Lüdtke-Buzug, **Xin Chen**, Huimin Wei, Ankit Malhotra, Thomas Friedrich, and Thorsten M Buzug
(2021) Imaging Modalities for Biological and Preclinical Research: A Compendium. Volume 2, Pages II.8-1 to II.8-10.
https://doi.org/10.1088/978-0-7503-3747-2ch12

Fully differential low noise amplifier for MPI/MPS
Ankit Malhotra, Holger Schwegmann, Jonas Schumacher, **Xin Chen**, and Thorsten M. Buzug
(2020) International Journal on Magnetic Particle Imaging. Volume 6 No 2 Suppl 1. https://doi.org/10.18416/IJMPI.2020.2009006

Efficient hybrid 3D system calibration for magnetic particle imaging systems using a dedicated device
Anselm von Gladiss, Matthias Graeser, André Behrends, **Xin Chen**, and Thorsten M. Buzug
(2020) Scientific Reports. Volume 10: 18432. https://doi.org/10.1038/s41598-020-75122-5

Temperature-dependent spectrum measurement using a magnetic particle spectrometer
Xin Chen, André Behrends, Ankit Malhotra, Alexander Neumann, and Thorsten M. Buzug
(2020) International Journal on Magnetic Particle Imaging. Volume 6 No 2 Suppl 1. https://doi.org/10.18416/IJMPI.2020.2009034

Investigating spatial resolution, field Sequences and image reconstruction strategies using hybrid phantoms in MPI
Anselm von Gladiss, Matthias Graeser, Aileen Cordes, Anna C. Bakenecker, André Behrends, **Xin Chen**, and Thorsten M. Buzug
(2020) International Journal on Magnetic Particle Imaging. Volume 6 No 1. https://doi.org/10.18416/IJMPI.2020.2003004

Sample temperature control in a three-dimensional magnetic particle spectrometer
Xin Chen, André Behrends, Alexander Neumann, and Thorsten M. Buzug
(2019) Paper presented at 9th International Workshop on Magnetic Particle Imaging, IWMPI 2019, New York, United States. 211.

First Measurement and SNR Results of a 3D Magnetic Particle Spectrometer
Xin Chen, Matthias Graeser, André Behrends, Anselm von Gladiss, and Thorsten M. Buzug
(2018) International Journal on Magnetic Particle Imaging. Volume 4 No 1. https://doi.org/10.18416/IJMPI.2018.1810001

Optimizing Transmit Coils for a Magnetic Particle Spectrometer
Xin Chen, Alexander Neumann and Thorsten M. Buzug
(2018) Paper presented at 8th International Workshop on Magnetic Particle Imaging, IWMPI 2018, Hamburg, Germany. 161.

First measured result of the 3D Magnetic Particle Spectrometer
Xin Chen, Matthias Graeser, André Behrends, Anselm von Gladiß, Thorsten M. Buzug
(2017) In L. Sefc, T. M. Buzug, & T. Knopp (Eds.), 7th International Workshop on Magnetic Particle Imaging (IWMPI 2017) (pp. 123).

Optimizing the Coil Setup for a Three-Dimensional Magnetic Particle Spectrometer
Xin Chen, André Behrends, Matthias Graeser, Alexander Neumann, and Thorsten M. Buzug
(2016) In T. M. Buzug, J. Borgert, & T. Knopp (Eds.), 6th International Workshop on Magnetic Particle Imaging (IWMPI 2016) (pp. 59).